UNIVERSIDADE DE SÃO PAULO
INSTITUTO DE GEOCIÊNCIAS

Andean Uplift Patterns in the Ecuadorian Andes

DANIEL RICARDO HERNÁNDEZ CHAPARRO

Dissertação apresentada ao Programa de Pós-Graduação em Geoquímica e Tectônica do Instituto de Geociências da Universidade de São Paulo como requisito parcial para a obtenção do título de Mestre em Ciências.

Área de concentração: Geotectônica

Orientador: Prof. Dr. Maurício Parra

SÃO PAULO
2023

Serviço de Biblioteca e Documentação do IGc/USP
Ficha catalográfica gerada automaticamente com dados fornecidos pelo(a) autor(a)
via programa desenvolvido pela Seção Técnica de Informática do ICMC/USP

Bibliotecários responsáveis pela estrutura de catalogação da publicação:
Sonia Regina Yole Guerra - CRB-8/4208 | Anderson de Santana - CRB-8/6658

Hernández Chaparro, Daniel Ricardo
Padrões de Levantamento Andino nos Andes Equatorianos / Daniel Ricardo Hernández Chaparro; orientador Mauricio Parra Amézquita. -- São Paulo, 2023.
114 p.

Dissertação (Mestrado - Programa de Pós-Graduação em Geoquímica e Geotectônica) -- Instituto de Geociências, Universidade de São Paulo, 2023.

1. Termocronologia de baixa temperatura em apatita. 2. Padrões de soerguimento. 3. Elementos traço de apatita. I. Parra Amézquita, Mauricio, orient. II. Título.

UNIVERSIDADE DE SÃO PAULO
INSTITUTO DE GEOCIÊNCIAS

Andean Uplift Patterns in the Ecuadorian Andes

DANIEL RICARDO HERNANDEZ CHAPARRO

Orientador: Prof. Dr. Mauricio Parra Amezquita

Dissertação de Mestrado

Nº 927

COMISSÃO JULGADORA

Dr. Mauricio Parra Amezquita

Dr. Sebastian Zapata Henao

Drª. Andréa Ritter Jelinek

SÃO PAULO
2023

Acknowledgments

This research was financially supported by the Fundação de Amparo A Pesquisa do Estado de São Paulo-FAPESP, funded by the Sao Paulo Research Foundation (FAPESP) grants 2018/15613-1, 2021/13551-1, 2022/13766-0, and CNPq grant PQ 307324/2022-2.

I extend my deepest gratitude to my advisor, Prof. Mauricio Parra, for his unwavering support throughout every stage of the research process. His invaluable insights, research incentives, and commitment to my academic growth have been instrumental in the successful completion of this project.

I would like to acknowledge Ana Maria Patiño for her invaluable suggestions, collaborative efforts, and assistance during sample preparation, as well as her dedicated teaching of laboratory procedures at LTC.

I am sincerely thankful to Giovanny Nova for his valuable suggestions, teamwork, and insightful discussions that have significantly contributed to the development and interpretation of the results.

Special thanks go to Prof. Kerry Gallagher for her invaluable assistance in modeling the data, as well as to Dr. Alexis Dereyke, and Dr. Nathan Cogné from the University of Rennes. I am grateful for their warm welcome into their laboratories and their support in obtaining helium data and multi-elemental geochemistry data

I would like to extend my sincere thanks to Geoffrey Ruiz for their invaluable advice on interpreting the results and for generously sharing their extensive knowledge of Ecuadorian geology. Their support and insights have been instrumental in the success of this project.

Sebastian Zapata for providing me with sedimentary samples from the Napo Uplift that were include in this work.

I finally would like to thank all my collages and friends at IGc - USP for discussions and support.

Abstract

Reconstructing the exhumation history of accretionary orogens is essential for understanding the mechanisms and rates that govern subduction orogenesis. The Ecuadorian Andes constitute a bivergent orogen with active thrusting at the western flank of the Western Cordillera and in the sub-Andean ranges, at the eastern flank of the Eastern Cordillera (Cordillera Real). In the frontal Andean margin of northeastern Ecuador, Paleozoic and Jurassic to Miocene strata and positive tectonic inversion Jurassic magmatic arc rocks are exposed in a broad anticlinal named the Napo Uplift, which has been associated with transpressional deformation and ensuing positive tectonic inversion from temperatures < ~100°C. Scarce thermochronometry but abundant sedimentary provenance data indicate that exhumation in the Cordillera Real may have occurred since the Late Cretaceous, concomitant to flexural subsidence and foreland basin development farther to the east, in the present-day Napo Uplift. However, the patterns of subsequent exhumation that led to its present-day configuration remain elusive due to the lack of low-temperature thermochronometry. In this study, we conducted new apatite (U-Th)/He and fission-track analyses on Jurassic to Miocene magmatic and sedimentary rocks, as well as vitrinite reflectance in Cretaceous mudstones, from the Napo Uplift. One-dimensional thermal modeling, both single- and multi-sample, of new and published data reveals distinct periods of rapid cooling and exhumation from different morphotectonic domains in the Northern Sub-Andean Zone. We document Miocene exhumation associated with out-of-sequence thrusting across the Ecuadorian Subandean zone and document along-strike variations and possible triggering mechanisms. In the Napo uplift, we identify an uplift, commencing around ~11 Ma in the northern part and ~13 Ma in the southern region, respectively. In addition, we characterized provenance patterns using detrital apatites, integrating fission-track data, U-Pb ages, and trace element geochemistry. Our results and available multi-method proxies allow for documenting the spatial and temporal patterns of source area evolution as well as the unroofing patterns of the Cordillera Real. Altogether, our combined dataset show that the tectonic history of Napo Uplift region includes fault reactivation at ~13 Ma and thrust belt advancement after ~7 Ma most likely dominated by transpression transmitted along the deep dextral Puná-Pallatanga-Cosanga-Chingual fault system.

Keywords: Low-temperature thermochronology in apatite, Uplift patterns, Apatite trace elements

RESUMO

Reconstruir a história da exumação de orógenos de acreção é fundamental para compreender os mecanismos e taxas que governam a orogênese por subducção. Os Andes equatoriais constituem um orógeno bivergente com atividade de empurrão ativa no flanco oeste da Cordilheira Ocidental e ativa nas cadeias Subandinas no flanco leste da Cordilheira Oriental (Cordilheira Real). Na margem frontal andina nordeste do Equador, são expostos estratos paleozoicos e jurássicos até o Mioceno, além de rochas de arco magmático jurássico com inversão tectônica positiva em uma ampla anticlinal chamada Elevação de Napo. Essa elevação tem sido associada à deformação transpressional e subsequente inversão tectônica positiva a temperaturas inferiores a cerca de 100°C. Embora haja poucos dados de termocronometria, informações abundantes sobre a proveniência sedimentar indicam que a exumação na Cordilheira Real pode ter ocorrido desde o final do Cretáceo, simultaneamente à subsidência flexural e ao desenvolvimento de bacias de antepaís mais a leste, na região da atual Elevação de Napo. No entanto, os padrões de exumação subsequentes que levaram à sua configuração atual permanecem desconhecidos devido à falta de termocronometria de baixa temperatura. Neste estudo, conduzimos novas análises de (U-Th)/He e traços de fissão em apatitas de rochas magmáticas e sedimentares do Jurássico ao Mioceno, bem como a reflectância da vitrinita em argilitos do Cretáceo da Elevação de Napo. Modelagem térmica unidimensional, tanto de amostras únicas quanto de múltiplas amostras, de dados novos e já publicados, revela períodos distintos de resfriamento e exumação rápidos em diferentes domínios morfotectônicos associada ao *thrusting* fora de sequência através da Zona Subandina norte. Documentamos a exumação do Mioceno na Zona Subandina equatorial e identificamos variações ao longo do comprimento, juntamente com possíveis mecanismos desencadeadores. No anticlinal de Napo, identificamos um soerguimento diacrônico, que começa ao redor de ~10 Ma na parte norte e ~13 Ma na parte sul respectivamente. Além disso, caracterizamos padrões de proveniência usando apatitas detríticas, integrando dados de traços de fissão e (U-Th)/He em apatita, idades U-Pb e análises geoquímicas de elementos-traço. Nossos resultados permitem documentar a evolução espacial e temporal das áreas fonte assim como os padrões de denudação da Cordilheira Real. Em resumo, nosso conjunto de dados combinado mostra que a história tectônica da região da Elevação de Napo incluiu a reativação de falhas por volta de 13 Ma, seguida pelo avanço do cinturão de dobramento após aproximadamente 7 Ma, provavelmente dominado por transpressão transmitida ao longo do sistema profundo de falhas dextrais Puna-Pallatanga-Cosanga-Chingual.

Palavras-chave: Termocronologia de baixa temperatura em apatita, Padrões de soerguimento, Elementos traço de apatita.

SUMMARY

FIGURE LIST

TABLE LIST

ACRONYM LIST

AF - Abitagua Fault
AFT - Apatite Fission Track
AL - Arajuno Locality
ALK - Alkali-rich igneous rock
ASI - Aluminum saturation index
AUPb - Apatite U-Pb
BBO- Billion Barrels of Oil
BF - Bermejo Field
CC - Coastal Cordillera
CCPP - Chingual-Cosanga-Pallatanga-Puná
CF - Cosanga Fault
CLIP - Caribbean Large Igneous Province
CR - Cordillera Real
CU - Cutucú Uplift
CV - Coefficient of variation
DGM - Dolores Guayaquil Megashear
DRS - Data Reduction Scheme
ESR - Equivalent Spherical Radius
GeOHeLiS - Elemental and Isotope Geochemistry
ID - Interandean Depression
IGc - Institute of Geoscience
IM - Mafic I-type granitoids and mafic igneous rocks
LA-ICP-MS
LM - Low and medium-grade metamorphic
LTC - Thermochronology Laboratory
MAD - Madagascar apatite
MTL - Mean Track Length
NAS - Northern Andean Sliver
nccSTP - cubic centimeters at standard temperature and pressure
NU - Napo Uplift
OF - Oglan Field
PD - Pastaza Depression
PF - Pungaracu Field
QF - Queijos Fault
REE - Rare Earth Element
RV - Reventador Volcano
SAF - Subandean Front
SATB - Sub-Andean Thrust Belt
SAZ - Sub-Andean Zone
SM - S-type granitoids
SF - Subandean Fault
SynAp - Syntetic apatite
t-T - Thermal-time
UM - Ultramafic rocks
WC – Western Cordillera

1. INTRODUCTION

In Cordilleran orogens, shifts from orthogonal to oblique subduction or the subduction of buoyant bathymetric highs such as aseismic ridges and oceanic plateaus often result in an increase in plate coupling at the subduction interface (e.g., Singh et al., 2011; Taylor et al., 2005). This increased coupling has been interpreted to cause changes in the deformation in the upper plate, as changes in subduction dynamics have effects on both the shape and stress field in the descending slab (Bevis, 1986), and on the stress regime and the strain patterns in the upper plate (e,g., Gutscher, 1999, Horton et al., 2022; Singh et al., 2011).

The strong coupling has been suggested to trigger widespread deformation and uplift at subduction margins (e.g., Dominguez et al., 1998; George et al., 2023; Lallemand et al., 1992; Ramos, 2005; Rosenbaum & Mo, 2011; von Huene et al., 1997), and in some cases, it may result in extensional or compressional deformation in the upper plate in regions as far as the back-arc (Meffre and Crawford, 2001; Pardo et al., 2002, Axen et al., 2018). Exhumation of uplift in flat-slab regions has been associated with the dynamic component induced by the buoyancy of a fluid-rich asthenospheric wedge, such as in the Colombian Eastern Cordillera (Siravo et al., 2019).

A complex history of accretion, subduction, and attendant uplift has shaped the Ecuadorian Andes. which constitute the narrowest part of the northern Andes. The Andes in Ecuador comprise a bivergent orogen with double-wedge thrusting geometry (Baby et al., 2013). The west-vergent wedge corresponds to the Ecuadorian coastal domain, west of the Western Cordillera (Eguez et al., 2003; Jaillard et al., 2004, 2005), while the east-vergent wedge in the Sub-Andean ranges corresponds to the eastern flank of the Eastern Cordillera (Cordillera Real).

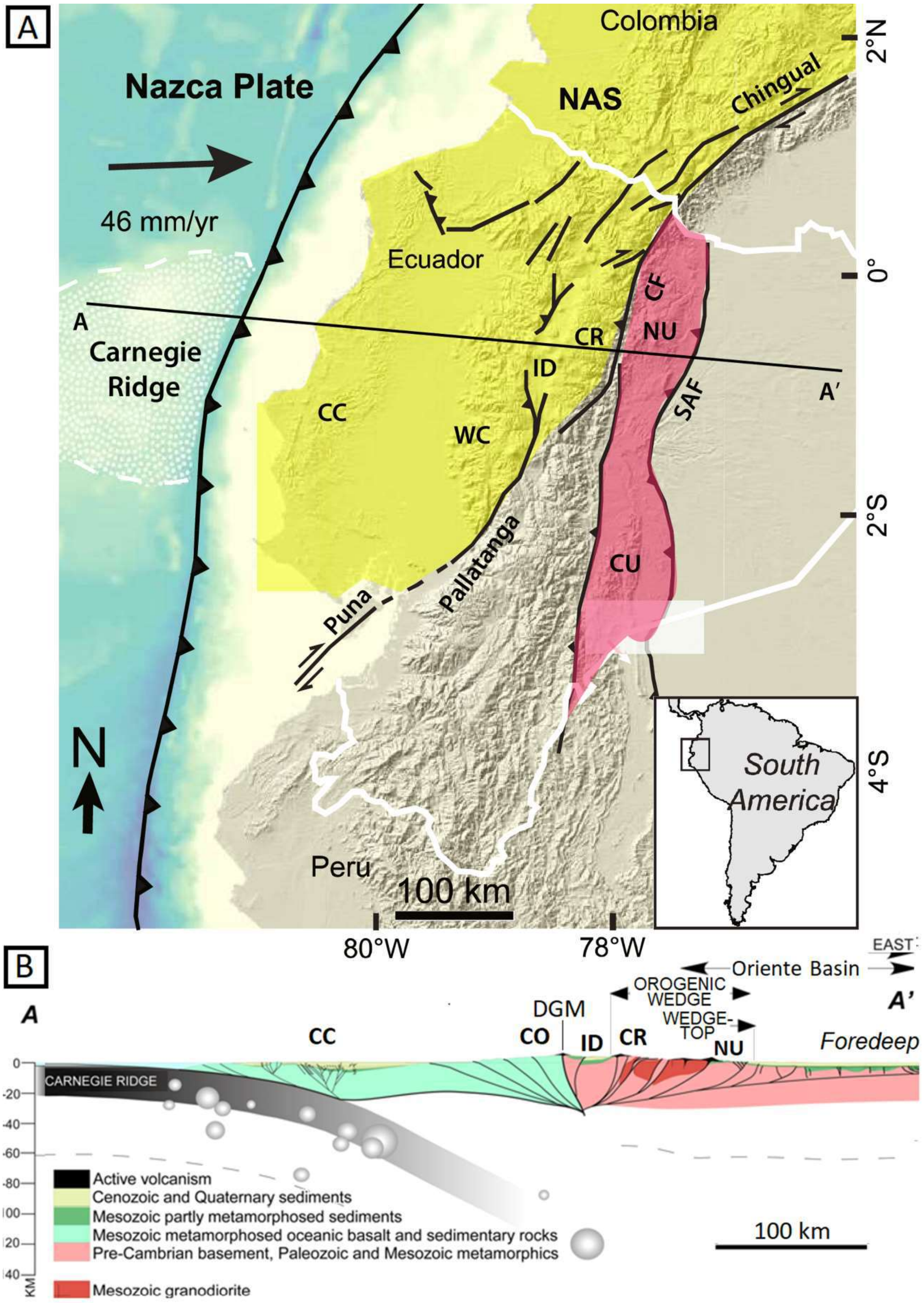

Fig 1. (A) Principal active faults (black lines; Alvarado et al., 2016) in the Ecuadorian Andes with Nazca-Plate bathymetry and Carnegie Ridge, showing the Northern Andean Sliver (NAS) and the Sub-Andean Zone (SAZ) in red transparent shading limited in the Northern SAZ by the Puna-Pallatanga-Cosanga-Chingual (CCPP) fault system (Yepes et al., 2016 and references therein). *Modified* form Margirier et al., (2022). **(B)** Structural cross-section (A–A′) across the Ecuadorian Andes showing the double-wedge geometry associated to retro-arc and foreland basin. DGM, Dolores Guayaquil Megashear; CC is the Coastal Cordillera, CF is the Cosanga Fault, PD is the

Pastaza Depression, CU is the Cutucú Uplift, ID is the Interandean Depression, NU is the Napo Uplift, SAF is the Subandean Front, WC is the Western Cordillera. *Modified* from Baby et al., (2013).

In the Eastern Cordillera, the NU is a complex antiformal culmination elevated 1.6 km above the Amazonian foreland and associated with slip along a deep active mega-thrust system involving thick-skinned tectonics (Baby et al., 2013) and transpressional flower structures associated with the Sub-Andean Front system. (Cediel et al., 2003). East of it, the Oriente Basin constitutes the modern foredeep of the Ecuatorian foreland basin system and hosts up to 4.5 km of Cretaceous and Cenozoic clastic deposits and approximately 30 billion barrels of oil (BBO) distributed across 100 fields (Rivadeneira & Baby 2004). Based on a thickness reduction in the post-Turonian stratigraphic section studied with surface and subsurface data across the NU, it has been suggested that initial tectonic inversion and anticlinal folding occurred in the Late Cretaceous (Santonian-Campanian) (Baby et al.,2013; Rivadeneira and Baby, 2004).

Tectonic uplift in the NU has juxtaposed Jurassic and Cretaceous units along its hanging-wall against Miocene sedimentary rocks of the Arajuno Formation, which suggest a post-Miocene activity, concomitant to the subduction of the Carnegie Ridge (Kerr et al., 2002; Vallejo et al., 2006). Thermochronometry and sedimentary provenance data document that exhumation in a narrow belt referred to as the Sub-Andean Thrust Belt (SATB) between the NU and Cordillera Real in Ecuador, may have occurred at least since Late Miocene (Spikings et al., 2000; Ruiz, 2002; Ruiz et al., 2004). However, apatite fission track (AFT) ages from the Jurassic magmatic basement rocks from the NU reveal a poorly resolved cooling period between 25 and 0 Ma (Spikings et al., 2000; Ruiz, 2002; Ruiz et al., 2004). Individual pulses of Miocene cooling remain unresolved, as available data suggest that sedimentary rocks in the NU have not been heated above 120°C (Ruiz et al., 2004). Moreover, no studies using sensitive thermochronometers like apatite (U-Th)/He (AHe) have been conducted, making it challenging to precisely document the age of Neogene thrust tectonics in this frontal margin. Consequently, Late Miocene exhumation patterns in the NU and any potential link between ridge subduction and exhumation in the Sub-Andean Zone (SAZ) remain unexplored. Unraveling the exhumation patterns of the NU is a key element for assessing the contribution of the topographic growth of the Northern Andes to the formation of the trans-continental Amazon River (e.g., Bicudo et al., 2020).

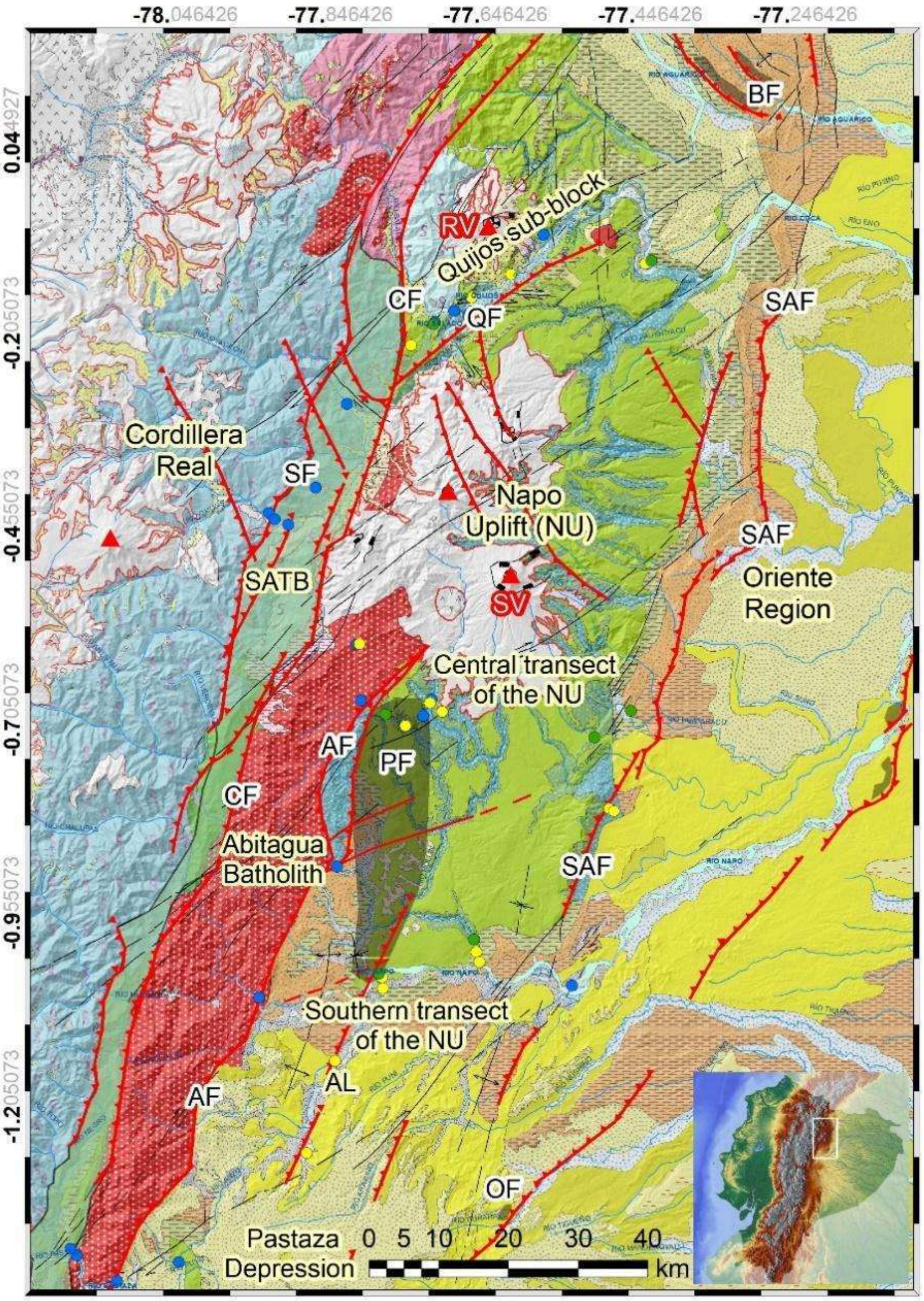

Fig 2. Main structural sketch-map of the Napo Uplift region (see Figure 1 for location) (Balseca et al., 1993) above geological map Modified from INIGEMM, (2014-2016). Red lines represent the main structures related to a deep mega-thrust system (Baby et al., 2013). Blue points are thermochronological published data, Yellow points are new thermochronological data, and green

points are new vitrinite reflectance data. Transparent shading indicates oil fields. Conventions: Reventador Volcano (RV), Sumaco volcano (SV), Abitagua Fault (AF), Arajuno Locality (AL), Cosanga Fault (CF), Quijos Fault (QF), Subandean Fault (SF), Sub-Andean Front (SAF), PF (Pungarayacu Field), Oglan Field (OF), Bermejo Field (BF).

To unravel the thermal evolution of the NU with an enhanced spatiotemporal resolution and a special focus in the post-Miocene, we acquired new AHe and AFT data and new vitrinite reflectance data from multiple samples in structural blocks across the northern SAZ (NU and SATB). We constructed thermal models of coherent structural domains using our new results and previous research (Spikings et al., 2000; Ruiz, 2002; Ruiz et al., 2004). Finally, we used detrital apatite U-Pb ages and trace element geochemistry to unravel the provenance history of Cretaceous to Miocene strata exposed the NU, integrating also previous provenance proxies based on heavy minerals and detrital zircon U-Pb ages (Ruiz et al., 2007; Martin-Gombojav and Winlker, 2008; Pepper et al., 2016; Gutiérrez et al., 2019; Jackson et al., 2019; Vallejo et al., 2021). Our results reveal diachronous uplift of the NU since the middle Miocene associated with the long-lasting transpressive Chingual-Cosanga-Pallatanga-Puná (CCPP) fault system that propagated deformation to the east of the North Andean Sliver (NAS) from the subduction trench.

2. BACKGROUND

2.1. Regional Geological Setting

The convergence between the Pacific and South American plates from the Jurassic to the present has led to the construction of the Ecuadorian Andes (Cediel et al., 2003) and the development of several well-defined tectono-stratigraphic regions (Fig. 1). These regions can be broadly categorized into two main provinces: one floored by oceanic crust west of the Dolores-Guayaquil Megashear zone, and one continental province east of it (Aspden and Litherland, 1992; Jaillard et al., 2009, Fig 1). The oceanic province encompasses the Western Cordillera and the forearc region, which includes mafic plume-related magmatic rocks, island arc volcanic rocks, and upper Cretaceous to Eocene turbidites (e.g., Kerr et al., 2002) covered by a Neogene forearc strata (Reynaud et al., 1999) in the Coastal Cordillera. The Western Cordillera is composed by Triassic and Jurassic submarine basaltic–andesitic volcanic series and intrusive rocks tectonically juxtaposed with mostly turbiditic deposits of Late Cretaceous to Oligocene age (Aspden & Litherland, 1992; Litherland et al., 1994; Pratt et al., 2005). In northern Ecuador, the eastern limit of the oceanic domain is the Peltectec Fault (Arevalo et al., 2016). East of it, the continental domain comprises the Interandean Valley, the Cordillera Real (CR), the SAZ, and the retroarc foreland basin. The continental province is composed of Paleozoic and lower Cretaceous metamorphic rocks of the CR, which together with Cretaceous and Cenozoic sedimentary rocks of the retro-arc Amazon foreland basin, nonconformably overlie the Precambrian Guyana Shield (Litherland and Aspden, 1992; Litherland et al., 1994). The Interandean Valley is a topographic depression located between the Western and Real Cordilleras, filled by thick volcano-sedimentary sequences deposited from the late Miocene onward (Winkler et al., 2005). Inliers of metamorphic and dense crystalline rocks appear scattered across the basin (Bruet, 1949). The Cordillera Real is composed of Paleozoic garnet-biotite schists, paragneisses and minor amphibolites which towards the west are intruded by metamorphosed synkinematic two-mica peraluminous S-type granitoids of Late Triassic/Early Jurassic age (Tres Lagunas), Jurassic submarine basalt/andesite sequences, and metamorphosed volcaniclastic sediments in its western part (Aspden and

Litherland, 1992; Pratt et al., 2005). Farther to the east, the SAZ represents the westernmost part of the Oriente basin, where broad anticlines and thrust slices of the SATB expose a geological sequence comprising Paleozoic basement rocks, as well as Mesozoic to Cenozoic volcanic and sedimentary formations (Pratt et al., 2005; Ruiz, 2002). Notable large-scale antiforms in the SAZ include the NU in the northern part, and the Cutucú Uplift in the southern part (NU and CU respectively in Figure 1; Vallejo et al., 2021). Retroarc foreland basin strata made up by shallow marine deposits that grade upsection into fluvial strata constitute Oriente Basin and are exposed in the Napo and Cutucú thrust belts.

2.2. Geodynamic evolution

Extrusion of the plume-related oceanic Caribbean Large Igneous Province (CLIP) onto the Farallon plate in the present-day Pacific plate near the Galapagos hotspot took place between 95 and 70 Ma, with a gradual change from plume to plume-subduction magmatic signatures (Whattam and Stern (2015) and references therein). Abnormal buoyancy induced by plume-head weakening of the lithosphere would have initiated southwestward subduction and island arc formation in the trailing, western to southeastern edge of the CLIP (Whattam and Stern et al., 2015). This subduction drove the northeastward motion of the Caribbean plateau beneath North and South America, leading to episodic accretion of oceanic slivers and dextral transpression against the continental margin (White et al., 1999; Pindell et al., 2005; Montes et al., 2019; Montes and Hoyos, 2020, and references therein). In the Late Cretaceous, the leading edge of the CLIP and an overlying arc underwent collision, leading to fragmentation and clockwise rotation, which concluded in the early Maastrichtian period, approximately 70 Ma (Luzieux et al., 2006; Vallejo et al., 2009, 2019; Spikings et al., 2010). Shear sense indicators within the Calacalí-Pujilí-Pallatanga fault system in northern Ecuador (Hughes and Pilatasig, 2002) and paleomagnetic data supporting block rotations (Luzieux, 2007) provide evidence of a dextral motion related to the east-northeastward-oriented collision of the Caribbean Plateau.

The Late Cretaceous accretionary event led to the formation of a broad deformation zone spanning from Ecuador to Colombia. Within this zone, both submarine and onshore accretionary wedges are present as the continental and oceanic domains, as well as seismically active dextral faults such as the Dolores-Guayaquil megashear and the Peltec fault (Alvarado et al., 2016; DeMets et al., 2010; Mora et al., 2017; Pousse-Beltran et al., 2017). These dextral faults are believed to have initially formed a Campanian suture zone between the continental and oceanic basements subsequently reactivated during the Cenozoic. Subduction was reestablished following the early Eocene accretionary tectonic phase (Spikings et al., 2010; Aizprua et al., 2019). Thermochronological data (AHe and AFT) from the Western and Real cordilleras record cooling phases at ~65–55 and 43–30 Ma that were associated with Cenozoic accretion events and changes in plate kinematics that led to exhumation (Spikings et al., 2001, 2010).

Oligocene marked the onset of the continuous oblique subduction (Jaillard et al., 2009). High coupling along the northern Ecuadorian interface caused the NAS to begin to be pushed toward the northeast, driven by shear stress partitioning (Egbue and Kellogg, 2010; Nocquet et al., 2014). The NAS is bounded to the east by the long-lasting transpressive Chingual-Cosanga-Pallatanga-Puná (CCPP) fault system (Fig. 1A), defining the western limit of the South American plate (Ego et al., 1996b; Yepes et al., 2016). Direction changes in the Nazca plate convergence vector occurred at 26 and 20 Ma (Pardo-Casas & Molnar, 1987). In the Miocene, the NAS started its norward motion according to the tectonic model proposed by Alvarado et al., (2016) triggered by the oblique subduction at ~15 Ma. This shift led to the exhumation of the domains that make up the current Western Cordillera, Cordillera Real, and Interandean Valley, spanning from southern Ecuador to Colombia between 15 and 10 Ma (Alvarado et al., 2016; Steinmann et al., 1999; Spikings et al., 2000, 2001, 2010; Spikings and Crowhurst, 2004, Margirier et al., 2022).

In the Late Miocene of the Carnegie Ridge started the subduction under the South American Plate (e.g., Margirier et al., 2022, Brichau et al., 2021, Spikings et al., 2010), promoting strike-slip faulting, fault reactivation, and compositional changes in the magmatism (Egbue & Kellogg, 2010; Schütt & Whipp, 2020; Chiaradia et al., 2020). Strike-slip motion has been primarily accommodated by the CCPP fault system (Fig. 1A), active since at least the Miocene (Alvarado et al., 2016; Dumont et al., 2005). However, increased coupling at the plate interface after the subduction of the Carnegie Ridge may have caused the acceleration of the northward motion of the NAS as recently as the Pliocene to early Pleistocene (Deniaud, 1999; Witt et al., 2006; Spikings et al., 2010). Margirier et al. (2022) recently identified a cooling phase that commenced around 6-5 Ma in the Western Cordillera and which they associate with exhumation rates of ~0.5 km/Myr. They closely correlated this Late Miocene onset of exhumation with active shortening, rock uplift, and coeval exhumation in the Coastal Cordillera (Brichau et al., 2021) and the northern Cordillera Real, where~2.3 km of exhumation have occurred since 5.5-3.5 Ma (Spikings & Crowhurst, 2004; Spikings et al., 2010).

2.2.1. Oriente Basin

The Oriente Basin of Ecuador is an up to 4.5-km thick retroarc foreland basin with geographical continuity extending into the Putumayo Basin in southern Colombia and the Santiago-Marañón Basin in northern Peru. Horton (2018) utilizing sediment provenance and the correlation between facies and sediment accumulation rates suggests that the depositional cycle from the Cretaceous to the Paleocene represents a retroarc post-extensional (postrift) thermal sag basin, following a Late Jurassic-early Cretaceous extensional (synrift) basin phase (Fig. 3). The basin fill comprises basaltic to rhyolitic lava flows and pyroclastic materials originating from the late Jurassic Misahualli Formation, which in the NU area has been dated as 172.3 ± 2.1 Ma (amphibole Ar/Ar in andesite, Romeuf et al., 1995) and 162 ± 2 (Ar/Ar total fusion age in a rhyolite, Spikings et al., 2001). Vallejo et al (2021) present a U–Pb age of 148.34 ± 1.65 Ma in a high-level intrusion of the Misahualli Fm. approximately 250 km to the south, at ~3° S Lat. The Misahualli Formation can reach thicknesses of up to 600 meters and is distinguished by an unconformable contact with the over Lower Cretaceous Hollín Formation (Gutiérrez et al., 2019).

In the northern SAZ, the Aptian Hollín Formation comprises up to 180m-thick fluvial deposits, including basal alluvial valley fills, that unconformably overlie a previously incised basement of Jurassic and Paleozoic rocks (Gutiérrez et al., 2019). A Jurassic detrital zircon population and heavy mineral assemblages dominated by volcanic elements unambiguously document sediment sourcing from Jurassic arc rocks or recycling of strata thereof derived (Ruiz et al., 2007; Vallejo et al., 2021) in the lower Hollín Fm. The upper Hollín is characterized by ultrastable heavy mineral assemblages and Proterozoic zircons associated with eastern distal sources in the Amazon craton (Martin-Gombojav and Winlker, 2008 Gutiérrez et al., 2019; Vallejo et al., 2021). Upsection, the Napo Group is constituted of 240 to 600 m (Vallejo et al., 2004) of marine mudstones and limestones accumulated between the late Albian to the Campanian during sea-level highstand (Gutiérrez et al., 2019). In the southern Napo region near the city of Tena, well-log observations in the Pungarayacu oil field indicate a thickness of 600 meters for the Napo Formation (Rivadeneira & Baby 2004). However, estimating the thickness in the NU is challenging due to erosion or non-deposition of the Upper Napo, resulting in an erosional unconformity between the overlying Tena Formation and horizons as old as the Turonian-Coniacian M2 limestone of the Napo Group (Fig. 3). Dominant ultra-stable heavy mineral assemblages and detrital zircon U-Pb populations dominated by Proterozoic zircons as old as 2000 Ma unambiguously record provenance from the distal Amazon craton. Disconformably overlying the Napo Fm, the Maastrichtian to Paleocene Tena Formation is a 750-m thick redbed series that marks the end of the marine sedimentation within the Oriente Basin (Fig. 2). Gutiérrez et al. (2019) documented a detrital zircon population with a minimum age of 68.6 ± 3.5 Ma within sandstones of the Tena Formation. A marked upsection increase in volcanic heavy mineral assemblages (Vallejo et al., 2021) and the presence of abundant late Cretaceous zircons (70-90 Ma) derived from the Andean magmatic arc of document a sedimentary provenance polarity reversal and provide the first unambiguous record of a western source located in the present-day Western Cordillera (Gutiérrez et al., 2019; Vallejo et al., 2021).

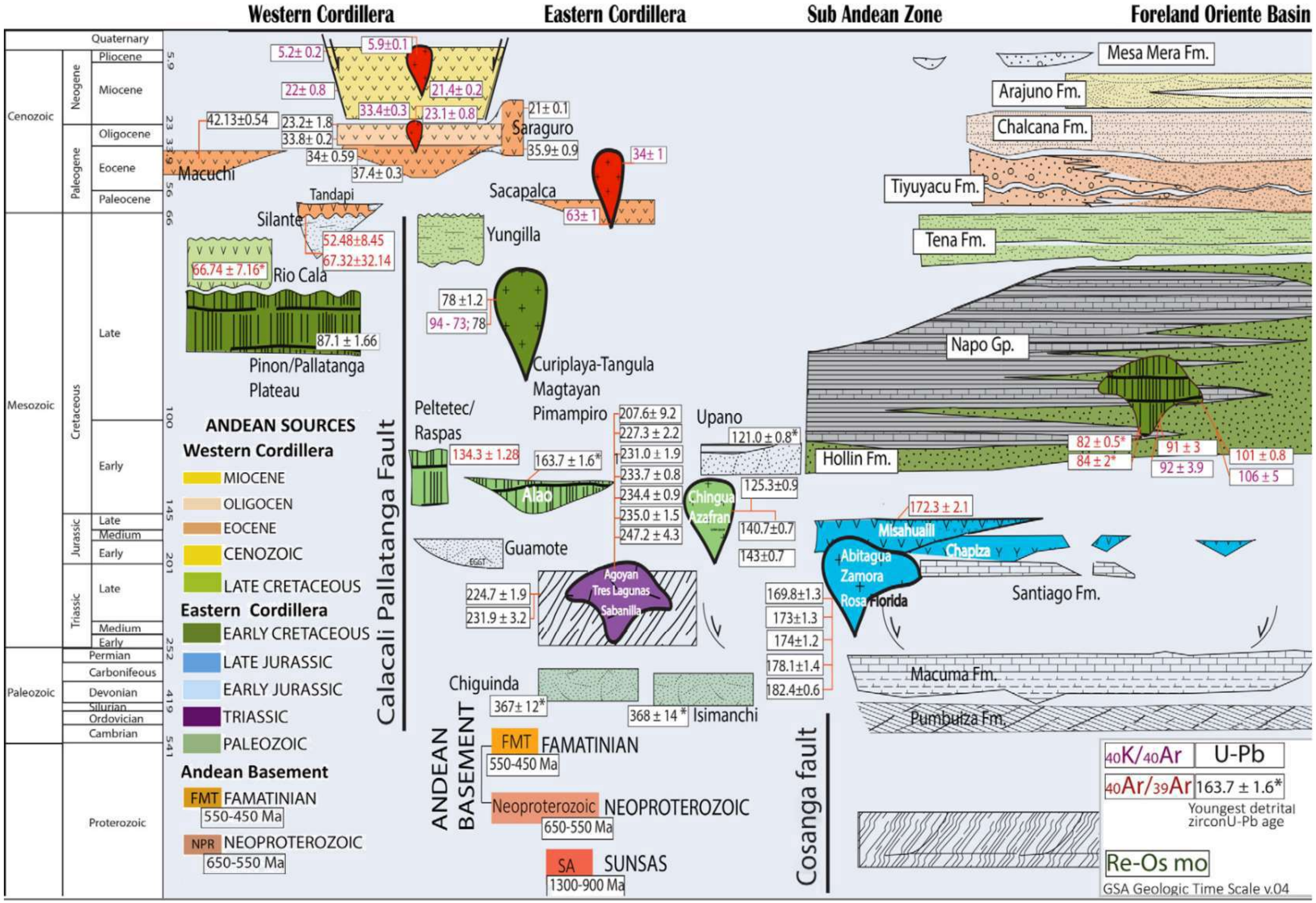

Fig. 3. Regional simplified stratigraphic framework for the Oriente foreland basin and Regional geologic column across the major lithotectonic provinces *modified* from Gutiérrez et al., (2019), and references therein.

The Eocene conglomeratic Tiyuyacu Formation was deposited in fluvial (lower member) and alluvial-fan (upper member) systems, both originating from the west, from the Andean Cordillera, although from a source that included Jurassic and Triassic zircons and no late Cretaceous, such as the Cordillera Real (Gutiérrez et al., 2019). The overlying Chalcana Formation (Roddaz et al., 2011), comprises 250 to 450 m of silty and sand dominated meandering fluvial strata accumulated in the Oligocene earliest Miocene. Gutiérrez et al., (2019) report a detrital zircon youngest population age of 22.8 ± 0.8 Ma from a sandstone of the Chalcana Fm. south of the city of Tena. On top of Chalcana, Miocene deposits include the Arajuno Formation, the eastern marine equivalent Curaray Formation, and the partially coeval Chambira Formation. The Arajuno and Chambira formations reach ~1000-1500 m, are separated by a minor erosional unconformity, and are constituted of sandy and gravelly meandering to braided fluvial channel deposits intercalated with floodplain deposits (Christophoul et al., 2002; Burgos et al., 2005; Roddaz et al., 2011). Gutiérrez et al., (2019) report a detrital zircon youngest population 17.6 ± 0.8 Ma in the base of the Arajuno and 13.3 ± 0.4 Ma towards the top. Finally, the Late Pliocene gravel deposits up to 200 m thick constitute the Mesa and Mera Formations and make part of the megafan from the Pastaza Depression.

2.3. Local Geological Settings

The area of study can be structurally sub-divided from west to east into (1) the 5-15 km wide SATB (Fig. 2; Litherland et al., 1994), and (2) the northern SAZ, including the Jurassic Abitagua batholith, the NU and its eastern frontal blind thrust structures.

2.3.1. The Sub-Andean Thrust Belt (SATB)

The SATB consists of imbricate and deformed Cretaceous units and green-schist metamorphosed rocks from the Jurassic Paradalarga Unit (J_P) (Buitron and Vallejo, 1999), and is limited to the west by the east-verging reverse Subandean Fault (SF). This fault marks the contact with the overthrusting front of the Cordillera Real (Pasquearè et al., 1990). To the east, SATB is bounded by the east-verging Cosanga Fault which juxtaposes the Jurassic metavolcanics Paradalarga against the Abitagua Batholith in the footwall south of S0°30', and against the Jurassic-Cretaceous cover of the NU north of it. The Cosanga Fault extends northward into the Quijos River valley, and displays predominantly reverse motion with an additional dextral lateral component, connecting to the Quijos fault segments. Pratt et al. (2005) propose that the Cosanga Fault underwent a significant reverse dip-slip of several kilometers during the Miocene-Pliocene.

2.3.2. Abitagua batholith

The Jurassic Abitagua batholith is a 120 km long and up to 15 km wide plutonic body located to the in the hanging wall block of the Cosanga Fault (Litherland et al., 1994), and is limited to the west by the Abitagua Fault. In the study area, the Abitagua batholith is topographically prominent, defining the highest non-volcanic elevation of the Northern SAZ at ~2700 m. This batholith is composed of pink, medium or coarse-grained biotite monzogranite to K-feldspar megacrystic biotite granite which has been dated by U–Pb in zircon at 170 ± 7 Ma (Vallejo et al., 2021) and shows no evidence of tectonic foliation or metamorphism.

2.3.3. The Napo Uplift (NU)

This broad anticline, 70 km-wide and 150 km-long, forms a structural culmination that rises about 1.6 km above the Amazonian foreland (Balseca et al., 1993). On its western side, it is flanked by Jurassic granitoids, including the Abitagua and Cuchilla batholiths in the Northern NU, whereas its southern sector is characterized by kilometric N-S trending folds (Fig. 4B). The NU is limited to the east by the transpressive Sub-Andean Front (SAF in Figs. 1A and 2) that has a reverse displacement with a maximum vertical offset of 1000 m according to well-log data (Rosero-Castillo, 1997; Baby et al., 2013). To the north of the NU, at 0°10´N, the Bermejo anticline constitutes the western part of a flower structure (Fig. 4A, see Fig 2 for localization) associated with the Sub-

Andean Front which was interpreted as the surface manifestation of a blind thrust (Balseca et al., 1993; Rivadeneria and Ramirez, 1985)

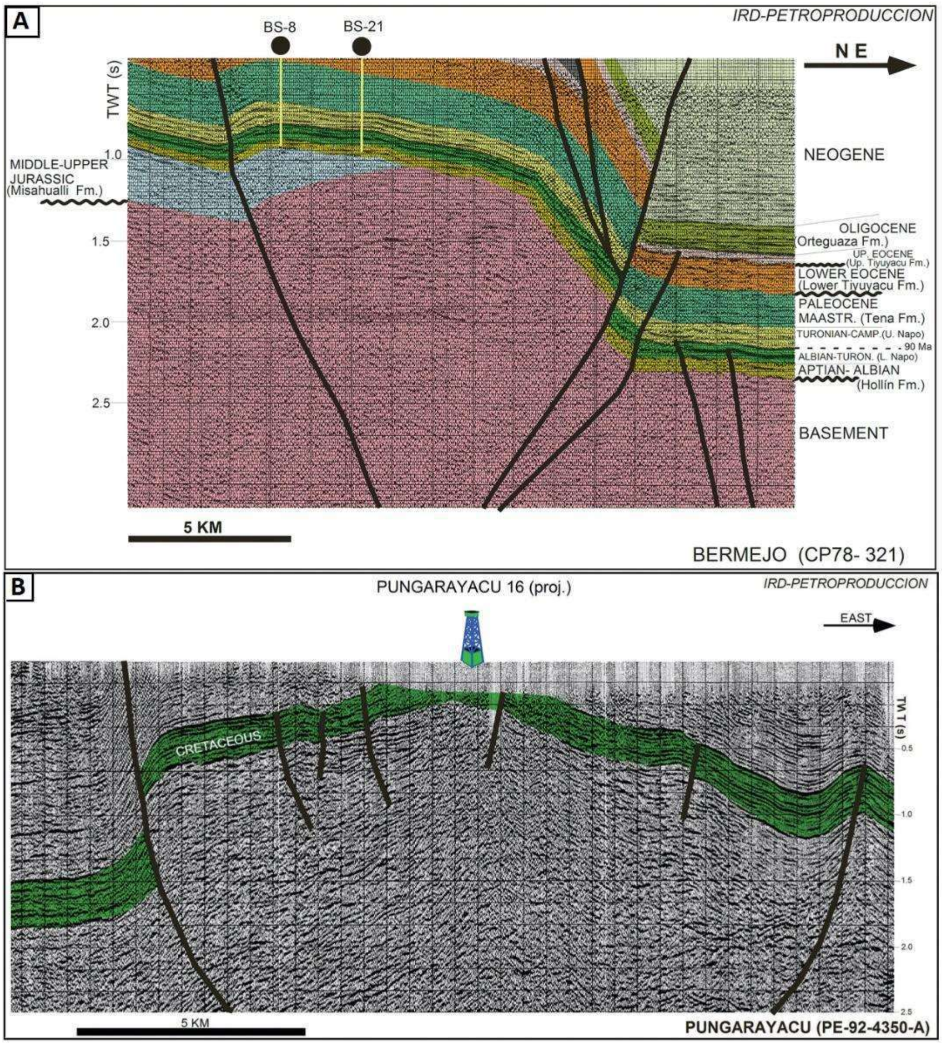

Fig. 4. Seismic profiles of the Bermejo oil field (A), and the Pungarayacu heavy-oil field (B); see location in the oil fields in Figure 2. Modified from Rivadeneira and Baby, (2004).

2.3. Previous thermochronological data.

In the Northern SAZ, north of 2°S and between the Subandean Fault (SF) and the Sub-Andean Front, Ruiz (2002) conducted a thermochronology study utilizing apatite (AFT) and zircon fission-track (ZFT) data. In this section, we described the AFT and ZFT published ages within our area of study in the Northern SAZ north of 1°17’S, from west to east, in the SATB, the Abitagua Batholith, and the NU (Fig. 9A).

Thermochronological data from Jurassic metamorphosed volcaniclastic sediments (Paradalarga Fm; Ruiz (2002)) in the SATB, sampled in the hanging wall of the Cosanga fault (Fig. 9A) included four relatively young AFT ages, ranging between of 2.5 ± 1.0 to 6.4 ± 1.8 Ma. These samples exhibited a long Dpar ranging from 2.6 ± 1.1 (n=10) to 3.2 ± 0.2 μm (n=24), and only two track length measurements of 14.4 and 15.1 μm. All of the young AFT ages reported in the SATB are from four samples in the vicinity of active volcanoes. However, Ruiz (2002) indicated that young AFT ages were not associated with active volcanoes but instead, that partial or complete resetting of the AFTages may have been influenced by the thick and hot cover of ignimbrites found in the Rio Quijos basin, which has since been eroded. However, the presence of a young AFT ages (Sample 09 (Jp) 2.8 ± 0.6 Ma) in the Paradalarga unit from an incised valley to the north, where no ignimbrites are reported, has been used by Ruiz (2002) to infer a direct link between the young AFT cooling ages in the Paradalarga unit and recent activity along the Sub-Andean Fault system. The ZFT ages obtained from this region in Jurassic volcanic and metamorphosed sedimentary rocks, ranging from ~46 to 55 Ma, are notably younger than the depositional ages.

Farther to the east, in the Abitagua batholith, three AFT ages with a range of 5.0 ± 1.8 to 161 ± 15.0 Ma have been reported. Dpar measurements or another kinetic parameter as chlorine content for these samples were not provided. The oldest AFT age of 161.0 ± 15.0 Ma exhibited a mean track length (MTL) of 10.3 ± 1.1 μm and a unimodal standard deviation of 3.6 μm. In contrast, the AFT ages younger than 82 Ma show MTL with narrower distributions, varying between 9.85 ± 0.33 μm for the oldest of the younger samples and 12.1 ± 1.7 μm for the youngest. Additionally, three ZFT ages ranging from 113.0 ± 12.0 to 176.0 ± 38.0 Ma from samples at 590-2150 m of elevation are reported. The youngest AFT and ZFT ages occur is the lowest-elevation sample 18(Ab).

In the Jurassic units along the NU, ages by Ruiz (2002) reveal a significant age disparity. North of ~0° 20’ S, younger AFT ages between 78.0 ± 14.0 and 116.0 ± 30.0 Ma with MTL of 10.8 ± 2.2 and 9.6 ± 1.3 μm occur. In contrast, the southern section of the NU exhibited older AFT ages, ranging between 133.2 ± 18.4 and 183.5 ± 15.1 Ma, with corresponding MTL of 11.8 ±

0.45 (n=12) and 11.86 ± 0.24 µm (n=59), respectively. Dpar or chlorine content were not available for these samples.

In the Cretaceous-Miocene strata of the NU, two AFT populations of 78.0 ± 6.0 Ma (P_1) and 142.0 ± 15.0 Ma (P_2) were obtained from a siltstone level of the lower part of the Maastrichtian to Paleocene Tena Fm. Also, a partially reset age of 19.3 ± 1.5 Ma was obtained from the lower Miocene Arajuno Fm.

3. SAMPLING AND METHODS

Low-temperature thermochronology methods provide insights into the thermal history of the Earth's crust, particularly in relation to cooling/heating events and their potential triggers like exhumation, heat flow changes and post-magmatic cooling (Malusa and Fitzgerald 2019, and references therein). Exhumation, which involves both rock uplift and erosion, can be inferred from these thermochronological data when combined with geological evidence (e.g., England & Molnar, 1990). AFT and AHe thermochronometers are valuable tools in this regard, as they are sensitive to temperature ranges spanning approximately 120°C to 60°C (e.g., Ault et al., 2019). In addition, detrital thermo/geochronology and geochemical tracing of apatites have been used to infer sediment source areas and hence document their uplift and exhumation. In particular, fission-track and U-Pb dating, coupled with patterns or rare earth elements have been recently used in provenance studies (O´Sullivan et al., 2020)

3.1. Samples

In order to investigate the low-temperature thermal and provenance histories of the NU, we present vitrinite reflectance data from 6 mudstones and 15 AFT, 8 AUPb, and 6 AHe analyses from a total of 17 bedrock samples. Sampling was performed along three E-W transects reaching from 2300 m.s.l. in the western, hanging-wall block of the east-vergent Abitagua fault to 300 m.s.l. in its footwall to the east. Sampling along the NU comprises Jurassic magmatic rock samples and Lower Cretaceous-Miocene sedimentary rock samples (Table 1).

Table 1. Samples collected in the NU from Jurassic magmatic and Lower Cretaceous-Miocene sedimentary rocks.

Sample	Unit	Lithology	Lat	Long	*Elev*	Stratigraphic Age (Ma)	Method
NA25	Chambira	Reddish sandstones	-1.2775	-77.8897	399	14.0 ± 1.0	AUPb
NA75	Arajuno	Lithic sands of medium grain	-1.1587	-77.8532	508	16.5 ± 6.5	AFT/AUPb

22NP20	Chalcana Fm.	Gray clayey sandstones	-0.8356	-77.4932	589	22.8 ± 0.8	AUPb
20111MS	Upper Tena Fm.	Reddish sandstones	-1.0303	-77.6668	395	68.6 ± 3.5	AFT/AUPb/Ahe
NJ82		Sandstones	-1.0648	-77.7914	470	68.6 ± 3.5	AFT/AUPb
NL68	Lower Tena Fm.	Phyllonites	-0.2340	-77.7677	1100	68.6 ± 3.5	AFT/AUPb
20109MS		Sandstones	-1.0243	-77.7965	464	84.0 ± 12.0	AFT/AUPb/AHe
NJ69		Green sandstones	-1.0502	-77.7921	447	68.6 ± 3.5	AFT/AUPb
22NP29		Reddish sandstones	-1.0175	-77.6709	399	68.6 ± 3.5	AFT
NL106	Lower Tiyuyuacú	Matrix-supported conglomerate	-1.07936	-77.79117	1937	68.6 ± 3.5	AUPb
22NP09	Misahualli Fm.	volcaniclastic sediments	-0.1298	-77.4462	754	160.0 ± 15.0	AHe
22NP05		Reddish volcaniclastic sediments	-0.0637	-77.5722	1633	160.0 ± 15.0	AHe
22NP21		Andesite	-0.6947	-77.7302	1030	160.0 ± 15.0	AFT/AUPb/Ahe
22NP04		Andesite	-0.1715	-77.6768	1294	160.0 ± 15.0	AFT/AUPb/Ahe
NL92		Porphyritic rock	-0.7255	-77.7621	1157	160.0 ± 15.0	AFT/AUPb
NA18		Andesite	-0.1416	-77.6260	1279	160.0 ± 15.0	AFT/AUPb
NL99		Crystal tuff	-0.6959	-77.7304	1021	160.0 ± 15.0	AFT/AUPb
22NP19		Sandstone and volcaniclastic sediments	-0.8324	-77.4994	672	160.0 ± 15.0	AFT/AUPb/Ahe
22NP25	Abitagua granite	K-feldspar granite	-0.6194	-77.8211	2137	172 ± 1	AFT/AUPb/Ahe

Age is the depositional or magmatic age of the rock; *Lat* is the south latitude and Long is the west longitude using the WSM 84 coordination system; *Elev* is the elevation in meters above sea level; AFT is apatite fission-track, AUPb is apatite uranium-lead and trace and rare earth elements, and AHe is (U–Th)/He in apatite.

The 17 bedrock samples were processed in the Thermochronology Laboratory (LTC) at the Institute of Geosciences (IGc) of the University of Sao Paulo. The samples were crushed and sieved to separate the 0.063 – 0.25 mm fraction, and subsequently, heavy minerals were concentrated by hydraulic separation using a water table. Magnetic grains were then removed using a Franz Isomagnetic Separator. This fraction was then cleaned with hydrogen peroxide and acetic acid to remove organic matter and carbonates, respectively, and subsequently dried in an oven at <50°C. Non-magnetic minerals underwent density separation in two steps. First, sodium polytungstate was used to separate minerals heavier and lighter than ~2.8 g/cm^3, and then, diiodomethane, with a density of 3.32 g/cm^3, is used to separate apatites (3.2 g/cm^3) from zircons. Since these samples were targeted for LA-ICP-MS fission-track analyses at GeOHeLiS analytical platform (GeOHeLiS) at the University of Rennes (France), we implement an analytical routine at LTC-USP for measuring densities of spontaneous tracks (Rho-S) in individual grains for fission-track (FT) analyses and recording grain coordinates so that later the grains can easily be identified during the LA-ICP-MS session at GeOHeLiS. The Olympus Stream Essentials software available at LTC-USP was used for recording by photography and measuring the areas in which NS were counted (Fig. 5-A). We used FTStage (Dumitru, 1993) to create a reference file that include mount coordinates for all analyzed grains, as well as for three reference points in each resin mount (P1, P2, and P3 in Fig. 3-B).

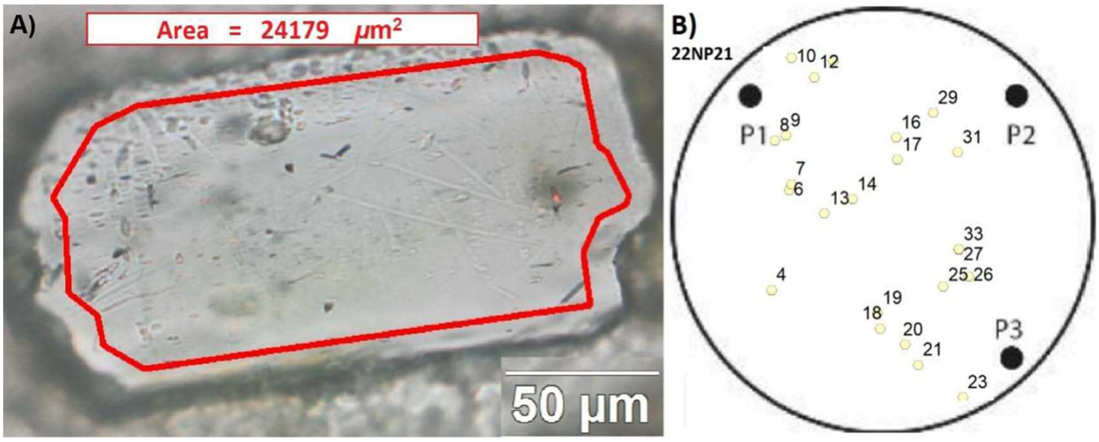

Fig. 5. A) Picture of apatite grain number 6 from sample 22NP21; B) Grain map with the location of pinholes (P1, P2, and P3) and the apatite grains (numbers).

3.2 Multi-elemental analyses on apatites using the LA-ICP-MS method

AFT, U-Pb, and trace elements analyses were carried out using Laser Ablation Inductively Coupled Plasma Mass Spectrometry (LA-ICP-MS) at the GeOHeLiS (9 samples) and the ChronusCamp Research Laboratory (Brazil) (6 samples).

LA-ICP-MS analyses in 9 samples were performed at the GeOHeLiS for the in-situ measurement of masses (^{35}Cl, ^{43}Ca, ^{86}Sr, ^{89}Y, ^{139}La, ^{140}Ce, ^{141}Pr, ^{146}Nd, ^{147}Sm, ^{153}Eu, ^{157}Gd, ^{159}Tb, ^{163}Dy, ^{165}Ho, ^{166}Er, ^{169}Tm, ^{172}Yb, ^{175}Lu,

^{204}(Hg + Pb), ^{206}Pb, ^{207}Pb, ^{208}Pb, ^{232}Th, and ^{238}U; see Appendix A) on apatite sample mounts. U/Ca ratios, determined using an ESI NWR193UC Excimer laser coupled to an Agilent 7700× Q-ICP-MS, were used to calculate the fission-track and U-Pb ages. Routinely, the analytical sequence in a laser ablation was performed using only one spot which size was ~35 μm (Fig. 4) with a repetition rate of 5 Hz and a fluence of 4 J/cm^2 (e.g. Cogné *et al*., 2014, 2016). The session consisted of interspersed analyses of approximately 8 sample grains, NIST 612 glass, Madagascar (MAD) (Thomson *et al*., 2012), Durango (McDowell *et al*., 2005), Synthetic (SynAp) and Mt. McClure (Schoene and Bowring, 2006) apatites. Further details on the analytical protocol are described in Cogné *et al*., (2020). All instrumental conditions are summarized in Appendix A.

3.2.1 Apatite fission track analysis (AFT)

Sample mounts were etched in 5 M HNO3 at 20 ± 1 °C for 20 s to reveal the spontaneous fission tracks and subsequently, densities of spontaneous tracks (Rho-S) were estimated using a Olympus BX-51 microscope at 1250X with dry objectives, and electronic stage, and the FTStage 4.0 software (Dumitru, 1993) at LTC-USP. Additionally, in order to reveal a greater number of spontaneous confined fission tracks for better inverse modeling, five additional sample mounts were sent to the University of Potsdam for performing ^{252}Cf irradiation. In addition, 6 samples were analyzed at Chronuscamp Research Lab with a similar protocol. Following etching, the daughter radiogenic product (i.e., the spontaneous track density) is calculated in up to 100 apatite or zircon grains in each sample by counting fission tracks and estimating surface areas in a LEICA DM6M optical microscope employing 1250x magnification for apatites.

The Uranium concentrations (^{238}U) for fission-track dating in the counted areas of apatite selected (Fig. 3) at LTC-USP were determined employing the LA-ICP-MS method, as described in the section 3.2 following the modified zeta approach described by Cogné *et al*. (2020). This method assumes that the apatite ^{43}Ca signal intensity during a given LA-ICP-MS session acts as a proxy for the volume of ablated apatite. An extensive primary LA-ICP-MS sequence was conducted on Durango apatite crystals previously counted for fission tracks to yield a primary LA-ICP-MS zeta factor. These same Durango apatite crystals were then analyzed in subsequent "unknown" LA-ICP-MS dating session to yield a session-specific fractionation factor. Artificial glass NIST 612 is used as a primary reference material to correct for LA-ICP-MS session drift. The raw isotope data were reduced using the software Iolite (Paton *et al*., 2011) with a modified version of the Trace_Elements DRS (Woodhead *et al*., 2007) and an in-house spreadsheet to calculate the zeta calibration factor with 2σ errors (ζ_{ICP} 0.770367376 ± 0.029786245) (see Appendix C). The ^{238}U/ ^{43}Ca ratio determination for fission track dating employed a slightly modified version [Trace Elements FTD, Cogné *et al*., (2020)] of the Trace Elements DRS (Woodhead *et al*., 2007).

The analytical routine used for 6 samples at Chronuscamp Research Laboratory also involved the measurement of the concentration of the parent isotope, ^{238}U using a direct determination of uranium content via mass spectrometry (LA-ICP-MS, Soares et al., 2014). For apatites, the LA-ICP-MS data was normalized using the ^{43}Ca/^{238}U ratios of standard samples (standard) and unknown samples (unk), using the following equation:

$$[U]unk = \{[(^{43}Ca/^{238}U)unk]/\ [(^{43}Ca/^{238}U)std]*(Ustd)\}$$

The standard sample MT-7 (7,5 µg.g-1 U – Soares et al., 2015) was used as Uranium standard sample for the apatites. To obtain the zeta parameter for calculating the AFT ages, the zeta calibration factor was determined using the Durango - DUR-2 sample (31.4 ± 0.44 Ma – McDowell et a., 2005; Soares et al., 2014; 2015). The LA-ICP-MS system consists of a Photon Machines 213 nm solid state Nd: YAG laser ablation system attached to an Agilent 7800 Quadrupole ICP-MS, located at the ChronusCamp Isotope Geology Research Laboratory (Itapira, Sao Paulo, Brazil). A gas mixer (Squid) is connected to the Laser Ablation system for better homogenization of the isotope mixture. The ablation spot size is chosen to cover the maximum area where the spontaneous fission tracks are previously measured. The laser analytical routine consists of three stages: 1) warm-up time, which is used as a background (15s); 2) dwell time, corresponding to the sample ablation time (45s); and 3) washout delay, which is used to clean the system before analyzing the next grain (30s). The data reduction is carried out using in-house developed spreadsheets. In addition to the U measurements necessary for fission-track analysis, the LA-ICPMS methods allows for simultaneous measurement of other elemental data in the same grain. In this work, we measured Pb isotopes, which enables to calculate a U-Pb age for apatites and rare earth elements.

3.2.2 Apatite U-Pb dating (AUPb)

The AUPb technique is based on the accumulation of radiogenic ^{206}Pb and ^{207}Pb from the radioactive decay of ^{238}U and ^{235}U series in apatites and the ensuing movement of lead (Pb) within the atomic structure of an apatite grain through heat-induced volume diffusion (Paul et al. 2019). This process offers insights into the thermal past of the apatite grain (Cochrane et al. 2014). Several studies have determined that the AUPb system's closure temperature ranges from approximately 550 to 450°C, depending on factors such as cooling rates and the size of the apatite crystals (Chew and Donelick 2012; Cochrane et al. 2014).

Isotopes $^{(204}$,^{206},^{207},^{208}Pb, ^{232}Th, and ^{238}U) measured through LA-ICP-MS were employed for determining AUPb ages (Table 2 and Fig. 7 in the results section). Madagascar apatite (MAD) crystals (reference age 474.2 ± 0.4 Ma, Thomson et al., 2012) were used as the primary reference material, while McClure apatite grains (Schoene and Bowring, 2006) were used for quality control. Data reduction was performed using the “VizualAge_UcomPbine” Data Reduction Scheme (DRS) in Iolite (Paton et al. 2011; Chew et al. 2014).

3.2.3 Apatite Trace Elements

Trace elements analyses on apatite are diagnostic of their host rock and a faithful recorder of the parent melt geochemistry (Sullivan et al., 2020). Trace element data reduction was performed using the X_Trace_Elements_ISDRS in Iolite (Paton et al. 2011) following Chew et al. (2016). Instrumental drift was corrected using NIST 612 as the primary standard and elemental concentrations were calculated using ^{43}Ca for internal standardization using stoichiometric abundance of Ca at 39.74 wt% (Chew et al. 2014). In addition, synthetic apatite (SynAp) was used for the high chlorine standard. Individual element concentrations for standards NIST 612 glass, MAD apatite, synthetic apatite (SynAp).

In order to approach host rock diagnostic and discriminate apatite provenance. Firstly, Chondrite-normalized rare earth element (REE) diagrams were plotted using de isotopic concentrations (normalized to chondrite) of ^{139}La, ^{140}Ce, ^{141}Pr, ^{146}Nd, ^{147}Sm, ^{153}Eu, ^{157}Gd, ^{159}Tb, ^{163}Dy, ^{89}Y, ^{165}Ho, ^{166}Er, ^{169}Tm, ^{172}Yb, and ^{175}Lu. Finally, Sr/Y versus light rare earth element (La-Nd) (ΣLREE) biplots (Fig. 8 in the results section) were plotted to discriminate broad apatite provenance, between six broad categories of apatite consistently identified by O'Sullivan et al., 2020) with various degrees of overlap: low-and medium-grade metamorphic apatite; high-grade metamorphic apatite; felsic granitoids; mafic granitoids and mafic igneous apatite; alkali-rich igneous apatite and ultramafic-carbonatitic apatite.

3.3 Apatite (U–Th-Sm)/He (AHe)

Following mineral separation, the best quality apatite grains were selected by hand-picking. Sixty inclusion- and fracture-free crystals were selected under a stereomicroscope Olympus SZX12 at 110X with polarized light, categorized according to their shape and size, their dimensions measured, photographed, and encapsulated in platinum tubes at LTC-USP.

We performed AHe analysis at GeOHeLiS on 35 single apatite grains, and 12 Durango apatite fragments placed individually into platinum baskets for use as a mineral age standard. The capsules with apatite single grains and Durango apatite fragments were heated twice by laser (~1050 °C for 5 min) for He-extraction. The gas purification system adapted for Apatite, consists of: an activated carbon, a titanium foam and its oven, 2 Getters SEAS GP50, and a "cold head" cryogenic trap with a minimum temperature of 10-12 ° K. The ^{4}He gas was mixed with a known ^{3}He spike, purified, and analyzed with a PrismaPlus QMG220 quadrupole mass spectrometer following an approach similar to that developed by Gautheron *et al.*, (2021).

Pt capsules with the grains were removed from the He extraction line, spiked with ^{235}U and ^{230}Th in 2% nitric acid, and left at 80°C for 48 hours in sealed Teflon beakers. ^{238}U, ^{235}U, ^{232}Th, and ^{147}Sm contents were measured by isotope dilution ICP-MS following methods described by Derycke et al. (2021). The AHe ages are calculated according to established procedures (Meesters and Dunai, 2005), and the ages corrected for alpha recoil (Farley *et al*., 1996; Ketcham *et al*., 2011; Gautheron and Tassan-Got, 2010).

3.4 Vitrinite Reflectance

Six samples of shales and one sample of coal (Table 1) were sent for vitrinite reflectance analysis to the Organic Geochemistry Laboratory at UFRGS, Porto Alegre. Organic matter was concentrated using conventional heavy liquids and a plug was created using a grain size range from 0.25 to 2 mm. The samples were grinded and polished for optical analysis following standardized procedures (Bustin et al., 1989). The measurements were taken between 15 and 100 points on each sample using a Microscope Leica DM6000 with a Photomultiplier Coupled to Reflected Light.

3.5 Thermal modeling

To provide a more regionally meaningful evaluation of the exhumation patterns in the study area, we integrate our new AUPb, AFT, and AHe data from 17 bedrock samples from the NU with 12 published AFT and 11 published ZFT ages from the Northern SAZ (Ruiz, 2002). Raw data and methodology details for the AFT and ZFT published data are presented in Appendix B. The thermal histories were determined through inverse modeling using the QTQt software, which inverts thermochronometric data using the Markov Chain MonteCarlo algorithm and known AFT annealing and AHe diffusion parameters (Gallagher, 2012). We used multi-sample modeling, which involves investigating a thermal history to account for both the thermochronometric data and spatial (i.e., paleodepth) distribution of several samples. The spatial distribution of new and published thermochronological data is obtained through projection of the stratigraphic position of each sample relative to the angular unconformity at the base of the Lower Cretaceous rift deposits, as deduced from map patterns, establishing a vertical profile for inverse modeling (Fig 14 in Results section; Appendix B).

The inversion code used in this study incorporates kinetic models for helium diffusion in apatite, as described by Flowers et al. (2009). Additionally, it utilizes a multi-kinetic annealing model for AFT, following the approach outlined by Ketcham et al. (2007), and the ZFT kinetic model of Tagami et al., (1998). The input parameters for each profile included AFT and ZFT grain count data, the distribution of track lengths kinetically projected along the c-axis, Dpar values, and the single-grain apatite AHe ages, along with information about grain sizes and grain geometry. The present-day temperature was set at 21±10 °C. and a temperature gradient was fixed at 30°C/km allowing offset to vary over time. For each thermal history, we ran at least 200,000 burn-in models (to reach an equilibrium state) followed by 200,000 post burn-in models, or more if model convergence was not achieved. The prior, i.e., the time temperature space allowed for models, was set to 300-0 Ma or 400-0 Ma, depending on the sample, and from 300-0°C allowing for onset of cooling associated to the Jurassic-recent Andean cycle.

Geological t-T constrains used included: 1) AUPb data and published ZFT data (Ruiz et al., 2002) to represent the time-temperature space corresponding to the extrusion or intrusion ages of Jurassic magmatic samples; 2) the stratigraphic or igneous age, based and compiled from Tschopp, (1953); Pratt et al., (2005); Dashwood and Abbotts, (1990); Baby et al., (2004); Baby et al., (2013); Horton, (2018); Gutiérrez et al. (2019), and Vallejo et al., (2021) and references therein; 3) an Upper Jurassic-Aptian exhumation event associated with the development of an unconformity between the Misahualli and the Hollín formations in the NU ($t = 125 \pm 10$ Ma and $T = 30 \pm 12$°C).

Inverse thermal modeling was conducted across three distinct lithotectonic provinces in the Northern SAZ: The SATB, the Abitagua Batholith, and the NU. One multiple-sample profile was utilized in inverse modeling for each province, except for the NU, where three models were generated for the Northern, Central, and Southern transects.

4. RESULTS

4.1. Apatite U-Pb Dating and Trace Elements

We obtained eight new apatite U-Pb (AUPb) ages from 4 Jurassic, 3 Cretaceous, and 1 Cenozoic samples from the NU (Figure 6). Isotopic data (^{238}U/^{206}U and ^{207}U/^{206}U ratios) plotted on a Tera-Wasserburg concordia space (Fig. 9A) allow to obtain lower intercept ^{238}U/^{206}Pb ages (Table 2, and Appendix D) ranging between 172.6 ± 16.6 to 285.2 ± 13.5 Ma (2-sigma errors, Table 2). AUPb ages from 3 Jurassic magmatic samples in the NU range from 172.6 ± 16.6 to 185.6 ± 26.0 and therefore correspond to the extrusion ages of andesites of the Misahualli Fm (Samples 22NP04 22NP21), or the crystallization ages of the Abitagua granite (Sample 22NP25). Sandstone sample 22NP19 yielded an unimodal AUPb distribution centered at 285.2 ± 13.5 Ma, without any Jurassic component, showing only a detrital component, without volcanoclastic input. In the Maastrichtian to Paleocene sedimentary samples of the Tena Fm (samples 20109MS, 22NP29, 20111MS), the AUPb ages range from 76.6 ± 15.7 to 90.9 ± 7.7 Ma (Fig. 7), most likely corresponding to syn-depositional apatite grains from the Andean magmatic arc. Finally, sedimentary sample 22NP20 from the Paleocene Chalcana Fm shows an age distribution with peaks at 250 and 435 Ma.

Table 2. Summary of AUPb data plotted in Tera–Wasserburg Concordia diagrams

Sample ID	*n*	^{238}U (ppm)	Age (Ma)	±2σ (Ma)	(^{238}U/^{206}Pb)$_c$	P (x2)	2σ (%)	(^{207}Pb/^{206}Pb)$_c$	2σ (%)	MSWD
22NP21	19	7.0	183.7	16.3	4.7	0.98	6.2	0.848	1.1	0.0
22NP04	23	6.8	172.6	16.6	5.9	0.35	5.6	0.849	1.5	1.1
22NP25	22	5.5	185.6	26.0	4.7	0.68	6.0	0.862	1.9	0.8

n = number of grains dated; 238U = average uranium concentration of the analyzed grains;); Age corresponds with lower intercept (Ma); P(χ2) = χ2 probability after (Galbraith 1981); MSWD is Mean Square of the Weighted Deviates for the isochron fit (sample detail can be found in Table 1)

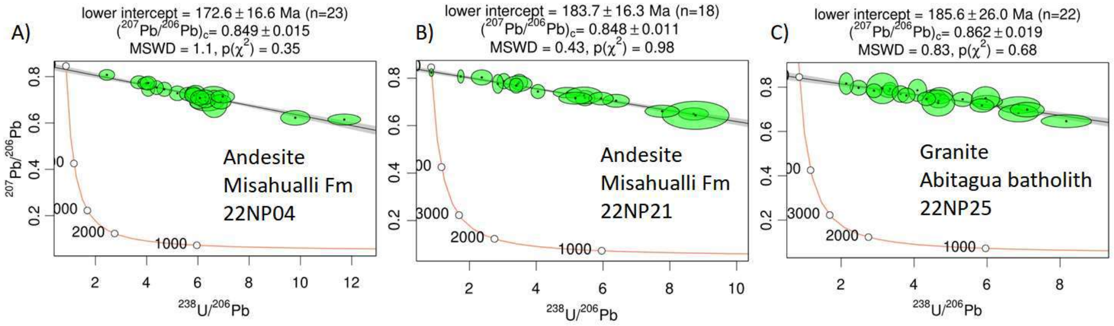

Fig. 6. Tera-Wasserburg concordia diagrams for: A) U–Pb apatite age of an andesite rock from the Misahuallí Fm (22NP04). B) U–Pb Apatite age of a Jurassic andesite rock from Misahualli Fm (22NP21) Formation, and directly underlying the Hollín Formation. C) U–Pb Apatite age of a granite of the Abitagua Batholith (22NP25). The lower intercept is considered as a mean U–Pb age.

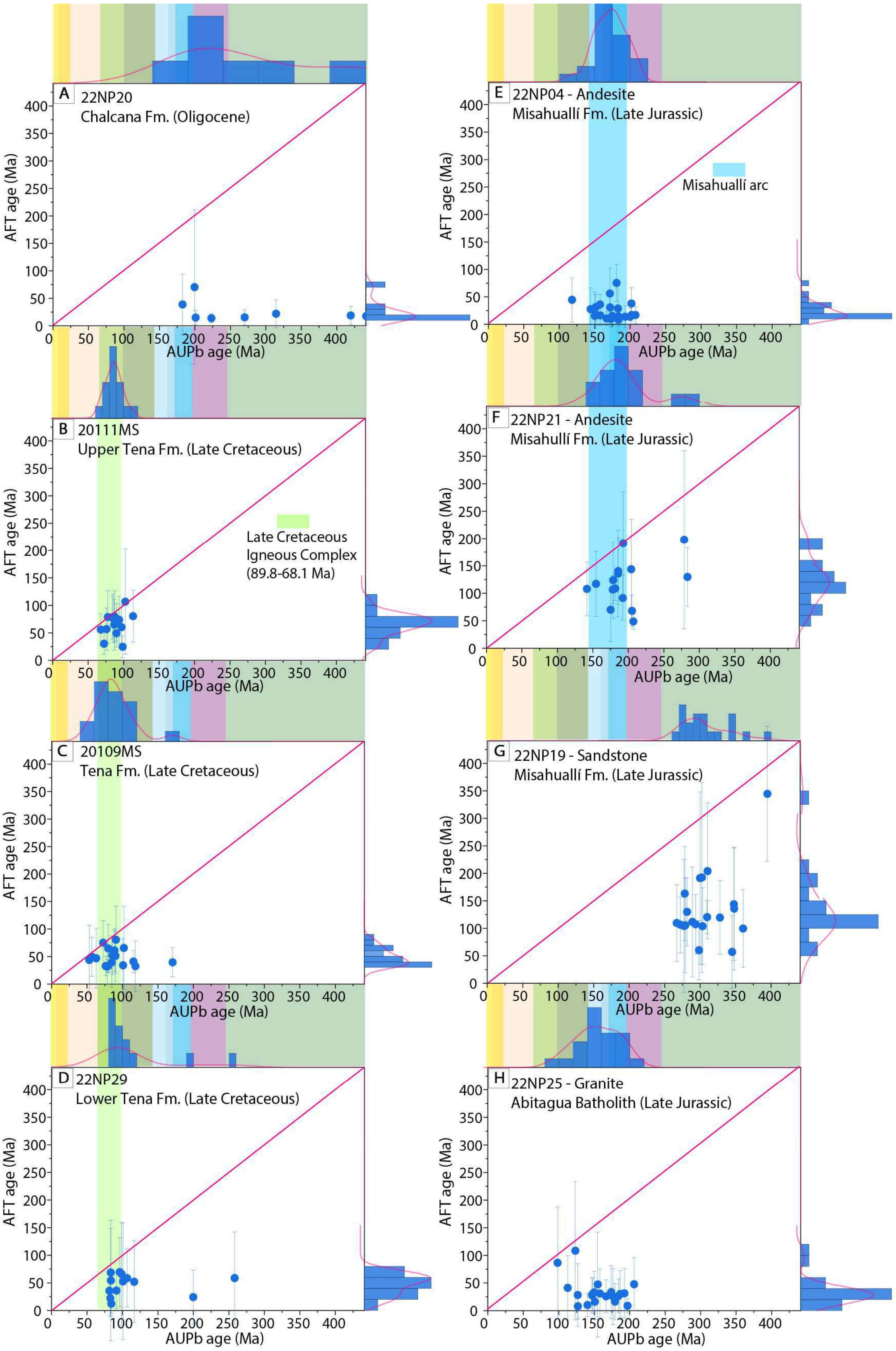

Fig. 7. Plot of AFT ages vs AUPb age with the respective histogram from Late Jurassic-Paleogene samples. Age histograms (blue bars) and probability density functions representing (above) the detrital apatite U–Pb geochronological results and (left) AFT ages. The samples are presented in stratigraphic order (A-H).

In sedimentary samples, apatite-trace element analysis using biplots of the Sr/Y ratio vs the sum of light rare earth elements La, Ce, Pr, Nd (ΣLREE) helps petrogenetically fingerprinting and hence understanding the provenance of apatite samples (O´Sullivan et al., 2020). We present REE geochemistry data from 7 Jurassic rocks, including 5 magmatic (22NP25, NA18, NL92, 22NP21, and 22NP04), 1 volcanoclastic (NL99), and 1 detrital (22NP19), 6 Cretaceous sandstones (20109MS, 22NP29, NJ69, NL68, NJ82, and 20111MS) and 4 Cenozoic sandstones (NL22NP20, NA25 and NA75). Apatite Sr/Y vs ΣLREE biplots allow discriminating apatite provenance from mainly four sources: 1) Low and medium-grade metamorphic apatite (LM) derived from the metasedimentary Andean basement, 2) High-grade metamorphic apatite (HM), from deeper levels of the Neoproterozoic-Paleozoic Andean basement, and 3) I-type granitoids and/or mafic igneous rocks (IM) sourced from the Andean arc, 4) Alkali-rich igneous apatite (ALK) and ultramafic-carbonatitic apatite (UM) from the Amazonian craton (Fig. 8).

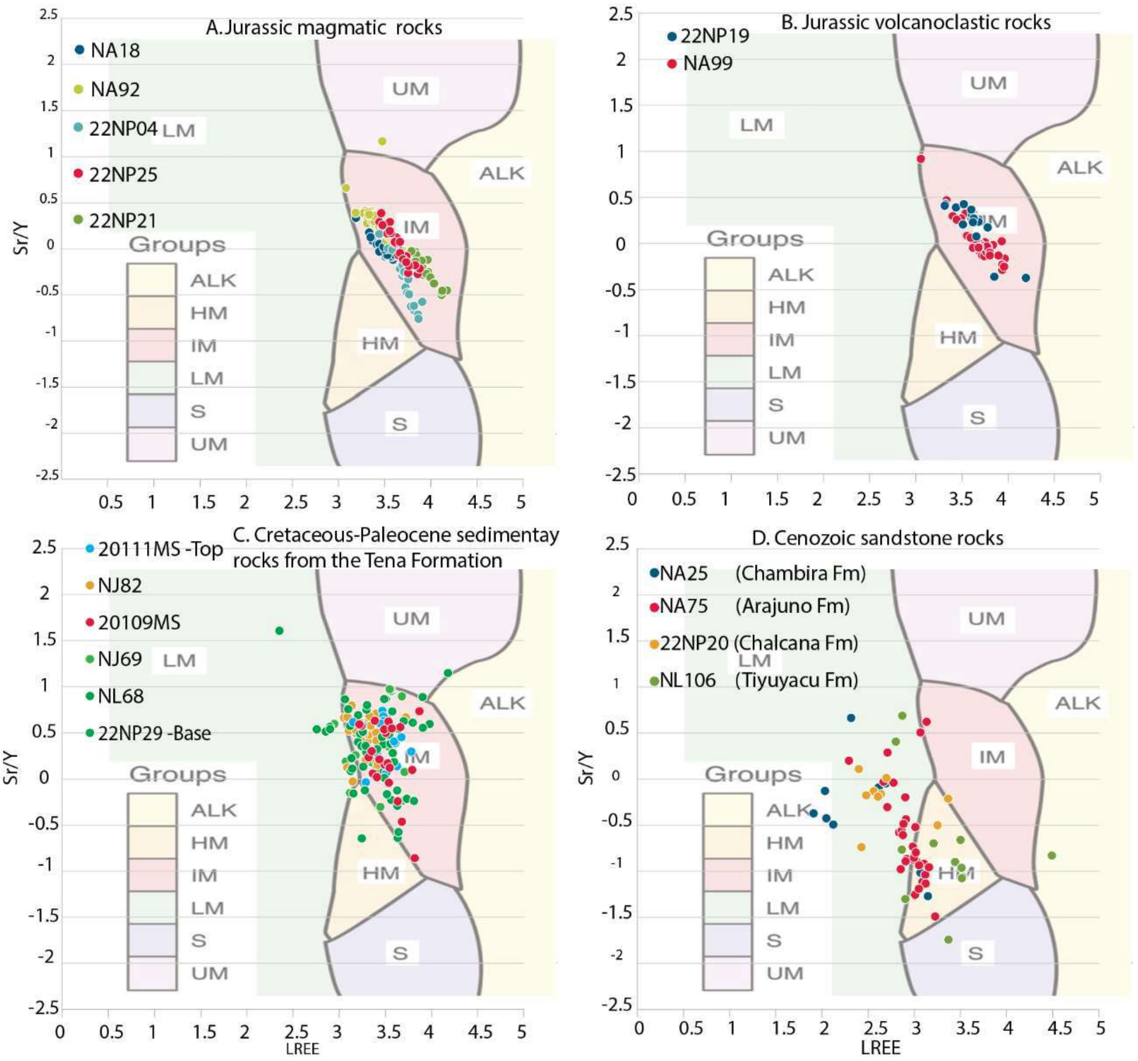

Fig. 8. Sr/Y vs ΣLREE (La-Nd) biplot from A) Jurassic magmatic rocks, B) Jurassic volcanoclastic and detrital rocks, C) Maastrichtian-Paleocene sedimentary samples from the Tena Formation, and D) Cenozoic sandstones rocks. Abbreviations for groups: ALK = alkali-rich igneous rocks; IM = mafic I-type granitoids and mafic igneous rocks; LM = low- and medium-grade metamorphic and metasomatic; HM = partial-melts/leucosomes/high-grade metamorphic; S = S-type granitoids and high aluminum saturation index (ASI) 'felsic' I-types; UM = ultramafic rocks including carbonatites, lherzolites and pyroxenites.

Jurassic magmatic samples show an enrichment in LREE compared to MREE (La/Sm$_N$ median values ranging from 3.65 to 2.54) and a moderate negative Eu anomaly (Eu/Eu* median values between 0.21 and 0.28 (Appendix F). Those patterns are characteristic of magmatic rocks with significant crustal assimilation (Gilby et al., 2020, O´Sullivan et al, 2020), as those corresponding to continental magmatic arcs. Moreover, petrogenetic fingerprinting using Sr/Y vs ΣLREE biplots shows that all apatites from Jurassic magmatic rocks fall into the IM field, which correspond to I-type granitoids and/or mafic igneous rocks (IM), as expected for the Andean magmatic arc (Fig. 8A). Likewise, apatites from the Jurassic sandstone (22NP19) and tuff (NA99) were also sourced from similar igneous sources (Fig. 8B).

In Cretaceous-Paleogene strata, the apatite samples exhibit a more varied distribution in the biplots. Remarkably, in the lower part of the Maastrichtian-Paleocene Tena Formation (NL68, NL69 and 22NP29; green points in Figure 8C) 78% of apatites correspond to I-type granitoid (IM) sources, while smaller proportions are associated with low-grade metamorphic (LM, ~12%), high-grade metamorphic (HM, ~7%), and ultramafic (UM, ~3%) sources. A first shift in apatite provenance appears upper the Tena Fm (20109MS, NJ82, 20111MS sample), where the distribution is less diverse and apatite sources are predominantly IM (>95%) (Fig. 8C). In contrast, in the Paleocene-Eocene Tiyuyacu Formation (Sample NL06), the primary population consists of HM sources (>50%), with a secondary population in LM (~20%), and minor populations originating from alkali-rich igneous apatites (ALK) and S-type granitoids (SM). Oligocene sample 22NP20 from the Chalcana Formation reveal a predominance of LM sources (>70%), despite the few numbers of grains analyzed (n=10). Miocene sample NA75 collected from the base of the Arajuno Formation (n=37) exhibits a majority of HM sources (~55%), followed by LM (~40%), and a smaller proportion in igneous and mafic sources (IM) (~5%). Finally, 10 grains analyzed in sample NA25, collected near the base of the Late Miocene-Pliocene Chambira Formation comprise 7 grains associated with LM sources and 3 with HM sources (Fig. 8D).

4.2. Low-Temperature Thermochronology

We sampled four volcanoclastic rocks Jurassic magmatic rocks and Lower Cretaceous-Paleogene sedimentary rocks along three structural cross sections in the north, center, and south of the NU (Fig. 9A), including the Abitagua Batholith, spanning an elevation range between 300 and 2300 m.s.l. The transects along the NU include profiles in the hanging walls of the Sub-Andean Front and Abitagua Faults (AF), and in the footwalls of the Cosanga Fault and the AF.

We present 18 new AHe single grain ages ranging from 2.0 ± 0.2 to 158.6 ± 15.9 Ma from 6 samples, and 15 new AFT ages ranging from 22.1 ± 6.3 to

220.7 ± 39.2 Ma, with a MTL between ~9 and ~14 μm (Table. 3). Additionally, 6 new vitrinite reflectance Ro (%) values between ~0.45 ± 0.11 and 0.55 ± 0.05 % are reported from Jurassic to Oligocene shale samples (Table 5).

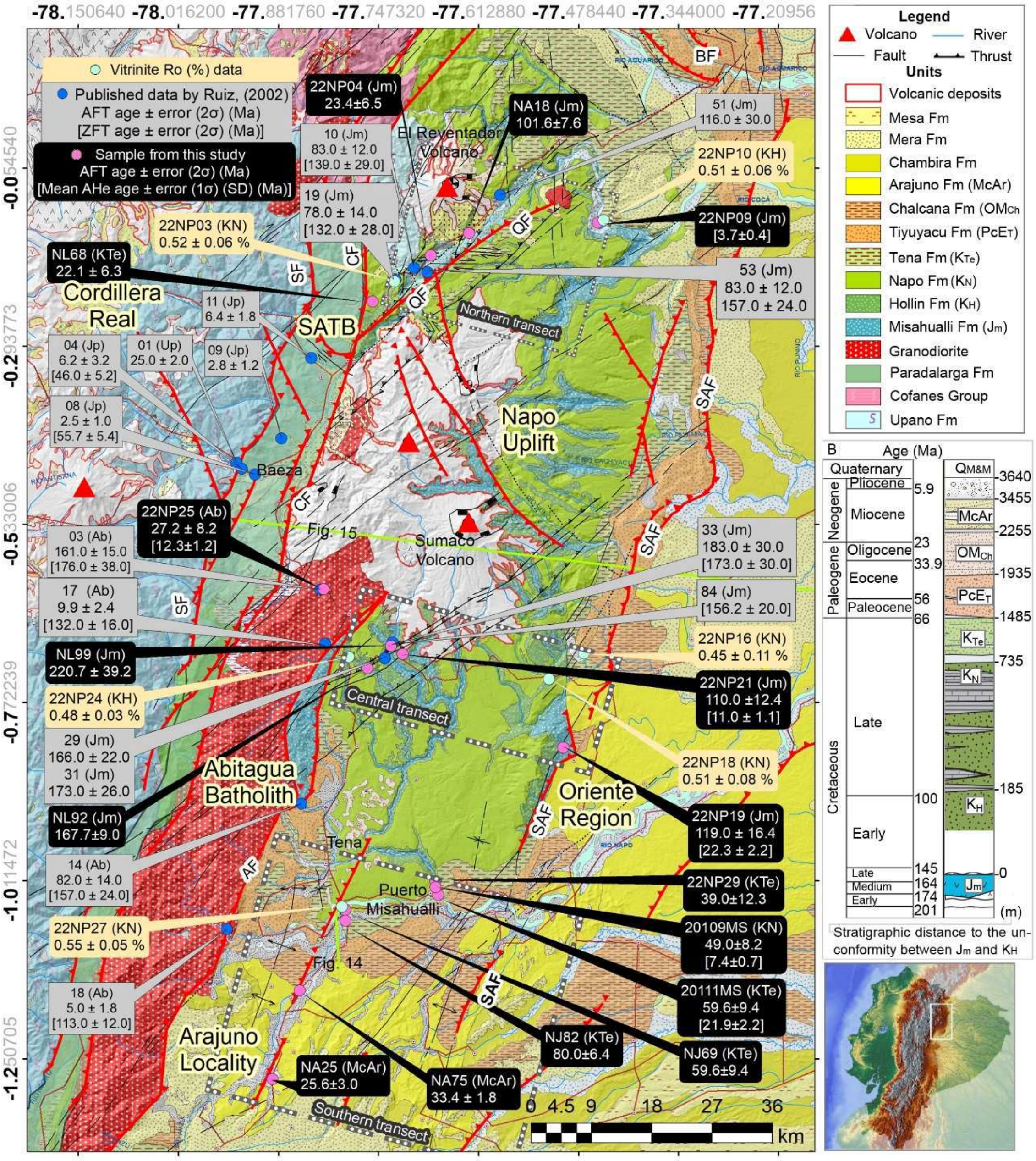

Fig. 9. (A) Geologic map of the NU modified from INIGEMM, (2014, 2016) showing the main faults and the location of low-temperature thermochronological samples. Red triangles denote volcanos; black boxes show the new AFT and/or AHe data in yellow points; grey boxes present AFT published data from Ruiz et al., (2002) in blue dots; yellow boxes show new values of vitrinite reflectance Ro (%) in green dots; AF is the Abitagua Fault, CF is the Cosanga Fault; QF is the Quijos Fault; SF is the Subandean Fault; SATB is the Sub-Andean Thrust Belt; SAF is Sub-Andean Front; **(B)** Stratigraphic column corresponds to Misahuallí Fm (Jm), Hollín Fm (K_H), Napo Fm (K_N), is the Tena Formation (K_{Te}), Tityuyacu Fm (PcET), Chalcana Fm (OM_{Ch}), Arajuno Fm (McAr), and *modified* from Gutiérrez et al. (2019) with stratigraphic thicknesses compiled from published data (references in section 3.4).

Table 3. Summary of Geochronological and Thermochronological Data from the Napo Uplift (*Ecuador)*

			Location [a]			LA-ICP-MS Apatite Fission Track data											Mean corrected AHe age [k] ± error (1σ) (SD) (Ma)	
Sample	**Unit**	**Lithology**	**Lat (°)**	**Long (°)**	**Elev (m)**	**n** [b]	**Ns** [c]	**Dpar (µm)**	***Cl*** [d] ***wt%***	**^{238}U** [e] **ppm**	**ρs** [f]	**P (χ^2)** [g]	**AFT pooled age ± error (2σ) (Ma)**	**AFT central age ± error (2σ) (Ma)**	**MTL**[h] **± error (1σ) (1 s.e.)** [i] **(µm) (n)** [j]			**Stratigraphic age (Ma**
Abitagua Batholith																		
22NP25	Abitagua granite (Ab)	K-feldspar granite	-0.6194	-77.8211	2137	21	44	1.7	0.6	5.5	0.7	0.76	27.2±8.2	32.7±9.8	12.4±0.2(4)		12.3±1.2	170.0 ± 0.7
Northern transect of the Napo Uplift																		
NL68	Lower Tena Fm. (K_{Te})	phyllites	-0.234	-77.7677	1100	37	55	-	0.9	6.6	1.2	0.00	20.0±2.4	22.1±6.3	11.3±2.5 (35)		-	68.6 ± 3.5
22NP09	Misahualli Fm. (Jm)	volcaniclastic sediments	-0.1298	-77.4462	754	-	-	-	-	-	-	-	-	-	-		3.7±0.4	165.0 ± 15.0
22NP04		Andesite	-0.1715	-77.6768	1294	23	126	2.1	0.3	6.8	0.7	0.00	22.8±4.1	23.4±6.5	11.7±2.1 (4)		-	165.0 ± 15.0
NA18		Andesite	-0.1416	-77.626	1279	40	208	-	0.6	6.0	3.3	0.96	101.6±7.6	108.7±15.5	9.3±2.0 (58)		-	165.0 ± 15.0
Central transect of the Napo Uplift													-				-	
22NP21	Misahualli Fm. (Jm)	Andesite	-0.6947	-77.7302	1030	15	377	2.7	1.4	7.0	2.8	0.17	110.0±12.4	112.7±12.1	10.6±1.1 (6)		11.0±1.1	165.0 ± 15.0
NL92		Porphyritic rock	-0.7255	-77.7621	1157	76	474	-	0.4	4.0	3.9	0.60	167.7±9.0	181.2±17.2	13.0±1.8 (120)		-	165.0 ± 15.0
NL99		Crystal tuff	-0.6959	-77.7304	1021	36	227	-	1.1	2.6	4.0	0.00	209.8±14.9	220.7±39.2	12.4±2.0 (67)		-	165.0 ± 15.0
22NP19		Sandstone and volcaniclastic sediments	-0.8324	-77.4994	672	19	234	2.3	1.0	7.5	3.1	0.83	119.0±16.4	122.4±17.3	11.4±1.3 (36)		22.3±2.2	165.0 ± 15.0
Southern transect of the Napo Uplift													-				-	
NA25	Chambira (McAr)	Reddish sandstones	-1.2775	-77.8897	399	10	77	-	0.0	51.7	13.0	0.38	25.6±3.0	27.7±7.2	11.8±2.2 (32)		-	14.0±1.0
NA75	Arajuno (Ar)	Lithic sands of medium-grain	-1.1587	-77.8532	508	30	419	-	0.0	51.7	13.0	0.33	33.4±1.8	32.8±3.6	11.7±2.1 (49)		-	17.6±0.8
20111MS	Upper Tena Fm. (K_{Te})	Reddish sandstones	-1.0303	-77.6668	395	15	171	2.7	1.9	9.1	2.5	0.27	59.6±9.4	63.1±9.7	13.4±1.6 (42)		21.9±2.2	68.6 ± 3.5
NJ82		Sandstones	-1.0648	-77.7914	470	40	193	-	1.4	5.9	3.0	0.99	80.0±6.4	79.9±6.0	14.3±2.4 (109)		-	68.6 ± 3.5

NJ69	Lower Tena Fm. (K_{Te})	Green sandstones	-1.0502	-77.7921	447	19	93	-	1.0	8.7	3.8	0.00	74.7±9.5	53.7±15.1	12.9±2.4 (18)	-	68.6 ± 3.5
22NP29		Reddish sandstones	-1.0175	-77.6709	399	13	41	2.2	1.2	10.4	1.4 E-5	0.80	39.0±12.3	43.7±13.7	-	-	68.6 ± 3.5
20109MS	Lower Tena Fm. (K_{Te})	Sandstones	-1.0243	-77.7965	464	18	152	2.3	1.1	11.2	2.7	0.63	49.0±8.2	46.3±8.4	12.8±1.9 (46)	7.4±0.7	68.6 ± 3.5

[a] *Longitude* and latitude coordinates are given in WGS 84 (degrees). [b] Number of grains dated. [c] Number of spontaneous tracks counted. [d] weight percentage of chlorine (Cl). [e] Average uranium concentration of the analyzed grains. [f] Average spontaneous track density (x10^5cm^{-2}). [g] χ^2 probability after (Galbraith 1981) [h] Corrected age is the age-corrected by the grain geometry and ejection factor FT (Ketcham et al., 2011). [h] MTL is the mean track length. [i] Standard error. [j] Amount of measured track lengths. [k] The mean value corresponds to a single grain AHe age. See Fig. 9A for location. In most samples, apatite separates were counted by D.R. Hernandez using zeta calibration (ζICP) of 0.6915 ± 0.0109, with the exception of samples in *italics*, where apatites were counted by ChronusCamp Research Lab using a zeta value (ζLA-ICP-MS Uppm) of 1750 ± 61.2

Intrasample dispersion of AHe ages was assessed following methods outlined by Fakuda et al (2020), whereby reproducible ages are defined as aliquots within 3σ of the weighted mean ages. Aliquots that do not fit these criteria are considered outliers (Table 4).

In the northern transect along the hanging-wall of the Quijos Fault, all the collected samples were volcaniclastic rocks from the Late Jurassic Misahualli Formation, except for sample NL68 from the Upper Maastrichtian-Paleocene Tena Formation. In this particular sample obtained from phyllites along the Cosanga Fault (Fig. 9A and 10A) was found the youngest AFT age in the NU. AFT data yielded a discordant age of 22.1 ± 6.3 Ma based on 37 grains, with an MTL of 11.3 ± 2.5 µm (35 TL), which can be divided into two kinetic populations P1 [11.8 ± 2.6 Ma (15 grains) and 12.98 ± 1.55 µ (15 TL)], and P2 (18.7 ± 3.3 Ma (22 grains) and 12.45 ± 2.05 µm (22 TL)]. Published AFT and ZFT ages in rocks of Paradalarga Unit along the hanging wall block of the Cosanga fault range between 2.8 to 25.0 and 46.0 to 55.7 Ma, respectively. No close constraints on maximum temperatures are available, but a pattern of younger thermochronological ages than stratigraphic/magmatic ages suggests significant thermal resetting.

In the Northern transect, the youngest AFT age within the Late Jurassic Misahualli Formation in the NU was found in an andesite rock sample (sample 22NP04 in Fig. 10A). This sample was collected at a paleodepth exceeding 500 m from the unconformity with the Aptian Hollín Formation. AFT data yielded a discordant central age of 23.4 ± 6.5 Ma, based on 23 grains, have two kinetic populations P1 [concordant age of 17.8 ± 4.6 Ma (18 grains), Dpar (1.52-2.23 µm) and only 5 measurement track lengths between 15.1 and 9.7 µm], and P2 [discordant age of 42.9 ± 14.9 Ma (5 grains) and Dpar (2.25-2.40 µm)]. Approximately 7 km to the northeast of this sample, another andesite rock sample (NA18 in Fig. 10A) from the same Late Jurassic unit was collected near the unconformity with the Aptian Hollín Formation, exhibiting an older concordant AFT age of 85.9 ± 7.4 Ma based on 40 grains. This sample has a mean chlorine content of 0.6 Wt%, higher than the younger sample 22NP04 with 0.3 Wt% (Table 3). This discrepancy suggests that sample 22NP04 underwent more burial than sample NA18, aligning with the paleodepth of both samples (Fig. 10A).

In the northeastern part of the Northern transect, a relatively young single-grain Apatite Helium (AHe) age of 3.7 ± 0.4 Ma was obtained from Jurassic volcanoclastic sediments (22NP09 in Fig. 9A). The sample exhibited an effective uranium (eU) concentration of 11.7 ppm and an equivalent spherical radius (ESR) of 68.8.

In the Jurassic volcanic and volcano-sedimentary rocks of the NU, thermochronological ages exhibit a marked north-south variation (Fig. 9A). In the north, all new AFT ages are younger than 101.6 ± 7.6 Ma (Fig. 10A), significantly younger than the rock formation age, with apatites being chlorine-poor (~0.4 Wt%), with mean Dpar of ~2.0 μm, and a short MTL of 9.1 ± 2.3 μm (in samples with more than 10 TL; sample NL18 in Table 3). These characteristics provide evidence of incomplete but significant thermal resetting during post-Aptian burial.

Table 4. Bedrock Apatite (U-Th)/He Age Data; (see appendix E for detailing AHe outliers' consideration)

Single grain	[b] **^{4}He / masse [nccSTP/g]**	**Mass (mg)**	[c]**FT**	**U ppm**	**Th ppm**	**Th/U ratio**	[d]**[eU] ppm**	**Ages uncorrected (Ma)**	**Corrected age ± 1σ (Ma)**	**Grain length (μm)**	**Grain half width (μm)**	[e]***ESR***	[f]**G.M**
20111MS-1	27323	6.28	0.75	7.1	38.6	5.4	16.4	13.8	18.4±1.8	166	53	62.8	1B
20111MS-3	83401	4.52	0.72	11.3	92.1	8.1	33.3	20.8	28.8±2.9	131	44	52.2	1B
20111MS-4	38890	6.54	0.78	13.4	66.6	5.0	29.3	11.0	14.0±1.4	235	59	72.8	1T
20111MS-5	40573	2.70	0.73	7.8	40.5	5.2	17.5	19.2	26.3±2.6	150	44	52.9	0T
20109MS-1	36095	9.22	0.82	20.6	81.5	4.0	40.2	7.4	9.0±0.9	222	66	79.2	1B
20109MS-2	9077	13.7	0.85	7.5	26.7	3.6	13.9	5.4	6.3±0.6	199	83	96.7	1B
20109MS-3	3657	7.42	0.78	10.7	37.8	3.5	19.8	1.5	2.0±0.2	222	61	73.1	0T
20109MS-4	32067	7.31	0.80	7.9	26.0	3.3	14.3	*18.6*	23.1±2.3[a]	221	58	70.3	1B
20109MS-5	120203	5.14	0.80	10.8	36.0	3.3	19.5	*51.1*	64.1±6.4[a]	148	59	69.2	1B
20109MS-6	93603	4.58	0.78	6.0	22.0	3.7	11.3	*68.6*	88.5±8.8[a]	218	50	62.2	1T-1B
20109MS-7	26678	3.84	0.77	13.6	40.0	2.9	23.2	9.5	12.4±1.2	195	50	61.2	1T-1B
20109MS-8	*He blanc*	3.21	0.77	18.2	76.6	4.2	36.4	<4.2	-	164	50	59.9	1B
22NP09-2	4090	6.26	0.79	6.5	21.2	3.3	11.7	2.9	3.7±0.4	213	57	68.8	2B
22NP19-1	*He blanc*	2.79	0.71	5.7	27.3	4.8	12.3	<19.5	-	145	45	53.6	0T
22NP19-2	16760	5.53	0.71	5.8	19.1	3.3	10.5	13.2	18.5±1.9	158	45	55.2	1T
22NP19-3	*He blanc*	2.42	0.74	2.5	11.7	4.6	5.6	<21.8	-	152	46	56.1	1T-1B
22NP19-4	*He blanc*	4.88	0.78	4.1	14.3	3.5	7.7	<8.2	-	184	54	64.7	1B
22NP19-5	*He blanc*	2.87	0.73	3.8	17.1	4.6	8.0	<13.2	-	191	48	60.8	2T

22NP19-6	38755	4.50	0.76	2.9	11.9	4.1	5.8	*55.5*	72.8±7.3[a]	203	48	58.5	1B
22NP19-7	10180	3.89	0.73	2.2	8.9	4.0	4.4	19.1	26.2±2.6	200	47	56.8	0T
22NP21-1	21958	6.12	0.81	7.2	37.9	5.2	16.6	10.9	13.6±1.4	161	63	74.0	1B
22NP21-3	20066	2.17	0.71	6.7	87.2	13.0	28.0	5.9	8.4±0.8	168	46	58.3	2T
22NP21-5*	77790	2.94	0.73	8.7	40.5	4.6	18.8	*34.3*	47.1±4.7[a]	203	47	59.7	2T
22NP21-6*	*He blanc*	3.58	0.74	2.8	14.5	5.1	6.6	*17.4*	23.5±2.3[a]	200	44	53.9	1B
22NP25-1	43164	3.92	0.77	21.2	66.8	3.2	37.4	9.6	12.5±1.2	165	51	60.4	1B
22NP25-2*	49168	7.20	0.81	6.5	19.6	3.0	11.2	*36.3*	44.8±4.5[a]	189	65	77.0	1B
22NP25-3	18584	4.95	0.81	8.0	19.0	2.4	12.7	12.1	15.0±1.5	173	57	67.2	2B
22NP25-4*	26411	2.77	0.76	4.0	15.0	3.8	7.7	*28.3*	37.4±3.7[a]	153	49	59.6	1T-1B
22NP25-5*	138398	6.16	0.82	5.2	14.0	2.7	8.9	*129.4*	158.6±15.9[a]	198	58	68.9	2B
22NP25-6*	34645	5.78	0.82	8.3	14.9	1.8	12.1	*23.7*	28.9±2.9[a]	180	58	68.8	2B
22NP25-7	9293	5.99	0.79	4.5	14.4	3.2	8.1	9.5	12.0±1.2	207	56	66.9	1B
22NP25-8	*He blanc*	7.24	0.79	3.2	9.4	3.0	5.6	<4.7	-	241	61	74.0	1B
22NP25-9	*He blanc*	4.99	0.81	3.1	9.6	3.1	5.6	<10.3	-	171	55	65.3	2B
22NP25-10	14788	8.61	0.89	4.0	15.3	3.8	7.9	15.6	17.5±1.7	91	101	99.5	2B
22NP25-11	3812	3.60	0.77	5.1	14.5	2.9	8.7	3.7	4.7±0.5	182	46	55.9	2B

[a] Grain age regarded as an outlier. [b] Ratio of ^{4}He volume in cubic centimeters at standard temperature and pressure (nccSTP) to the mass of the substance in grams (g), in this column *He blanc* means that the grain had lower helium content than the mass spectrometer can measure. [c] FT is the a-ejection correction after Farley et al. (1996). [d] Effective uranium concentration (U ppm + 0.235 Th ppm) (Shuster et al. 2006). [e] ESR is the equivalent spherical radius. [f] Grain morphology: 0T = no terminations, 1T = one termination, 2T = two terminations (Brown et al. 2013)

Table 5. Samples analyzed for vitrinite reflectance analysis (Ro (%) average and coefficient of variation (CV).

Sample ID	**Long.**	**Lat.**	***Elev (m)***	**Lithology**	**Unit**	**Maximum depositional age (Ma)**	**n**	**Ro (%) average**	***S error (%)***	***CV (%)***
Northern transect of the Napo Uplift										
22NP03	-77.7259	-0.2064	1546	Laminated black shales	Napo Fm	90.0 ± 8.5	57	0.52	0.06	12
22NP10	-77.4447	-0.1239	980	Black mudstones	Hollín Fm	118.6 ± 1.2	50	0.51	0.06	12
Central transect of the Napo Uplift										
22NP16	-77.4714	-0.7058	530	Mudstones interbedded with claystones	Napo Fm	90.0 ± 8.5	22	0.45	0.11	24
22NP24	-77.7876	-0.7106	1186	Gray mudstone	Hollín Fm	118.6 ± 1.2	21	0.48	0.03	6
Southern transect of the Napo Uplift										
22NP18	-77.5184	-0.7402	1009	Laminated black shales	Napo Fm	90.0 ± 8.5	50	0.51	0.08	16
22NP27	-77.7965	-1.0458	464	Shales	Hollín Fm	90.0 ± 8.5	31	0.55	0.05	9

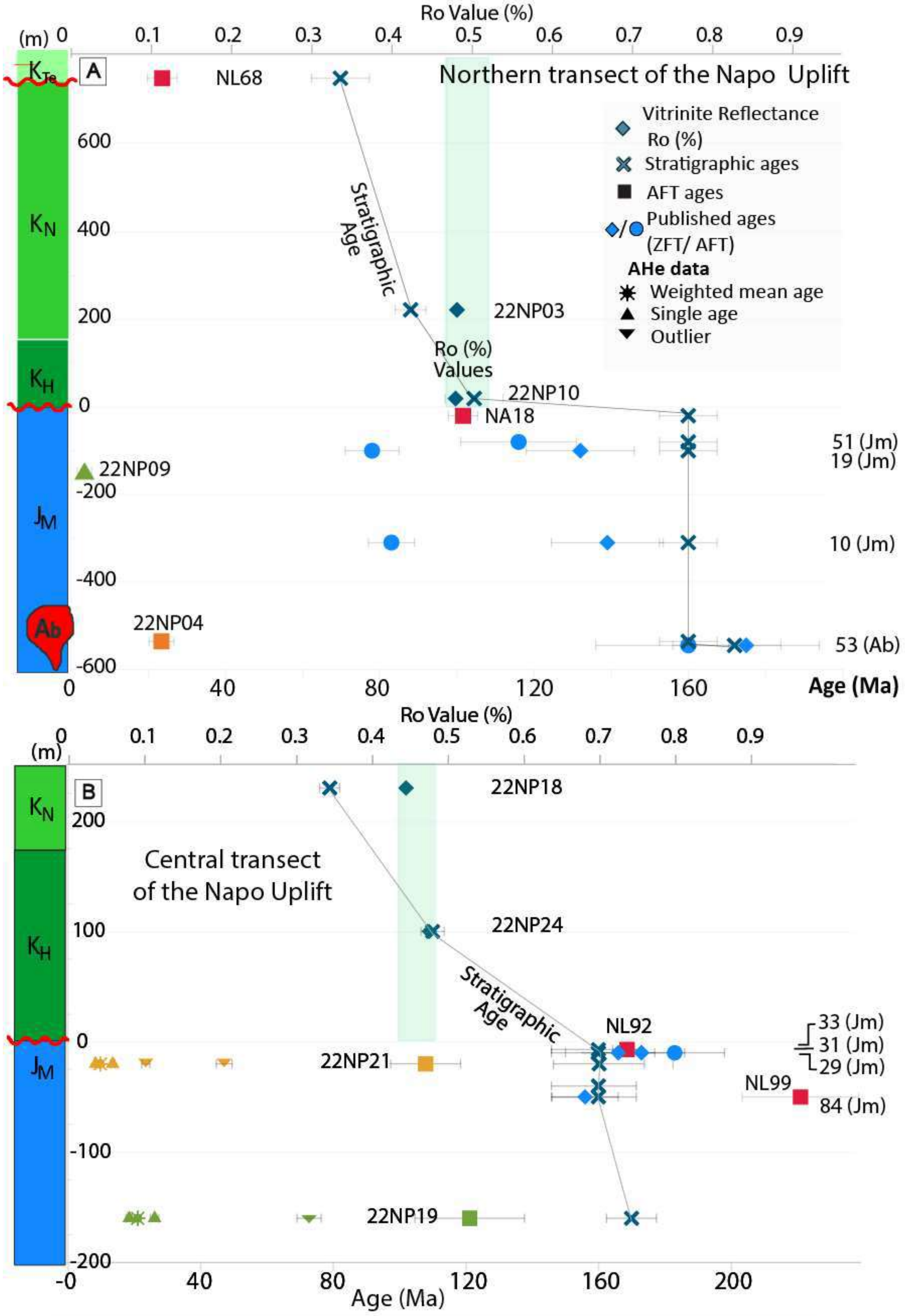

Fig 10. New thermochronological (Table 3) and vitrinite reflectance (Ro) data, and published data (Ruiz, 2002) for samples from the Northern **(A)** and Central **(B)** transects from the NU (see Fig. 9A for location) plotted against the stratigraphic position referred to the base of the Cretaceous rift-related units.

Conversely, in the central transect of the NU, the AFT ages of Jurassic samples 22NP21, NL99 and 22NP19 in the footwall of the Abitagua fault exhibit a range between 110.0 ± 12.4 and 220.7 ± 39.2 Ma, with porphyritic sample NL 92 yielding a concordant AFT age of 167.7 ± 9.0 Ma, which overlaps with the Jurassic volcanic age (Figs. 6A, 6B and 10B; Table 2). It is worth noting that all other Jurassic-basement samples, except for sample NL92, feature apatites rich in chlorine (ranging from 0.9 to 1.3 Wt%, Table 3). These apatites also present longer MTL values of 12.4± 2.0 µm and a Dpar ranging between 2.3 and 2.6 µm (Table. 3). The kinetic features, the close alignment of AFT ages with the Jurassic volcanic age and the presence of intermediate track lengths allow for a reliable approximation of the depositional age, which has been only minimally modified by moderate degrees of annealing. Available ZFT are from nearby Jurassic volcanoclastic rocks (Ruiz, 2002) ranging between 173.0 ± 30.0 to 156.0 ± 20.0 Ma (Fig. 10B), which further suggest that (1) zircons are mainly sourced by Jurassic volcanic units and (2) post-depositional thermal resetting is negligible.

In summary, the northern NU exhibits a higher degree of fission-track annealing Jurassic samples during post-Aptian burial in compared to the central transect of the NU. Additionally, Ro values higher than 0.51 ± 0.06% (78°C) were reported in the northern section, while in the central transect of the NU, Ro values reached up to 0.45 ± 0.11% (65°C) (Figs. 9A and 10; Table 3). Furthermore, two weighted mean AHe ages of 9.8 ± 0.7 and 21.1 ± 1.5 Ma in the central transect are also older compared to the youngest AHe age in the north, which is 3.7 ± 0.4 Ma (sample 22NP09 in Fig. 9A; Appendix E).

In the Central transect, Jurassic sandstone sample 22NP19, collected in the less accessible hanging wall block of the Sub-Andean Front Fault (Fig. 9A), at a distance between 100 and 200 m beneath the unconformity with the Hollín Formation represents the easternmost Jurassic thermochronologic data in the NU. Detrital AFT data yield a concordant age of 119.0 ± 16.4 Ma based on 19 grains with a short MTL of 11.4 ± 1.3 µm (n=36) suggesting a moderate degree of thermal resetting. In addition, in the same transect but on its western side, the Jurassic andesite sample (22NP21) yielded a concordant age of 110.0 ±12.4 Ma based on 14 grains with a shorter MTL of 10.6 ± 1.1 µm (n=6) than the detrital sample of the same unit (22NP19), but a longer mean Dpar of 2.7 µm.

Sample 22NP25 from the Jurassic Abitagua Batholith yielded a concordant AFT age of 27.2 ± 8.2 Ma, with a short mean Dpar of ~1.7 µm and a low chlorine content of 0.6 Wt%. Only 4 track measurements were reported with an MTL of 12.4 ±0.2 µm. We also report five reproducible single-grain AHe ages, ranging from 4.7 ± 0.5 to 17.5 ± 1.8 Ma without age vs eU or grain size correlations (Violet points in Figure 12). A weighted mean age of 7.6 ± 0.8 Ma (Fig. 11).

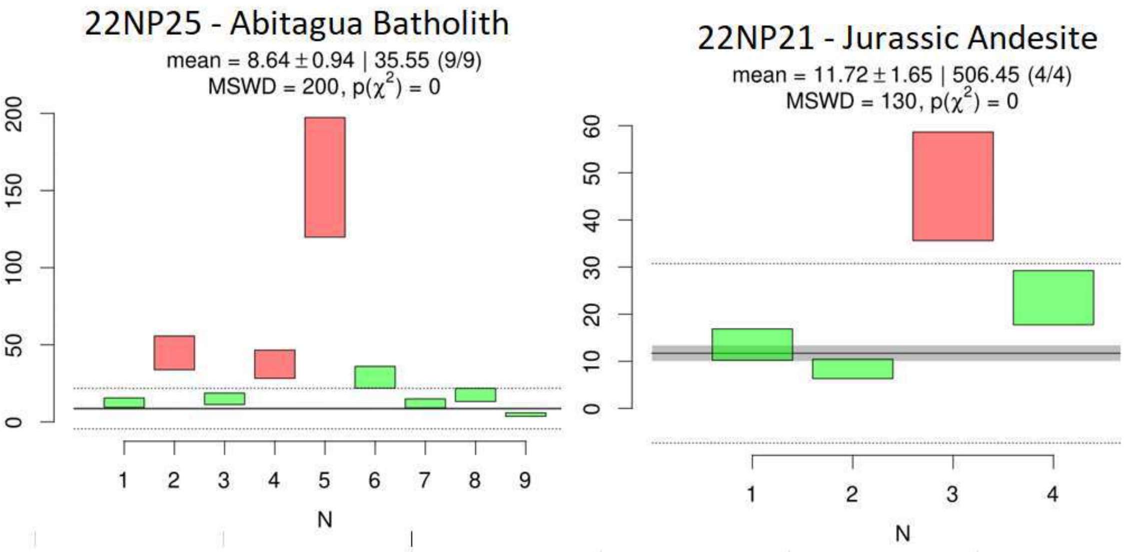

Fig. 11. Weighted mean AHe ages and minimum ages within ± 95% confidence intervals for the Jurassic magmatic sample (22NP25) to the left, and for the Jurassic andesite sample (22NP21) to the right. Red boxes are grain considered outliers.

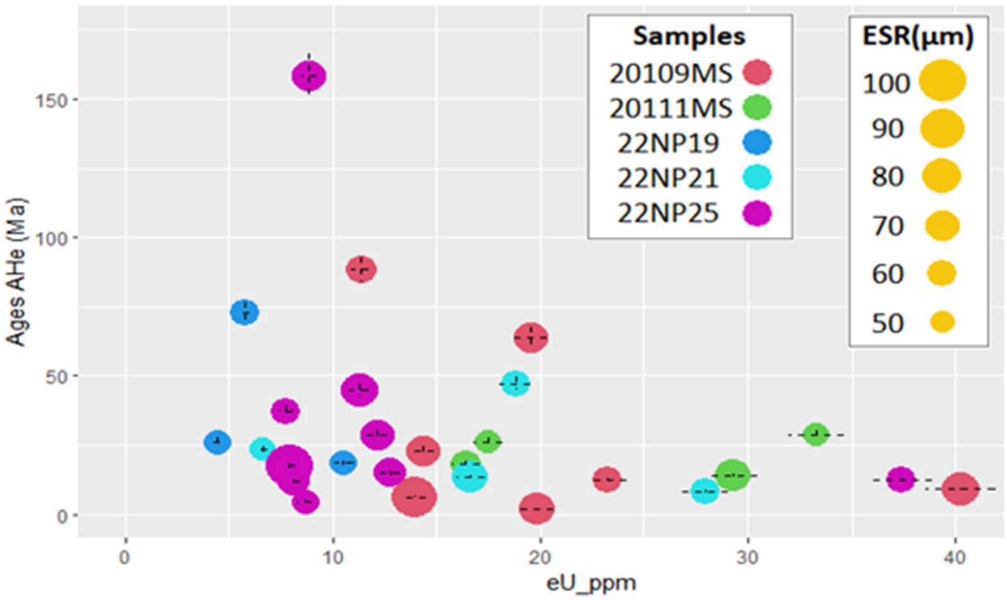

Fig. 12. Effective uranium (eU) ppm versus AHe grain ages (with errors indicated by ± 3σ), circle size represents the equivalent spherical radius.

In the Southern transect of the NU, including the Arajuno Locality (Fig. 9A), we conducted AFT and AHe analyses on the Maastrichtian-Paleocene Tena Formation and Miocene Arajuno Formation units east of the Abitagua fault. Additionally, vitrinite reflectance analysis was performed on the Cretaceous Napo Formation. The sandstone samples from the Maastrichtian-Paleocene Tena Formation (22NP29, 20111MS, 20109MS, NJ69, and NJ82) in this region exhibit chlorine-rich apatites (0.9 - 1.9 Wt%) and MTL ranging between 11.7 ± 2.1 and 14.3 ± 2.4 μm. In the upper Tena Formation near the city of Tena, sample NJ82 yielded a concordant AFT age of 80.0 ± 6.4 Ma (n=40) with an MTL of 14.3 ± 2.4 μm (n=109), suggesting older age and longer tracks than the sample NJ69 from the base of the unit (discordant age of 53.7 ± 15.1 Ma, MTL of 12.9 ± 2.4 μm), indicating lesser thermal resetting towards the top of the formation. About 15 km to the east along the hanging wall of the Sub-Andean Front Fault, near Puerto Misahuallí (Fig. 9A), sample 20111MS from the upper Tena Formation yielded an older concordant AFT age of 59.6 ± 9.4 Ma, with a longer MTL of 13.4 ± 1.6 μm (n=42), compared to a younger concordant AFT age of 39.0 ± 12.3 Ma from the base of the unit (sample 22NP29). In general, comparing lower with upper Tena Formation samples, the lower Tena samples (22NP29, 20109MS, and NJ69) yielded younger ages (53.7 ± 15.1 to 39.0 ± 12.3 Ma), shorter MTL and Dpar values (12.8 ± 1.9 to

12.9 ± 2.4 µm, 2.2 to 2.3 µm, respectively), and lower mean chlorine content (1.0 to 1.2 Wt%). Conversely, upper Tena Formation samples (20111MS and NJ82) yielded older AFT ages (concordant ages of 59.6 ± 9.4 and 80.0 ± 6.4 Ma), longer MTL (13.4 ± 1.6 and 14.3 ± 2.4 µm), longer Dpar values (2.7 µm), and higher mean chlorine content (1.9 and 1.4 Wt%). These findings collectively indicate a pattern of lower thermal resetting for the upper Tena Formation.

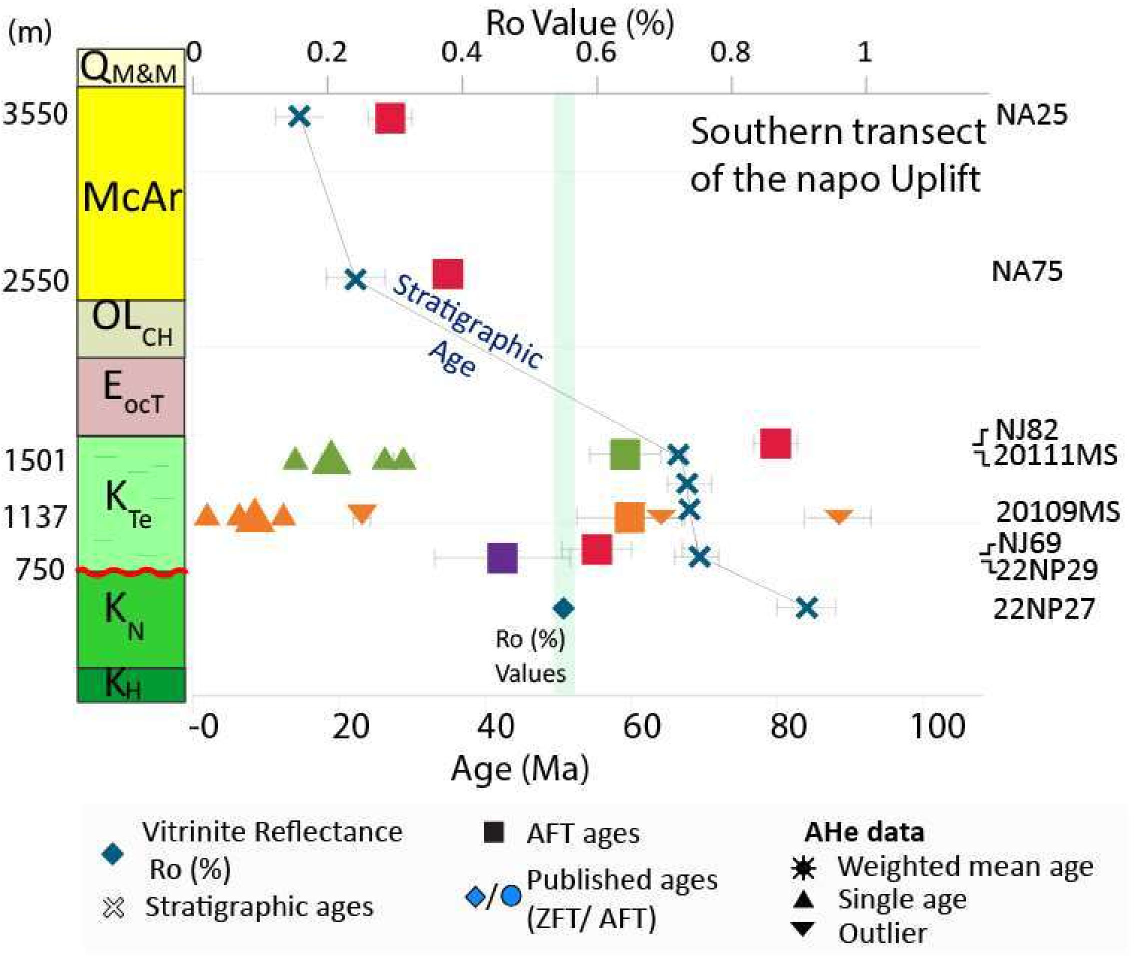

Fig. 13. New thermochronological (Table 3) and vitrinite reflectance (Ro) data, and published data (Ruiz, 2002) for samples from the Southern transect from the NU (see Fig. 9A for location) plotted against the stratigraphic position referred to the base of the Cretaceous rift-related units; bigger triangles represent Mean AHe age without outliers.

Furthermore, four AHe single grain ages from a sandstone sample (20109Ms) from the middle sector of the Maastrichtian-Paleocene Tena Formation show higher grain-age dispersion, including young ages between 2.0 ± 0.2 and 12.4 ± 1.2 Ma. In contrast, four AHe single grain ages in sample

20111MS from the upper part of Tena Fm are clustered at 21.9 ± 2.2 Ma (Fig. 13; Table 4).

Vitrinite reflectance data from sample 22NP27 (Table 5) collected from interlayered Cretaceous mudstone in the Napo Fm, underlying all samples analyzed for thermochronology along this transect, yielded a Ro value of 0.55%, which corresponds to a temperature of 94-103°C for moderate heating rates of 1-5°C/My (Sweeny and Burnham, 1990). This temperature range provides a maximum for the Cretaceous section and reveals that the AFT system in all Cretaceous and Cenozoic samples was never fully reset.

Further towards the south of the Southern transect, in the Arajuno locality (Fig. 9A), sample NA75 from the base of the Miocene Arajuno Fm yielded a concordant AFT age of 33.4 ± 1.8 Ma (n=30), with an MTL of 11.7 ± 2.1 µm (n=49). Finally, sample, NA25, collected from the overlying late Miocene Chambira Formation, close to its basal contact above the Arajuno Fm (Fig. 9A) also yielded a concordant AFT age of 25.6 ± 3.0 Ma (n=10), and a short MTL of 11.8 ± 2.2 µm (n=32). Remarkably, both of these samples have AFT ages older than their corresponding stratigraphic Miocene ages, which, in combination with their shorter MTL values, indicates a process of partial resetting attributed to Miocene heating to temperatures within the apatite APAZ (>60°C).

4.3. Thermal History Modeling

We present results of multi-sample inverse thermal modeling from different morphotectonic domains in Northern SAZ, including from west to east the SATB in the Cordillera Real, the Abitagua Block (Cordillera de Guacamayo), and finally the NU, where we analyzed in three transects (Figs. 9A and 15). Details on thermal modeling methods are provided in Section 3.5. Instead of topographic elevation for each sample, structural depths were estimated with respect to the sub-Cretaceous unconformity using geologic maps, as shown in Figure 14. The exhumation in all profiles was calculated assuming a surface temperature of 21 ± 10°C and a thermal gradient of 30°C/km, taking into account the apparent thermal gradient for the Northern SAZ calculated statistically by Angulo-Romero et al., (2023) based on borehole temperatures

(BHT) from the Oriente Basin, including the Pungarayacu, Oglan, and Bermejo fields.

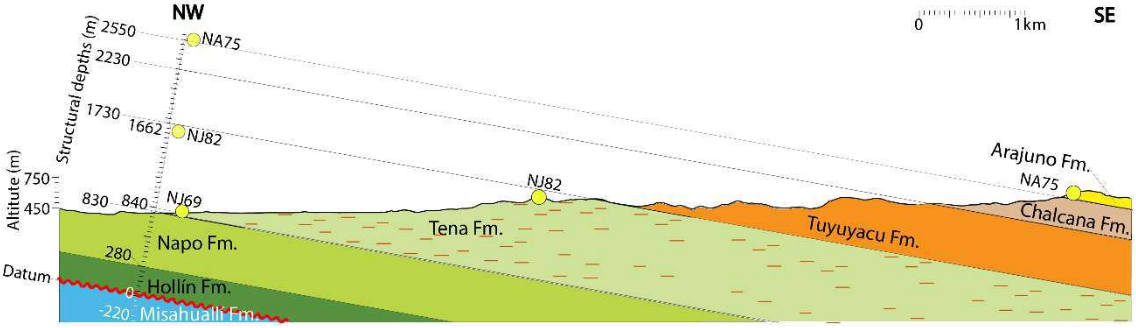

Fig. 14. Geological profile across the eastern part of the Southern transect (see Figure 9A for location) illustrates the approximate structural depths (Appendix B), estimated with reference to the unconformity between the Hollín and Misahuallí Formations; details on stratigraphic thickness are provided in Section 2.2.1.

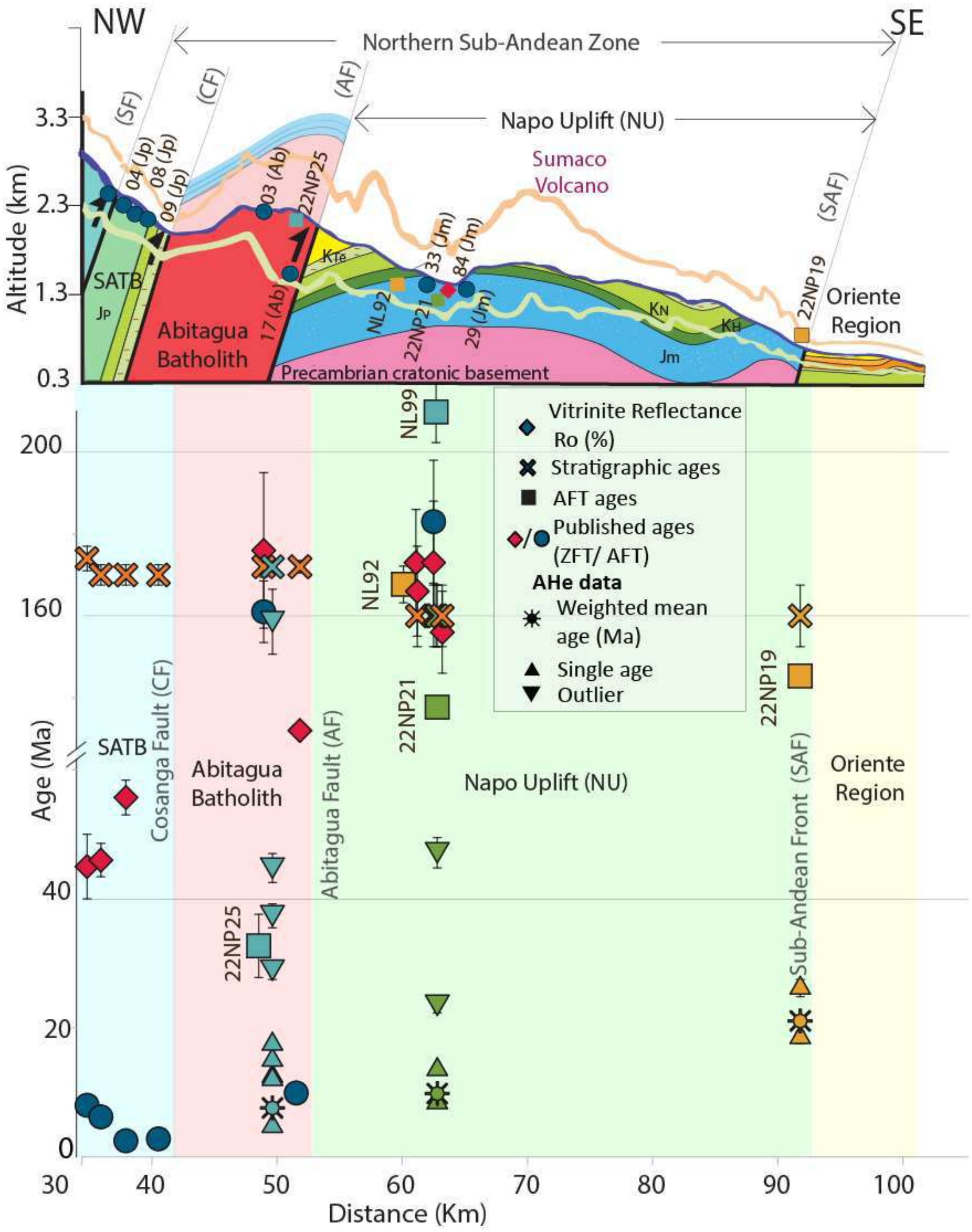

Fig. 15. Topography, simplified structural and geological section across the Northern SAZ (E-W at ~S0°29' Lat; see Figure 9A for location), and new and published thermochronological data are shown**. (A)** A 40-km-wide topographic swath (SRTM-90 based on Copernicus GLO-90 DEM) profile showing maximum, mean, and minimum elevation, as well as projected thermochronological samples for the Central transect. **(B)** Cooling ages (2s error) and stratigraphic ages.

In the SATB, we used information from published samples from the metavolcanic-sedimentary Paradalarga Formation obtained by Ruiz (2002). Based on lithostratigraphic correlations, the Paradalarga Fm has been considered time-equivalent of the Upano Fm in the Cordillera Real. Gutiérrez et al. (2019) report a detrital zircon youngest population age of 121 ± 0.8 Ma in rocks of the Upano Fm in the vicinity of the village of Baeza. They include 4 AFT ages ranging from 2.5 ± 1.0 to 6.4 ± 1.8 Ma, with two track lengths of 14.3 and 15.1 µm, and 2 ZFT ages of 46.0 ± 5.2 and 55.7 ± 5.4 Ma (Fig. 15 and 9A). A geological constraint derived from U-Pb data is the residence at surface temperature conditions during early Cretaceous time (120-125 Ma). Time-temperature paths from the SATB recorded three phases of rapid cooling (Fig. 16A) since the Eocene. The first phase of moderately rapid cooling started between 65 and 55 Ma from temperatures below the ZPAZ, which may be overestimated due to the use of the kinetic model of Tagami et al (1998) for modeling. A second phase, of slower cooling from temperatures of ~280°C to ~100°C, started at ~50 Ma and was followed by the third phase at ~7-6 Ma from temperatures between 132 and 122°C, resulting in an accelerated cooling rate between 13 and 20°C/My. This young phase accommodated between 3.0 and 4.0 km of exhumation, with rates of ~0.43-0.67mm/y.

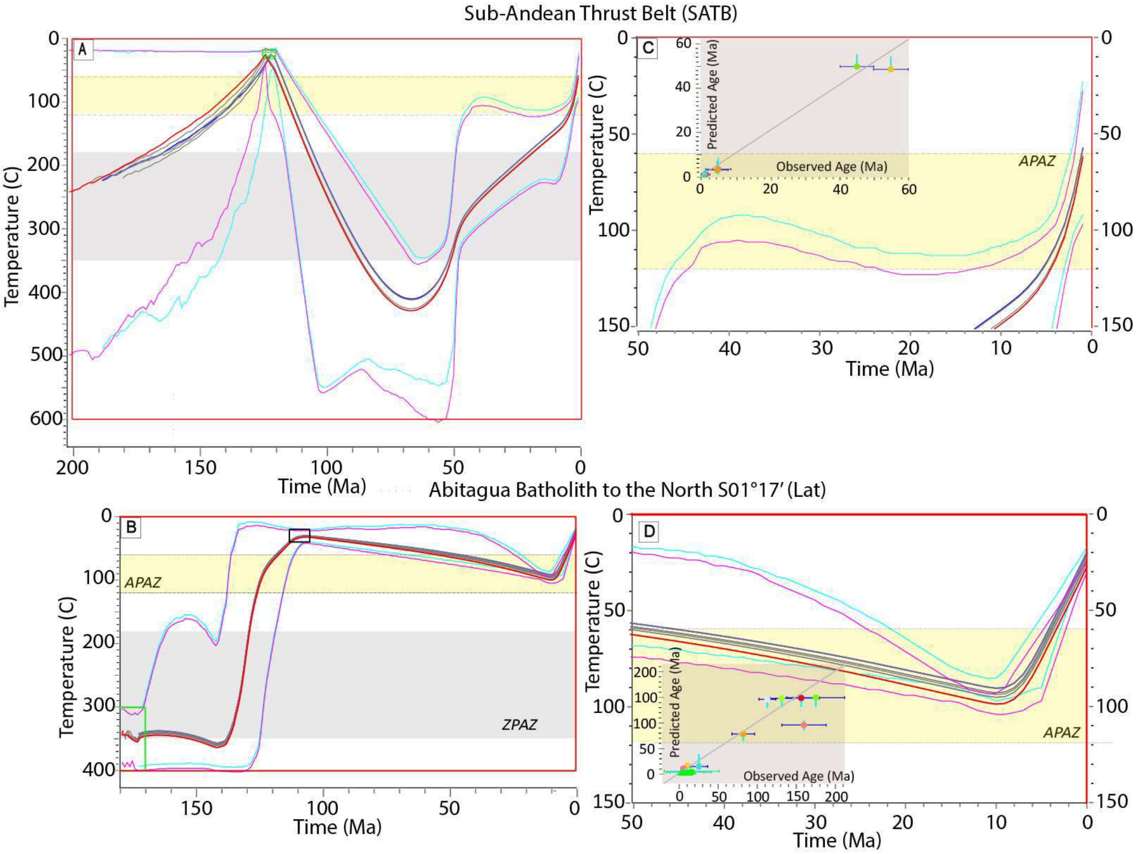

Fig. 16. Multi-sample time-temperature (t-T) paths for **(A)** the Sub-Andean Thrust Belt, showing an acceleration of cooling at ~6 Ma **(B)** the Abitagua Batholith. Each line depicts the t-T pathway of an individual sample, with dark red and blue lines representing the best model for the lower

and upper samples, respectively, and the light colors envelop the 95% credible interval. An inset plot of observed vs predicted ages based on the thermal history is displayed for each model. **C** and **D** show a closer view of the last 50 My for each model.

In the Abitagua Batholith north of 1°17’ S Lat, we used new and published information from Jurassic granitoids samples of the Abitagua batholith, whose crystallization age has been dated as 170.0 ± 0.7 Ma by U-Pb in zircon (Vallejo et al. 2021). A non-conformable contact with the overlying lower Cretaceous Hollín Fm document residence at near-surface temperatures at 109.0 ± 4.0 Ma, which we used as a stratigraphic constraint. We utilized a concordant AFT age of 27.2 ± 8.2 Ma and 5 single grain AHe ages ranging from 4.7 ± 0.5 to 17.5 ± 1.7 Ma from Jurassic magmatic sample 22NP25 (this study), in combination with published data from Jurassic magmatic samples including 4 AFT ages ranging between 5.0 ± 1.8 and 161.0 ± 15.0 Ma, and 4 ZFT ages ranging from 113.0 ± 12.0 to 176.0 ± 38.0 Ma. (Fig. 16B, Appendix B).

The thermal model from the Abitagua batholith (Fig. 16B) illustrates that following Jurassic-early Cretaceous rock exhumation, Cretaceous-Cenozoic heating associated with burial proceeded until Late Miocene to a peak temperature of approximately 98°C. A one-stage cooling phase started no later than 8 Ma, resulting in a moderate cooling rate between 8.0 and 10.5°C/My until present. The Late Miocene present phase of rock exhumation of ~2.1-2.8 km occurred at a rate of ~0.25-0.35 mm/y.

Farther to the east, in the core of the NU, cooling patterns were characterized using three multi-sample models, one for each transect. The northern and central transects predominantly include samples from the Upper Jurassic volcanic and volcaniclastic Misahuallí Fm, which near our study area has been dated as 172.3 ± 2.1 Ma (amphibole Ar/Ar in andesite, Romeuf et al., 1995) and 162 ± 2 Ma (Ar/Ar total fusion age in a rhyolite, Spikings et al., 2001). Vallejo et al (2021) present a U–Pb age of 148.34 ± 1.65 Ma in a high-level intrusion of the Misahuallí Fm. at ~3 S Lat, ~250 km farther to the south of our southern transect. Despite the lack of proximity, we used this age as an upper limit for the extrusion age of the Misahuallí Fm for thermal modeling (i.e., 175-145 Ma residence at surface temperature).

In the northern transect, north to the Quijos Fault (QF), we used a new single-grain AHe age of 3.7 ± 0.4 Ma from the Misahualli Fm (22NP09), 2 new

AFT ages from Jurassic magmatic samples NA18 and 22NP04 (101.6 ± 7.6 and 23.4 ± 6.5 Ma respectively), and a new AFT age of 22.1 ± 6.3 Ma from a phyllonite rock developed within the Maastrichtian-Paleocene Tena Fm in the immediate footwall of the Cosanga fault (NL68). In addition, we integrated published data from 3 ZFT ages (132.0 ± 28.0 to 175.0 ± 38.0 Ma) and 3 AFT ages (116.0 ± 30.0 to 78.0 ± 14.0 Ma) from the Misahuallí Fm (samples 19(Jm), 10(Jm), 51(Jm)), and two new vitrinite reflectance data from Cretaceous shales and mudstones samples (22NP03 and 22NP10) with 0.52 and 0.51 % Ro.

Time-temperature paths revealed protracted heating due to Cretaceous-Cenozoic burial until temperatures of 90-100°C until ~10-12 Ma (Fig. 17A). Subsequent Late Miocene cooling proceeded at rates of ~5-9°C/My, accommodating ~2-3 km of exhumation with a rate of ~0.16 - 0.30 mm/y.

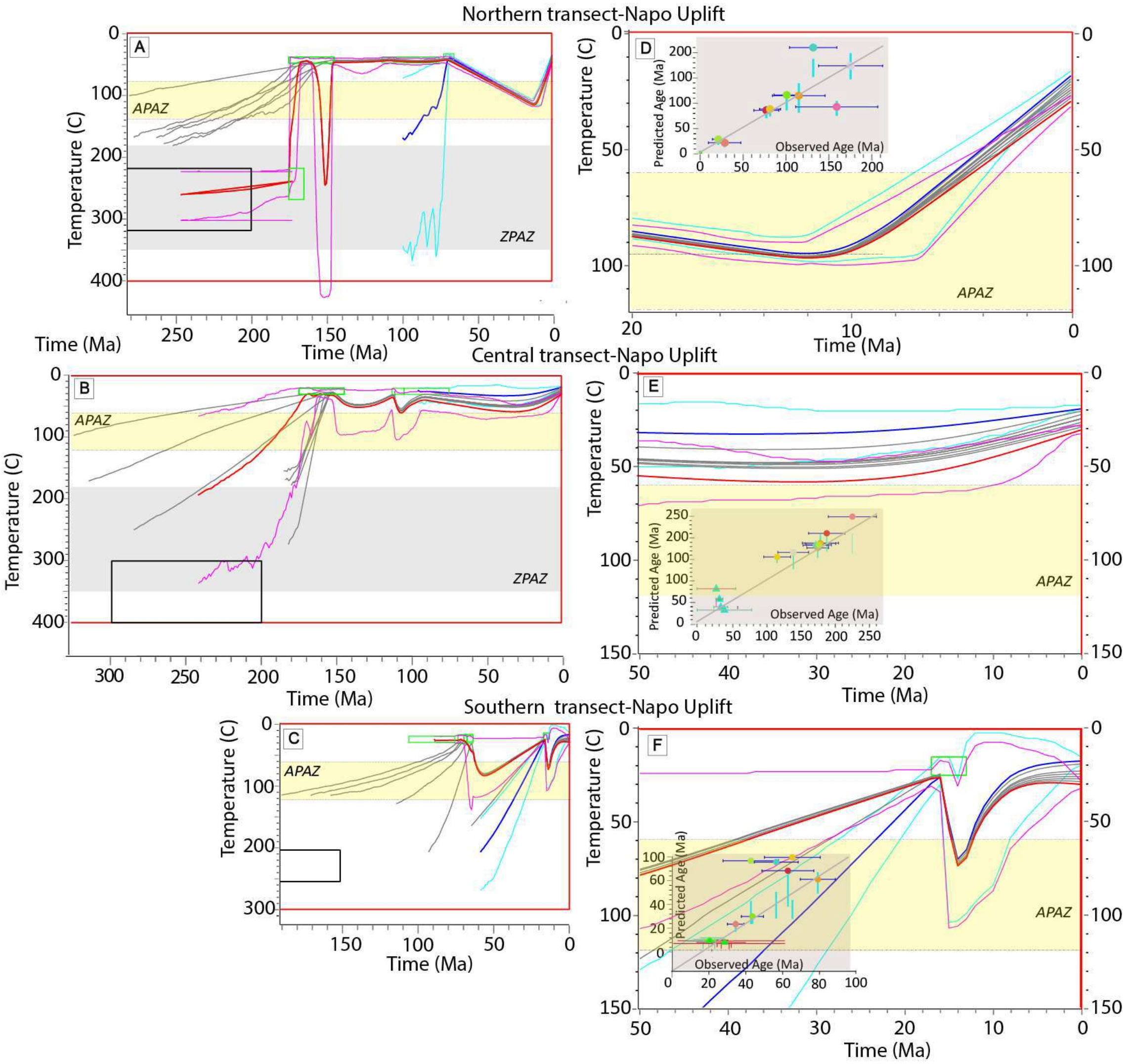

Fig. 17. Thermal-time (t-T) pathways for (A) the Northern, (B) Central, and (C) Southern transect in the NU. An inset plot of observed vs predicted ages based on the thermal history is displayed for each model. **D, E,** and **F** show a closer view of the last 50 My for each model. symbols and abbreviations are as in Figure 16.

In the Central transect across the NU, from Baeza to Loreto, we used thermochronometric data from Jurassic volcanic, magmatic, and volcanoclastic samples from the Misahualli Fm and two vitrinite reflectance data from the Hollín (22NP24) and Napo (22NP18) Formations of 0.51 and 0.48%, respectively. We integrated one new AFT age of 119.0 ± 16.4 Ma and 2 new single-grain AHe ages of 26.2 ± 2.6 and 18.5 ± 1.9 Ma from a Jurassic tophaceous sandstone (22NP19), one AFT age of 220.7 ± 39.2 Ma from Jurassic volcanoclastic sample (NL99), and 2 AFT ages of 110.0 ± 12.4 and 167.7 ± 9.0 Ma from Jurassic volcanic rocks (22NP21 and NL92). In addition, we integrated AFT and ZFT published data including one AFT age of 183.0 ± 30.0 Ma from Jurassic volcanoclastic sample (33(Jm)) and 4 ZFT ages ranging from 173.0 ± 30.0 to 156.0 ± 20.0 Ma from Jurassic volcanoclastic samples (31(Jm), 33(Jm), 84(Jm), and 29(Jm)) from the Misahualli Fm.

Thermal paths (Fig. 17B) reveal that peak temperatures associated with Cretaceous and Cenozoic heating reached only ~60°C, less than in the northern transect, and therefore the thermal history has a lower resolution. Cooling paths suggest that slow cooling (1.2-2.2°C/km) started at ~20 Ma at had proceeded until the present, implying exhumation of up to 1.5 km at slow rates of ~0.07 km/My. However, early Miocene subsidence occurred both, north and south of the structural culmination. We tentatively suggest that the thermal history places an old constraint on possible initial early Miocene uplift of the Napo Anticline, but more AHe data is needed to verify this hypothesis.

In the Southern transect of the NU, between Tena and Puerto Misahualli, we use only new AFT and AHe data from Cretaceous-Miocene sandstone samples from the Maastrichtian-Paleocene Tena Fm and Miocene Arajuno-Chambira Formations. We used 5 new AFT ages ranging from 80.0 ± 6.4 to 25.6 ± 3.0 Ma from Maastrichtian-Paleocene sandstones samples (20111MS, 20109MS, NJ69, 22NP29, and NJ82) from the Tena Fm, and 2 AFT ages (25.6 ± 3.0 and 33.4 ± 1.8 Ma) from the Arajuno and Chambira Formations. We also included 9 new single-grain AHe ages ranging from 28.8 ± 2.9 to 2.0 ± 0.2 Ma from Tena Fm samples 20111MS and 20109MS. Finally, we incorporated vitrinite reflectance data of ~0.55 % Ro from a Cretaceous shale sample (22NP27) from the Napo Fm. AFT ages and track lengths suggest that all but one (NJ82) samples from the upper Tena Fm. are partially reset.

Time-temperature paths allow Paleogene-Miocene (~55-16 Ma) cooling from maximum temperatures of around 85°C. However, basin subsidence associated with the accumulation of the Tiyuyacu and Chalcana Formations allows disregarding this t-T path. Post-Miocene heating to a maximum temperature of 70°C proceeded until ~12 Ma, when cooling at rates of 3.2-5.0 °C/km took place, implying exhumation of ~1.2-2 km at mean rates of ~0.1-0.16 mm/y. AHe data suggest that this late Miocene-recent cooling decelerated in the last 5 Ma.

5. DISCUSSION

5.1. Sediment provenance and unroofing sequence

The sedimentary history of the Oriente Basin began with the rift-related deposition of Jurassic units such as the Santiago, Chapiza, and Misahuallí Formations. Available heavy mineral analyses and detrital zircon U-Pb geochronology (Fig 18, Vallejo et al., 2021) show that the early Jurassic Santiago Formation is primarily characterized by mixed sources, influenced by both the craton and the magmatic arc.

In a Late Jurassic sandstone sample (22NP19) from the hanging wall of the Sub-Andean Front in the western NU show apatite U-Pb ages ranging from 349.4 to 267.0 Ma (Fig. 7G) corresponding with detrital zircon U-Pb population range from 366 to 250 Ma in a sample from the Early Jurassic Santiago Formation (Vallejo et al., 2021). This Zircon U-Pb population was associated with the metasedimentary Carboniferous–Permian Chiguinda unit from the Cordillera Real (Spikings et al., 2021). Carboniferous–Permian U-Pb age populations in both, zircon and apatite in the Jurassic Units suggest a western source. Although the petrogenetic nature of the apatites (22NP19) indicates a provenance exclusively from I-type granitoids and/or mafic igneous rocks (IM in Fig 8A), it is highly probable that they were transported to the Carboniferous–Permian Chiguinda Unit during the Pre-Andean Carboniferous arc magmatism, which was prevalent in Peru near the Ecuadorian border (Spikings et al., 2021; Vallejo et al., 2021). Given that a Late Carboniferous–Permian U-Pb age population of apatite or zircon has not been previously reported in the Late Jurassic Chapiza or Misahuallí Formation, the presence of the predominant Carboniferous–Permian apatite U-Pb population in the Jurassic sample 22NP19 (Figs. 9A and 7G) likely indicates that (1) there is a member from the Late Jurassic Chapiza Formation that may be correlatable or temporally equivalent to the Early Jurassic Santiago Formation; (2) there is a possibility that the 22NP09 sample corresponds to the Early Santiago Formation. However, this would imply the presence of the Early Jurassic Santiago Formation in the hanging wall of the Sub-Andean Front system in the western NU, contradicting previous studies that restricted the Early Jurassic Santiago

Formation outcrops to the Cutucú Uplift (Gaibor et al., 2008; Christophoul 1999; Díaz et al., 2003). If the above presumption holds true, the Early Jurassic Santiago Formation would be exposed at approximately S0° 50' 54" with a dip direction of 305° and a dip of 69°, possibly through a structure with geometry resembling a flower structure but with significant offset only on its eastern side of the wrench Sub-Andean Front system, possibly resulting from inverted Jurassic half-grabens beneath the SAZ (Baby et al., 1997; 1999).

In the Late Jurassic Upper Misahuallí Formation, andesite samples 22NP21 and 22NP04 (Figs. 7E and F), show a clear apatite petrogenetic fingerprinting in I-type granitoids and/or mafic igneous rocks (IM, Fig. 8A) an apatite U-Pb ages ranging from 118.0 to 207.4 Ma (22NP04), and from 141.6 to 283.4 Ma (22NP21). Despite sample 22NP21 has a smaller apatite U-Pb population with two older grains possibly originating from the Late Carboniferous-Permian Chiguinda unit, and sample 22NP04 shows just one grain younger than 140 Ma. The dominant apatite U-Pb population in both samples is almost equal between 144.0 and 207.4 Ma corresponding to the predominant detrital zircon U-Pb populations range from approximately 141.6 to 207.0 Ma from Late Jurassic Upper Misahuallí Formation (Fig. 18, Vallejo et al., 2021). U-Pb age populations in both, zircon and apatite along with the clear apatite petrogenetic fingerprinting from magmatic sources (IM, Fig. 8A) confirm the predominant and robust influence of volcanic input and granitic source rocks stemming from the erosion of the Jurassic volcanic arc, including the Abitagua, Zamora, and Rosa Florida batholiths.

Provenance studies conducted in the Cretaceous-Cenozoic sedimentary succession of the NU area have documented the initiation of uplift and exhumation in the Cordillera Real during the Late Cretaceous (76-73 Ma, Vallejo et al. 2021). This is based on the provenance polarity reversal documented by (1) a change from a cosmopolitan detrital zircon UPb distribution of dominantly Proterozoic (600-2100 Ma) zircons in the basal Maastrichtian-Paleocene Tena Formation to a unimodal distribution of Andean magmatic arc zircons in the upper Tena Formation. (Gutiérrez et al., 2019, Vallejo et al., 2021); and (2) the abrupt increase in volcanic heavy mineral assemblages (Fig 18). The youngest apatite U-Pb ages of ~65-70 Ma found in our samples of the uppermost Tena Fm and the unimodal distribution of late

Cretaceous (<100 Ma) AUPb ages (Fig. 7B) are in agreement with provenance from the Western Cordillera arc. Moreover, apatite petrogenetic fingerprinting in sandstones of the Tena Formation shows a shift from mixed sources, including low-grade and high-grade metamorphic (HM, LM) yet dominantly supplying I-type and mafic (IM) apatites, in the lower Tena Fm. to a fully IM composition in the uppermost Tena Fm. (Fig 8C), further documenting the reverse of provenance polarity. This major drainage reorganization has been ascribed to the uplift of the Western and Real Cordilleras in response to the initial accretion of oceanic terranes of the CLIP along northwestern South America (Gutiérrez et al., Horton 2018). Our thermal modeling from the SATB (Fig 16A) shows an onset of cooling of metavolcanic Jurassic rocks from a temperature of ~300°C at 70-60 Ma, in full agreement with the exhumation of a western Andean source during the latest Cretaceous.

In the Eocene Tiyuyacu Formation, a significant change is observed whereby apatite provenance shows the re-appearance of mixed sources, with the main contribution of high (HM) grade metamorphic apatites and minor low-grade metamorphic (LM) and S-type granitoids (Fig 8D). Such a change was accompanied by reappearance of a cosmopolitan detrital zircon U-Pb distribution with dominant peaks of Triassic (250 Ma), Neoproterozoic (500-600 Ma) and Grenvillean-Putumayo (1000 Ma) zircons and a marked increase of metamorphic and “cratonic” heavy mineral assemblages at expenses of the virtual disappearance of volcanic assemblages (Fig. 18). We attribute these changes to a combination of unroofing leading to the exhumation of deeper levels between 43.0 and 30 Ma (Spikings et al., 2000) in the Cordillera Real and the SATB. Consequently, as suggested by Gutiérrez et al (2019) to recycling and cannibalization of the proximal foreland (wedge-top), indicating the advancement of the orogenic wedge. This reworking is evident in the appearance of clasts from the Hollín Formation within the Tiyuyacu, as reported by Gutiérrez et al. (2019). Furthermore, these changes are directly linked to the significant sedimentation in the Tiyuyacu Formation, characterized by coarse-grained conglomerates, likely associated with a mega-fan system. Our thermal model of the SATB shows moderate cooling rates in the Eocene-Late Miocene, in agreement with protracted erosion leading to unroofing.

Our apatite trace element analysis in the Oligocene Chalcana Fm., despite the limited number of grains analyzed, reveals a dominant presence of apatites derived from low-grade metamorphic rocks (Fig. 8D) and with U-Pb ages of 200-500 Ma, indicating an increase in the contribution of metasedimentary Andean basement sources. Such a pattern implies the incorporation of deeper crustal levels and document unroofing of more distal areas, such as the western parts of the Cordillera Real. This interpretation aligns with the presence of minerals as garnets, epidote and chloritoid from medium-grade metamorphic suits and augite, hypersthene, olivine, chromite and (green and brown) hornblendes, suggesting a partial source in mafic rocks in the Western Cordillera (Ruiz et al., 2007). Further evidence of deeper unroofing is the reappearance of a Late Cretaceous magmatic arc (90–68 Ma) and the initial appearance of a syndepositional and Cenozoic age population (25–65 Ma) in the detrital zircons (Fig 18). During the Oligocene, sediment deposition rates were higher in the Oriente and other North Andean basins compared to the lower rates reported for the Tiyuyacu Formation (Parra et al., 2010., Horton 2018 and references therein), which has been attributed to orogenic advance.

In the early-middle Miocene rocks of the Arajuno and Chambira Formations, apatite petrogenetic fingerprinting reveals a subtle shift between the lower Miocene Arajuno (sample NA75 in Figure 8D) and the upper Miocene Arajuno (sample NA25 from the Miocene Chambira Formation, coeval with the upper Miocene Arajuno). In the lower Miocene Arajuno, apatites are primarily derived from high-grade metamorphic rocks, with some apatites from igneous rocks. In contrast, in the upper Miocene Arajuno, the majority of apatites are derived from low-grade metamorphic rocks, and there is no presence of apatites derived from igneous sources (Fig. 8D). This shift suggests a disappearance in the sources of the Andean magmatic arc. However, it's important to note that Miocene Arajuno may still exhibit these Andean signals, likely indicating recycling through the erosion of the Eocene-Oligocene substratum.

Detrital zircon U-Pb age distributions show a change from cosmopolitan Cratonic-Andean mixed to unimodal Andean sources from the base to the top of the Arajuno Fm. at ~15 Ma. Dominant zircon U-Pb populations in the Lower Arajuno include Late Cretaceous (<100 Ma) zircons whereas in the upper Arajuno they are mostly Triassic with very little Proterozoic grains, and minor syndepositional Miocene zircons (Fig. 18) coinciding with the petrogenetic fingerprint. All these observations suggest a source in the SATB, west of the Abitagua batholith. The lack of both a Jurassic zircon U-Pb populations (Fig. 18) and IM apatites suggests a source in metamorphic terranes of the Cordillera Real and predates the activation of the Cosanga fault, which based on our thermal modeling (Fig 16B), occurred at ~8 Ma, exhuming the Abitagua batholith from within the AFT PAZ. Such erosion in the SATB and western Cordilleras has been well documented by Spikings et al., (2010), who identified a significant exhumation event starting around 15 Ma and resulting in an estimated ~3.5 km of exhumation in the Northern Cordillera Real. Additionally, the western part of the SATB experienced rapid exhumation during this period (Ruiz, 2002). Our thermal modeling suggests that both, the SATB fault and the Cosanga faults were active in the since Late Miocene-Pliocene (6-7 Ma), but that exhumation rates were twice as much higher in the former (up to 0.7 mm/yr vs up to 0.35 mm/yr). Rapid exhumation is in agreement with rapid sediment accumulation in the Oriente basin throughout the Miocene (Horton 2018 and references therein).

In the Pliocene to Quaternary Mesa and Mera Formations, the heavy mineral assemblages clearly indicate a significant volcanic and magmatic influence (Fig 18, Ruiz et al., 2007). This coincides with the zircon UPb data, which reveals (1) Triassic signatures, likely sourced from the Triassic Tres Lagunas formations of the Cordillera Real; (2) Jurassic signatures from magmatic arc (Fig. 18; Gutierrez et al., 2019), which include the heightened erosion of the Abitagua batholith and the reworking of the Misahuallí Formations; and a smaller peak in zircon UPb ages from the Early Cretaceous, likely associated with mafic igneous rocks of the Peltetec unit (Fig. 18). This combined evidence strongly suggests substantial exhumation of the eastern part of the Cordillera Real and implies significant uplift and exhumation of proximal areas, due to, the thrust propagation involving the NU led to significant exhumation between ~1.2 and ~3.0 km, as indicated by our thermal models in the southern and northern transects (Figs. 17A, C and 19). The deposition of the Mera and Mesa Formations to the east of the NU may be associated with erosional exhumation of a growing topography of the whole Northern SAZ.

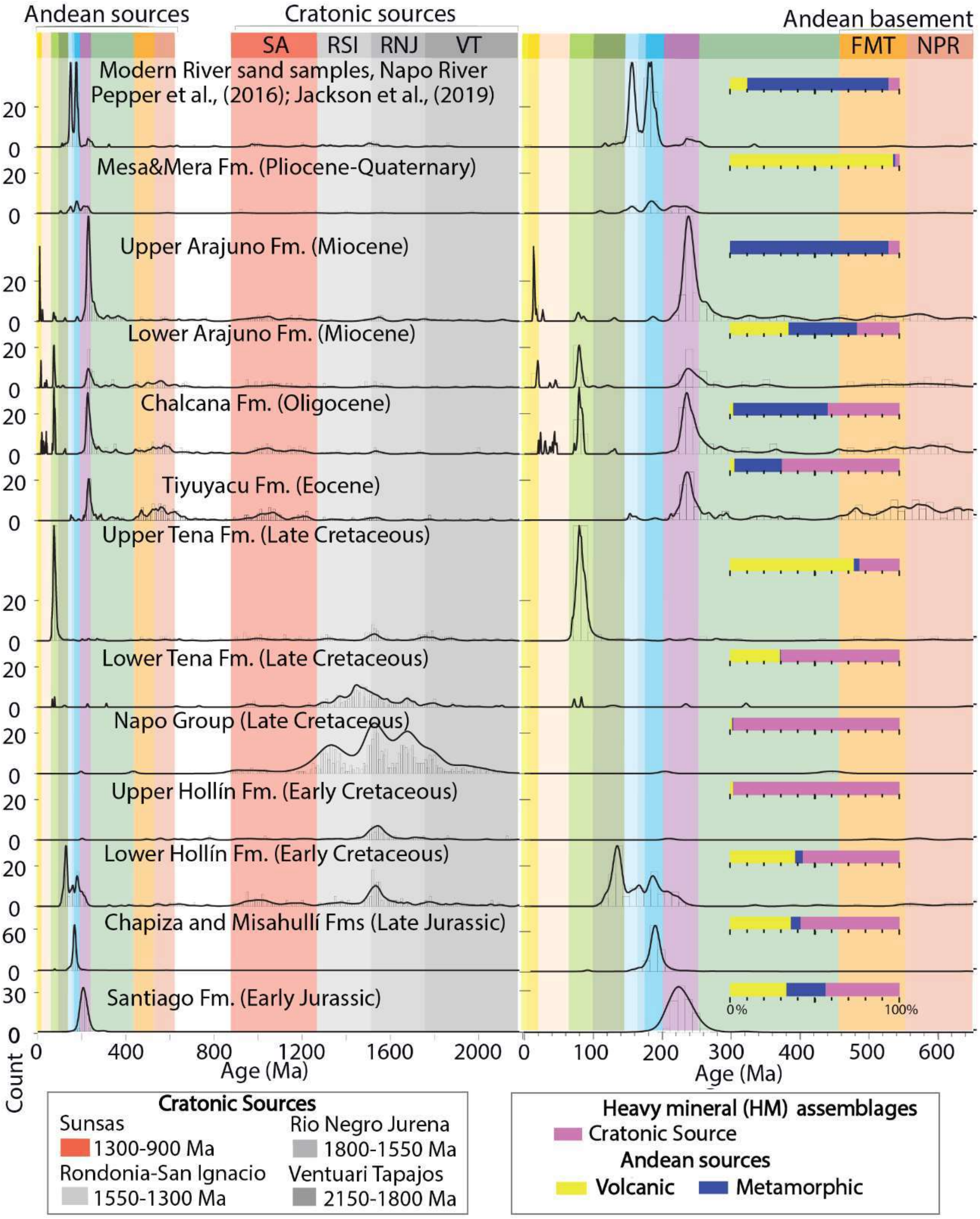

Fig 18. The composite probability density plot compiles detrital zircon U-Pb geochronological data from Jurassic–Cenozoic strata (Gutiérrez et al., 2019; Vallejo et al., 2017; 2021) and modern river sands from the Napo River (Pepper et al., 2016; Jackson et al., 2019). It illustrates diagnostic age populations representing detrital contributions from four main tectonic provinces: 1) Western Cordillera magmatic arc (<100 Ma); 2) Eastern Cordillera metasedimentary basement (650–250 Ma), Triassic intrusions (250–200 Ma), and limited Cretaceous igneous rocks (145–66 Ma); 3) Subandean Zone basin fill (recycled cratonic signatures from Cretaceous strata); 4) Crystalline basement of the South American craton (>900 Ma). Inset plots of heavy mineral (HM) assemblages show the percentage of source association: Cratonic source (zircon, tourmaline, rutile, monazite, branti), Volcanic Andean source (apatite, cassiterite, olivine augite, hypersthene, hornblende), and Metamorphic Andean source (Pumpellyite, Epidote, Sillimanite, Granite, Clinozoisite, Chloritoid, Zoisite). Data compiled from Ruiz et al. (2007) and Vallejo et al. (2021).

5.2. New Low-temperature thermochronological data (AFT and AHe) and Inverse QTQt thermal history models

The new AHe analyses (Table 4) show high intrasample dispersion but do not show any correlation between the effective Uranium content (eU) and the AHe age (Fig. 12). Therefore, it was not possible to use weighted mean ages in the modeling. Instead, we used single-grain AHe ages for modeling, excluding outliers (Appendix E). single-grain AHe ages between 3.7 ± 0.4 and 17.5 ± 1.7 Ma were found in the western central transect (22NP21), the Abitagua Batholith (22NP25), and the Northern transect (22NP09), comparable with the range of AHe ages obtained from the northern Cordillera Real (north of 1°30'S; 10.4 ± 0.9 Ma - 2.06 ± 0.01 Ma; Spikings and Crowhurst, 2004). In the eastern central transect (22NP19) and southern transect (20111MS and 20109MS), AHe single-grain ages ranging between 28.8 ± 2.9 and 2.0 ± 0.2 Ma showed high dispersion, likely associated with being partially reset ages in sandstone samples.

In general, the new AFT ages from the Jurassic magmatic samples from the Misahualli Formation in this study (Table 3) have values similar to ages published by Ruiz (2002), with some clear exceptions as the youngest AFT age of 23.4 ± 6.5 Ma from andesite sample (22NP04). Probably this sample underwent more burial than the near sample NA18, according to a lower mean chlorine content (0.3 Wt%) in the younger sample than the sample NA18 with double mean chlorine content.

In the Northern transect, the new AFT ages from Jurassic samples have similar ages to published ages of nearby samples, such as the new age of 101.6 ± 7.6 Ma from the Jurassic magmatic sample (NA18) and the AFT published ages between 78 ± 14 and 101.6 ± 7.6 Ma from Jurassic samples (53(Jm), 19 (Jm), and 10 (Jm), Fig. 9A). These ages, slightly younger than their late Jurassic stratigraphic age, indicate a low annealing degree. Only a single-grain AHe age of 3.7 ± 0.4 Ma from the Jurassic magmatic sample (22NP09) was used in thermal modeling due to the low apatite fertility of the sample. In the northern transect, a relatively young AFT age of 22.1 ± 6.3 Ma thermally reset from the phyllites rock sample (NL68) from the Maastrichtian-Paleocene Tena Formation is also noteworthy. The sample was possibly affected by fluid circulation through the Cosanga fault system due to its proximity.

In the Central transect, only one new AFT age of 167.7 ± 9.0 Ma from the Jurassic magmatic samples (NL92) is similar to the published age (183.0 ± 30.0 Ma) for the same unit (29(Jm) in Appendix B; Ruiz, 2002). Noticeably, two samples of the same unit (22NP21 and 22NP19) yielded younger AFT ages of 110.0 ± 12.4 and 119.0 ± 16.4 Ma. While sample 22NP19 is from Jurassic volcanic breccias from the hanging wall of the Sub-Andean Front in the eastern NU, sample 22NP21 is from andesite rocks from the footwall of the Abitagua Fault in the western NU. However, despite the shorter MTL observed in sample 22NP21 compared to 22NP19 on the western side, suggesting greater burial on the eastern side, only 6 TL support this comparison. Conversely, the eastern sample (22NP19) exhibits a shorter Dpar of 2.3 µm compared to the western sample (22NP21) with 2.7 µm, suggesting more robustly the opposite, that the western side underwent more burial. These young samples may be younger than the other Jurassic samples in this transect due to a higher mean Uranium content (7 and 7.5 ppm) in comparison with the samples NL92 and NL99 with 4.0 and 2.6 ppm of mean uranium content, respectively.

In contrast to the thermochronological analysis performed in the NU by Ruiz (2002), our investigation has uncovered AFT ages in the Maastrichtian-Paleocene Tena Formation samples ranging from 39.0 ± 12.3 to 80.0 ± 6.4 Ma that were only partially reset with maximum paleotemperatures of 100-120°C in the Southern Transects in the NU. This confirms that the southern transect of the NU underwent more burial than the central transect in the NU.

The new AFT ages (Table 3) between 22.1 ± 6.3 and 220.7 ± 39.2 Ma in the NU are relatively old in contrast to the younger AFT ages from 2.5 ± 1.0 to 6.4 ± 1.8 Ma in the SATB, which underwent total annealing for AFT and ZFT system. The young AFT ages in the NU are consistent with what was expected due to the limited post-depositional heating associated with burial (Ruiz, 2002).

5.2.1. Spatial trends in cooling histories

The thermal histories of the transects in the NU (Fig. 17) reveal that peak temperatures never exceeded 100°C since the Early Cretaceous, which suggest that NU experienced minimal burial (<4 km, Fig. 17) In the central transect, despite incorporating single-grain AHe ages from single grains both in the west and east, lacks resolution due to its entire post-depositional history being below 60°C (see Fig. 17B). However, the variation in peak temperatures along the strike of the NU reveals that in the Northern and Southern transects of the NU, peak temperatures reached close to 100°C, associated with deeper burial than the Central transect (<2.5 km). Rivadeneira and Baby, (2004) document a Late Cretaceous inversion event in the Oriente Basin setting the broad anticlinal structure in the NU, based on a thickness reduction in the post-Turonian stratigraphic section studied with surface and subsurface data across the NU. However, any uplift associated with this event must have occurred at very slow rates and involved minimal rock uplift. Consequently, determining the age for the major uplift of the broad anticlinal fold in the NU is challenging, as it was not recorded by the AFT and AHe systems. However, in transpressive deformation structures like the Bermejo anticline to the north of NU, a relationship has been established with the development of its structure prior to the Paleocene, most likely during the Maastrichtian, due to observed *onlaps* of the lower Tena Formation over the Napo Formation, suggesting the occurrence of a possible progressive unconformity event (Baby et al., 1997).

This evidence suggests the presence of a paleo-uplift in the NU since the Maastrichtian, where the persistent elevation of this area in the current central transect compared to the rest of the eastern terrains since the Late Cretaceous allowed this prominent relief, present since the Late Cretaceous inversion, to gradually accumulate a significant volume of hydrocarbons in the western part of the anticlinal structure of the NU, specifically in the reservoir of the Hollín Formation, representing the Pungarayacu field (Fig. 2 for location, Rivadeneira and Baby, 2004). This Maastrichtian paleo-uplift could explain why the central transect did not experience temperatures exceeding 60°C, as it is a pre-Paleocene structure that never underwent significant burial, while in the northern and southern transects, peak temperatures reached close to 100°C. The Late Cretaceous peak temperature difference Between the Southern and the Central transects (Figs 17B and C) allows us to establish an elevation difference in the antiformal culmination (central transect) of the paleo-uplift greater than 1.0 km compared to the southern transect. This difference has been observed in seismic profiles (N-S) along the Pungarayacu Field, with the Hollín Formation exposed in the central transect (see 22NP24 sample in Figure 9A for location; Rivadeneira and Baby, 2004)

Cooling started in the SATB in the Paleogene, at around 50 Ma, and continued at moderate rates until its acceleration at around 7 Ma. This initial cooling phase with a rate of ~0.13 mm/y was as slow as the Late Miocene exhumation phase in the Southern transect in the NU (from 0.10 to 0.16 mm/y; Figs. 16A, 17C). The similarity in exhumation rates (~0.13 mm/y) between ~13 and 7 Ma in the Southern transect and the SATB suggest that the SATB likely served as a buttressing mechanism for the propagation of deformation across the entire Northern SAZ, reactivating inherited fault zones during the middle Miocene, as suggested by Ruiz (2002).

All the provinces in the Northern SAZ display a one-stage cooling phase since the middle to Late Miocene, with the exceptions of the SATB, which had a two-stage cooling (Fig 16A), and the Central transect where thermal histories lack resolution. The sequence of the onset of these rapid cooling phases after 15 Ma related to exhumation and uplift begins first in the SATB, which appears to have been growing up or accommodating deformation at least since the Eocene. Then, the provinces in the NU start their exhumation in a nearly continuous sequence, in the Southern transect around ~13 Ma accommodating between 1.2 and 2.0 km, followed by the Northern transect between 12 and 10 Ma, almost contemporaneously with the Abitagua batholith between 10 and 8 Ma. The Northern transect and the Abitagua Batholith share approximately similar exhumation rates (Fig. 19) and accommodate similar maximum exhumation (~2.9 km). Finally, in the Subandean Thrust Belt (SATB) between ~7 and 6 Ma, started its youngest and highest exhumation rate in the region ranging from 0.43 to 0.67 mm/y accommodating between ~3 and 4 km.

The following describes the two main exhumation phases in the Northern Subandean Zone, associated with previously documented deformation styles (Pasquarè et al., 1990; Balseca et al., 1993; Baby et al., 1997; 1999; 2013; Rivadeneira and Baby, 2004) and tectonics models (Alvarado et al., 2016).

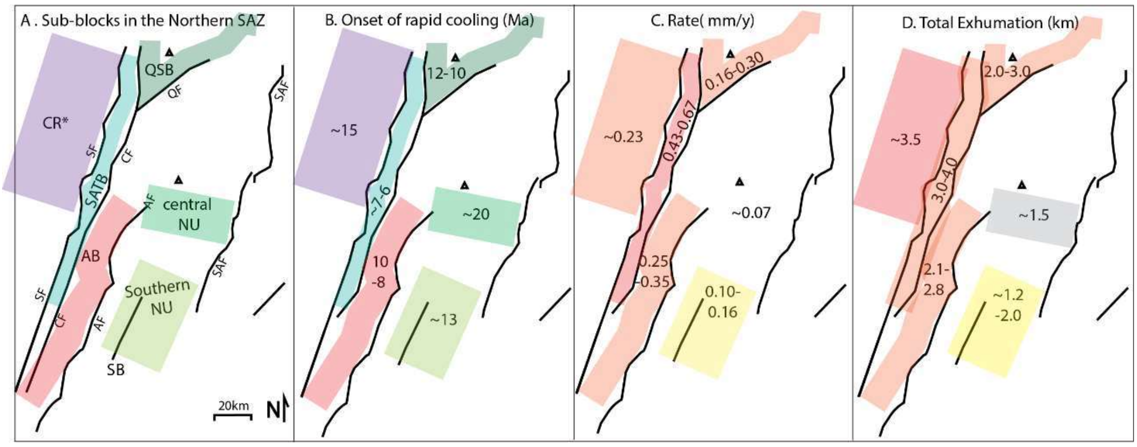

Fig 19. Simplified schematic of litho-tectonic provinces with cooling events starting in (B) after the Middle Miocene. The rate (C) and magnitude (D) of each exhumation phase were calculated using a thermal gradient of 30°C/km. Conventions: Cordillera Real (CR), Sub-Andean Thrust Belt (SATB), Abitagua Fault (AF), Abitagua Fault (AB), Cosanga Fault (CF), Quijos Fault (QF), Subandean Fault (SF), Sub-Andean Front (SAF), South-Block (SB).

5.2.1.1. Middle Miocene to recent exhumation phase in the Napo Uplift

Although the difference in the initiation of the exhumation phases of the different blocks is small (<3 My), this difference is within the error of the thermochronological modeling and is not significant. Therefore, we discern two major phases of exhumation in the Northern SAZ. The first event of almost synchronous exhumation in the NU commenced between 13 and 10 Ma, as evidenced in both the Northern and Southern transects (Figs 19, 17A, and 17C), with strike-along variation in exhumation rates and magnitude. The Northern transect exhibits comparatively high exhumation rates with a maximum rate of ~0.3 mm/a, while lower rates are evident in the Central with ~0.07mm/y and Southern transects between ~0.10 – 0.16 mm/y (Figs 17B and C). Notably, the intensity of deformation in the Central and Southern transect regions with a general sub-horizontal attitude is relatively modest in comparison to the Northern transect with reverse fault segments as the Quijos Fault and compressive structures as dipping duplex between the Cosanga Fault and the Quijos Fault (Pasquarè et al. 1990). However, in the Central transect, seismic profiles across the Sub-Andean Front at S0°30' show a vertical uplift of the Subandean Front exceeding 1000 meters (Baby et al., 1997), similar to the calculated exhumation in the central transect (~1500 m, Fig. 19).

Our thermal models in the Northern transect and within the Abitagua Batholith support the significant development of oblique-slip fault systems occurred along the Cosanga-Chingual segment of the Chingual-Cosanga-Pallatanga-Puná fault system (CCPP; Fig. 1; Alvarado et al., 2016) since the Late Miocene. On one hand, the oblique deformation in the hanging wall of the Cosanga Fault could be transferred to the hanging wall of the Quijos Fault (a segment of the Cosanga Fault) through oblique thrust-type deformation mechanisms associated with strike-slip motions, as suggested by Pasquarè et al. (1990). The hanging wall of the Quijos Fault served as the primary source for samples used in the thermal modeling of the northern transect (Fig. 9A), where its thermal history reveals an exhumation phase almost concomitant (from 10 to 8 Ma) with the exhumation phase in the Abitagua batholith. Exhumation started first (12-10 Ma) in the northern footwall of the Cosanga Fault, activating the Quijos Fault and then in the southern footwall (10-8 Ma) of the Cosanga Fault, activating the Abitagua Fault. Furthermore, the exhumation event in the northern transect (Quijos sub-block) event aligns with the compressive deformation evidenced in the dipping duplex in the vicinity of the Reventador volcano, as proposed by Pasquarè et al. (1990). On the other hand, the Abitagua Batholith does not exhibit internal deformation, implying that it experienced an "escape" movement in its emplacement to its ultimate level since the Late Miocene (~10-8 Ma), contributing to the formation of the highest non-volcanic topography in the Northern SAZ (Pratt et al., 2005).

During this phase, the principal stress direction (sigma1) was oriented WNW-ESE, perpendicular to the Sub-Andean Front system-oriented NNE-SSW (Pasquarè et al., 1990). This stress orientation aligned with the compression direction perpendicular to the average NNE-SSW orientation of numerous folds within the Mesozoic formations according to Pasquarè et al., (1990).

5.2.1.2. Late Miocene to recent exhumation phase in the Sub-Andean Thrust Belt (SATB) and out-of-sequence thrusting.

The second exhumation phase in the Northern SAZ is documented in the Subandean Thrust Belt (SATB), starting between 8 and 6 Ma until the present (Fig. 16A). This exhumation phase coincides with (1) a second phase of higher exhumation rate (~0.5 km/My) commencing around 6-5 Ma in the Western Cordillera (Margirier et al., 2022); (2) the Late Miocene onset of exhumation with active shortening, rock uplift, and coeval exhumation in the Coastal Cordillera (Brichau et al., 2021) and the northern Cordillera Real, where ~2.3 km of exhumation has occurred since 5.5-3.5 Ma (Spikings & Crowhurst, 2004; Spikings et al., 2010). These pulses across Ecuador were possibly activated due to the increased coupling at the plate interface after the subduction of the Carnegie Ridge, which may have caused the acceleration of the northward motion of the NAS through the CCPP triggering transpressive dextral deformation in its segments (Cosanga Fault) (Deniaud, 1999; Witt et al., 2006; Spikings et al., 2010, Margirier et al., 2022). These movement activated a phase of oblique deformation was marked in the SATB by the reactivation of reverse faults from the preceding pure thrust phase but with an oblique component. The principal stress direction (sigma1) shifted anticlockwise from NNE-ESE to E-W (Pasquarè et al., 1990). The deformation is well limited to the SATB by the Cosanga Fault to the west. The Cosanga fault, situated near the ancient Cosanga Fault tectonic system that was active during the Jurassic as a syn-depositional Fault, representing the cratonic front (Pratt et al., 2005), delineates the boundary between metamorphic rocks and deformed Mesozoic units in the SATB and non-deformed domains in the NU, as in the Northern transect (Aspden and Litherland, 1992).

Taking into account that deformation occurred first in the SATB since the Eocene (Fig. 16A), then propagated eastward to the NU in the middle-Late Miocene exhumation phase, and later, in the Late Miocene exhumation phase to the present, returned and accelerated the exhumation and deformation in the SATB. This suggests out-of-sequence thrusting slip along the Ecuadorian orogenic wedge, most likely favored by the inherited structural grain. Out-of-sequence thrusting has the potential to impact the overall configuration of a duplex or imbrication zone (Fossen, 2010, Pasquarè et al., 1990) as seen in the SATB. It could involve a potential Bulldozer effect, shifting the deformation from being accommodated in the east (Southern transect) to the west (SATB).

In summary, our thermal models unveil a chronological sequence of events in the NU, particularly focusing on the Neogene period. Initially, the SATB was activated in the Eocene, accompanied by a rapid exhumation pulse in the Cordillera Real. The exhumation in the Cordillera Real caused a major erosive planed surface between the Lower Tityuyacu and Upper Tiyuyacu Formation (Christophoul et al., 2002), indicating an eastward propagation pulse (Baby et al., 2013). Subsequently, the Sub-Andean Front system was activated in the middle Late Miocene. The subsequent activation of the Abitagua Batholith (10-8 Ma) concluded with heightened SATB deformation commencing between 8 and 6 Ma. These findings suggest that the migration of deformation is primarily driven by the dextral transcurrent reactivation of favorably oriented deep fault systems, including primarily the transpressive Subandean Front System and the Cosanga Fault. Additionally, it may be influenced by changes in the stress field direction since the Middle Miocene (~13 Ma) and in the Late Miocene (~7 Ma) (Alvarado et al., 2016; Pasquarè et al., 1990; Balseca et al., 1993).

Furthermore, the occurrence of out-of-sequence thrusting along pre-existing thrusts, observed since the Middle Miocene and continuing to the present, indicates a complex deformation pattern in the thrust-belt advance associated with thick-skinned tectonics. This pattern can be explained by several factors:

The narrowing restraining bends documented in the SATB prove the partitioning of dip-slip and strike-slip components (Alvarado et al., 2016; Pasquarè et al., 1990). The impact of erosion on the wedge since the Eocene, resulted in the redistribution of sediments through the cannibalization of the Hollín and Napo Formations within the Eocene Tityuyacu Formation. Wedge erosion may modify the internal stress state, allowing for the frontal advancement of the thrust belt.

The presence and continuous erosion of a critical wedge in the Miocene, contemporaneous with a new rapid exhumation of the Cordillera Real (Spikings et al., 2000), likely propagated deformation and exhumation of new structural zones within the Andean fold-thrust belt in the NU due to a 'bulldozer wedge' effect (Fossen, 2010) in the Sub-Andean Front, leading to out-of-sequence thrusting due to changes in the stress field direction (Pasquarè et al., 1990). This interaction is influenced by adjacent structures along the Late Miocene such as the Cordillera Real and the rigid block of the Abitagua Batholith (Pratt et al., 2005), and stress partitioning in the SATB. This transformation in the stress field dynamics appears to be closely linked to the increase in plate coupling at the subduction interface, which was driven by the onset of the Carnegie Ridge subduction (Yepes et al.,2016; Margirier et al., 2022).

5.2.2. Comparison of exhumation phases with previous studies.

The QTQt thermal history models based on new and previously published thermochronology data from Jurassic Units in the NU (Fig 17) reveal similar histories to the documented by Ruiz, (2002) in terms of the maximum heating of the blocks in the NU. In the Northern transect, our thermal modeling derived mostly from Jurassic magmatic rocks from the Misahuallí Formation show a Late Miocene exhumation started between 12 and 10 Ma. This is in contrast to the older exhumation phases (between 26 and 18 Ma) previously reported by Ruiz, (2002) from Jurassic magmatic samples from the same Misahualli Formation (Fig. 9A). Primarily, the inclusion of new AHe data in all models reveals recent cooling trends not present in the models from Ruiz (2002), which relied exclusively on AFT data.

Also in the Northern transect of the NU, our thermal model shows that was accommodated a maximum exhumation of ~3.0 km since at least 12 Ma comparable with ~3.5 km accommodated in the Northern Cordillera Real (N0°30') since 15 Ma documented by previous thermochronological studies using AFT and AHe data (Spikings et al., 2010, Spikings and Crowhurst, 2004).

In contrast, the thermal modeling of the Central and Southern transects has been accommodating in exhumation of at least ~1.5 km since 20 Ma and ~1.2 km since ~13 Ma, respectively. These exhumation rates documented south of S0°30' in the NU are comparable with the rapid exhumation of ~1.3 km previously reported between S0°30' and S1°30' in the Cordillera Real since 15 Ma (Spikings et al., 2010; Spikings and Crowhurst, 2004).

The thermal model for the Jurassic Abitagua batholith is very similar in the Late Miocene exhumation phases to the previous models reported by Ruiz (2002). Moreover, comparing the thermal history of the Jurassic Abitagua batholith with an exhumation phase starting between 10 and 8 Ma (Fig. 16B), it shows similar exhumation rates to a Jurassic batholith in southern Colombia referred to as the Sibundoy block by Pérez-Consuegra et al. (2021). While in the NU, the Abitagua batholith has exhumation rates ranging from 0.25 to 0.35

mm/y, while in southern Colombia, the Sibundoy block exhibits 0.4 mm/y. Moreover, the quantity of overburden removed from the Sibundoy Block in the last approximately 7 My was estimated to be around 2.7 km, which is comparable to the maximum exhumation accommodated, approximately 2.8 km, by the Abitagua Block since at least 8 Ma (Fig. 19) In addition, the exhumation in the Abitagua block is consistent with Late Miocene exhumation reported by thermochronology analysis using AFT and AHe in the Zamora Batholith, starting in its northern part (~S03°58') since ~9 Ma and in the southern (~S04° 05') at between 15 and 7 Ma (Spikings et al., 2010).

Our estimate of the starting of deformation in the NU between 13 and 7 Ma aligns with the onset of exhumation and/or deformation at 13 and 9–8 Ma in the Sub-Andean mountain ranges of northern Peru (e.g., Spacabapan et al., 2023; Mégard, 1984; Moreno et al., 2020; Sébrier et al., 1988). Especially, in the Biabo anticline in the Marañon Basin, when Calderon et al., (2017) by AFT thermochronology documented exhumation phases starting in the middle Eocene, and between 18 and 15 Ma associated with thin-skinned deformation, while in the Northern SAZ is associated with a thick-skinned deformation (Baby et al., 2013). However, our estimated onset exhumation contradicts previous studies that estimated a Pliocene-Quaternary age for the exhumation and uplift of the NU by the Subandean Frontal System (Baby et al., 1997). These studies were based on deformation in Cretaceous-Cenozoic strata observed in seismic profiles, and deformed Quaternary lahars reported from outcrops located in the NU. However, we do not rule out a more recent phase of deformation that was not entirely discerned by our thermal models, which could account for Quaternary deformations in the NU. This includes right-lateral transcurrent motions along NE to NNE trending faults dividing the NU into four main blocks (Balseca et al., 1993).

4. CONCLUSIONS

Our QTQt thermal models, based on existing thermochronology data and new AHe and AFT data, along with additional vitrinite reflectance data from the NU, provide a detailed, low-temperature thermal history previously overlooked by AFT analysis as discrete exhumation events since ~13 and ~7 Ma, in the NU and the SATB, respectively. The uplift of the Napo Uplift significantly influenced the sedimentation of recent Miocene units, starting around 13-10 Ma with variations in exhumation rates along the northern and southern transect. The influence of adjacent structures, such as the Abitagua Batholith, acting as a rigid block may explain the along-strike variation in exhumation rates in the NU

The exhumation pulse around 7 Ma in the Sub-Andean Thrust Belt (SATB) is associated with heightened plate coupling at the subduction interface induced by Carnegie Ridge subduction. This pulse provides unprecedented evidence of out-of-sequence thrusting in the Subandean ranges of the Northern Andes, attributed to the earlier activation of the Napo Uplift at ~ 13 Ma.

Combined with detrital apatite U-Pb ages and trace element geochemistry unraveled the provenance history of Cretaceous to Miocene strata in the NU, integrating also previous provenance proxies based on heavy minerals and detrital zircon U-Pb ages. Our results and available multi-method proxies allow documenting the spatial and temporal patterns of source area evolution as well as the unroofing patterns of the Cordillera Real. The existence and ongoing erosion of a critical wedge in the Paleocene-Eocene (~44 Ma) and the Miocene, coupled with the rapid exhumation of the Cordillera Real, likely propagated deformation and exhumation of new structural zones within the Andean fold-thrust belt in the Napo Uplift (NU). This, in the case of the Miocene, resulted in out-of-sequence thrusting during the Late Miocene.

The NU is an antiformal structure that took shape between the Late Cretaceous and the Paleocene, representing a paleo-uplift in comparison to the rest of the eastern terrains since the Late Cretaceous. The consistent elevation in the central transect prevented this central culmination in the NU from experiencing temperatures exceeding 60°C. In contrast, in the northern and southern transects, peak temperatures reached close to 100°C, which allow us unraveling new thermal histories with an enhanced spatiotemporal resolution. The NU was subsequently exhumed in the Miocene-Late Miocene exposing its Jurassic basement.

In general, the geological transformation of Ecuador has been shaped by the realignment of lithospheric plates and the consequential alterations in plate movement as the oblique subduction of buoyant bathymetric highs such as the aseismic Carnegie Ridge since ~7 Ma. These shifts have instigated various episodes of structural deformation and local variations in stress orientations.

REFERENCES

Aizprua, C., Witt, C., Johansen, S. E., & Barba, D., 2019, Cenozoic stages of forearc evolution following the accretion of a sliver from the Late Cretaceous-Caribbean large igneous province: SW Ecuador-NW Peru. Tectonics, 38(4), 1441-1465.

Almendral, A., Robles, W., Parra, M., Mora, A., Ketcham, R.A., and Raghib M., 2015, FetKin: Coupling kinematic restorations and temperature to predict thrusting, exhumation histories, and thermochronometric ages: AAPG Bull., (99, 8), pp. 1557-1573

Alvarado, A., Audin, L., Nocquet, J.M., Jaillard, E., Moths, P., Jarrin, P., et al., 2016, Partitioning of oblique convergence in the Northern Andes subduction zone: Migration history and the present-day boundary of the North Andean Sliver in Ecuador. Tectonics, 35(5), 1048-1065, doi.org/10.1002/(ISSN)1944-9194.

Angulo-Romero, E., Beate, B., & Romero-Cóndor, C., 2023, Zonificación del gradiente geotérmico en la cuenca Oriente de Ecuador a partir de temperatura de fondo de pozos: Boletín De Geología, 45(1), 119–139. https://doi.org/10.18273/revbol.v45n1-2023006

Aspden, J.A., Litherland, M., 1992, The geology and Mesozoic collisional history of the Cordillera Real, Ecuador. Tectonophysics, 205, 187-204.

Ault, A. K., Gautheron, C., King, G.E., 2019, Innovations in, U-Th)/He, fission track, and trapped charge thermochronometry with applications to earthquakes, weathering, surface-mantle connections, and the growth and decay of mountains. Tectonics, 38(11), 3705-3739, doi.org/10.1029/2018TC005312.

Axen, G.J., van Wijk, J.W. & Currie, C.A., 2018, Basal continental mantle lithosphere displaced by flat-slab subduction. Nature Geosci 11, 961–964, doi.org/10.1038/s41561-018-0263-9

Baby, P., Rivadeneira, M., Barragán, R., and Christophoul, F., 2013, Thick-skinned tectonics in the Oriente foreland basin of Ecuador: Geological Society., London, Spec.Publ.377, 59–76. doi:10.1144/SP377.1

Baby, P., Rivadeneira, M., Barragán, R., 2004, The Eastern Basin: geology and oil. 144. Travaux de l'Institut Francais des Etudes Andine, pp. 23-44.

Baby Patrice, Rivadeneira Marco, Davila Celso, Galarraga Milton, Rosero Jaime., 1997, Modelo estructural de la parte norte de la cuenca Oriente ecuatoriana. Quito (ECU); Quito : ORSTOM ; PETROPRODUCCION, 31 p. multigr.

Baldock. J.W.,, 1982, Geologia del Ecuador. Boletin de Explicación del mapa geológico de la República del Ecuador. Direccion General de Geologia y Minas, Quito, p. 70.

Balkwill, H., Rodriguez, G., Paredes, F., Almeida, J.,, 1995, Nothern part of Oriente Basin, Ecuador: reflection seismic expression of structures, Petroleum Basins of South America, 62. AAPG Memoirs, pp. 559-571, doi.org/10.1306/M62593C29

Balseca. W., Ferrari. L., Pasquarè. G., Tibaldi. A., 1993, Structural evolution of the Northern sub-Andes of Ecuador: the Napo uplift, Oxford, UK: SecondISAG, pp. 163-166.

Bès de Berc. S., 2003, Tectonique de chevauchement, surrection et incision fluviatile, exemple de la zone subandine equatorianne, (haut bassin amazonien), Phd, Université Toulouse III, pp. 224.

Bicudo, T. C., Sacek, V., & de Almeida, R. P., 2020, Reappraisal of the relative importance of dynamic topography and Andean orogeny on Amazon landscape evolution. Earth and Planetary Science Letters, 546, 116423, doi.org/10.1016/j.epsl.2020.116423

Bourdon, E., Eissen, J.-P., Gutscher, M.-A., Monzier, M., Hall, M. L., & Cotten, J., 2003, Magmatic response to early aseismic ridge subduction: The Ecuadorian margin case, South America, Earth and Planetary Science Letters, 205(3), 123–138, doi.org/10.1016/s0012- 821x(02)01024-5.

Braun, J., 2003, Pecube: a new finite-element code to solve the 3D heat transport equation including the effects of a time-varying, finite amplitude surface topography: Computers and Geosciences, v. 29, no. 6, p. 787-794.

Brichau, S., Reyes, P., Gautheron, C., Hernández, M., Michaud, F., Leisen, M., et al., 2021, First timing constraints on the Ecuadorian Coastal Cordillera exhumation: Geodynamic implications. Journal of South American Earth Sciences, 105, 103007, doi.org/10.1016/j.jsames.2020. 103007.

Bustin, R. M., Link, C., & Goodarzi, F., 1989, Optical properties and chemistry of graptolite periderm following laboratory simulated maturation. Organic geochemistry, 14(4), 355-364, doi.org/10.1016/0146-6380(89)90001-6.

Calderón, Y., Vela, Y., Hurtado, C., Bolaños, R., Baby, P., Eude, A., and Calvès, G., 2017, Petroleum systems restoration of the Huallaga—Marañon Andean retroforeland basin, Peru.

Cediel, F., Shaw, R. P., & Cceres, C., 2003, Tectonic assembly of the northern Andean block.

Chew, D.M., Donelick, R.A., 2012, Combined apatite fission track and U-Pb dating by LA- ICP- MS and its application in apatite provenance analysis. In:

Quantitative Mineralogy and Microanalysis of Sediments and Sedimentary Rocks. Mineralogical Association of Canada Short Course 42, pp. 219–247.

Chew, D.M., Donelick, R.A., Donelick, M.B., Kamber, B.S., and Stock, M., 2014, Apatite chlorine concentration measurements by LA-ICP-MS. Geostandards and Geoanalytical Research, v. 38, no. 1, p. 23–35, doi:10.1111/j.1751-908X.2013.00246.x.

Chew, D.M., Spikings, R.A., 2015, Geochronology and thermochronology using apatite: time and temperature, lower crust to surface. Elements 11, (3), 189–194, doi.org/10.2113/gselements.11.3.189.

Chew, D. M., Babechuk, M. G., Cogne, N., Mark, C., O'Sullivan, G. J., Henrichs, I. A., ... & McKenna, C. A., 2016, LA, (Q)-ICPMS trace-element analyses of Durango and McClure Mountain apatite and implications for making natural LA-ICPMS mineral standards. Chemical Geology, 435, 35-48.

Chiaradia, M., Müntener, O., & Beate, B., 2020, Effects of aseismic ridge subduction on the geochemistry of frontal arc magmas. Earth and Planetary Science Letters, 531, 115984, doi.org/10.1016/j.epsl.2019.115984.

Chlieh, M., Mothes, P. A., Nocquet, J. M., Jarrin, P., Charvis, P., Cisneros, D., et al., 2014, Distribution of discrete seismic asperities and aseismic slip along the Ecuadorian megathrust. Earth and Planetary Science Letters, 400, 292–301, doi.org/10.1016/j.epsl.2014.05.027.

Christophoul, F., Baby, P., Dávila, C., 2002, Stratigraphic responses to a major tectonic event in a foreland basin: the Ecuadorian Oriente Basin from Eocene to Oligocene times. Tectonophysics 345, 281-198.

Christophoul, F., 1999, Discrimination des influences téctonique et eustatiques dans les basins liés a des zones de convergence: examples du bassin subandin d’Equateur. Thése Université Tolouse III – Paul Sabatier, 184.

Cochrane, R., Spikings, R.A., Chew, D., Wotzlaw, J.-F., Chiaradia, M., Tyrrell, S., Schaltegger, U., der Lelij, R.V., 2014, High temperature, >350(◦C) thermochronology and mechanisms of Pb loss in apatite. Geochim Cosmochim Acta 127, 39–56, doi.org/10.1016/j.gca.2013.11.028

Cochrane, R., 2013, U-Pb Thermochronology, Geochronology and Geochemistry of NW South America: Rift to Drift Transition, Active Margin Dynamics and Implications for the Volume Balance of Continents. PhD. Thesis. University of Geneva, p. 191, doi.org/10.13097/archive-ouverte/unige:30029.

Cogné, N., Chew, D.M., Donelick, R.A., Ansberque, C., 2020, LA-ICP-MS apatite fission track dating: A practical zeta-based approach. Chemical Geology,v. 531. doi: 10.1016/j.chemgeo.2019.119302.

Cogné, N., Doepke, D., Chew, D., Stuart, F.M., Mark, C., 2016, Measuring plume-related exhumation of the British Isles in Early Cenozoic times, Earth and Planetary Science Lettes 456, pp. 1-15, doi.org/10.1016/j.epsl.2016.09.053.

Cogné, N., Chew, D., & Stuart, F. M., 2014, The thermal history of the western Irish onshore. Journal of the Geological Society, 171(6), 779-792.

Dashwood, M.F., Abbots, I.L., 1990, Aspects of the petroleum geology of the Oriente Basin, Ecuador, (In: Books, J., Ed.), Classic Petroleum Provinces, 50. Geol. Soc. London. Spec. Publ, pp. 89-117, doi.org/10.1144/GSL.SP.1990.050.01.06.

DeMets, C., Gordon, R. G., & Argus, D. F., 2010, Geologically current plate motions. Geophysical journal international, 181(1), 1-80.

Deniaud, Y., 1999, Enregistrements sédimentaire et structural de l'évolution géodynamique des Andes Equatoriennes au cours du Néogène: Étude des bassins d'avant-arc et bilans de masse, Géologie Alpine, Mémoire H.S, 32, p. 157, Université Joseph Fourier Grenoble.

Derycke, A., Gautheron, C., Barbarand, J., Bourbon, P., Aetgeerts, G., Simon-Labric, T., Sarda, P., Pinna-Jamme, R., Boukari, C., & Haurine, F., 2021, French Guiana margin evolution: From Gondwana break-up to Atlantic opening. Terra Nova, 33, 415–422.

Díaz, M., Baby, P., Rivadeneira, M., Christophoul, F., 2003, El PreAptense en la Cuenca Oriente Ecuatoriana. In: Memorias del VIII Simposio Bolivariano – exploracio´n petrolera en las Cuencas Subandinas, Cartagena, Colombia, pp. 208–222

Dominguez, S., Lallemand, S. E., Malavieille, J., & von Huene, R., 1998, Upper plate deformation associated with seamount subduction. Tectonophysics, 293(3–4), 207–224, doi.org/10.1016/s0040-1951(98)00086-9

Dumitru, T.A., 1993, A new computer-automated microscope stage system for fission-track analysis. Nuclear Tracks and Radiation Measurements, Volume 21, Issue 4, Pages 575-580; https://doi.org/10.1016/1359-0189(93)90198-I.

Dumont, J.F., Santana, E., Vilhena, W., Pedoja, K., Ordoñez, M., Cruz, M., Jiménez, N., and Zambrano, I., 2005, Morphological and microtectonic analysis os Quaternary deformation from Puná and Santa Clara Islands, Gulf of Guayaquil, Ecuador, South America, Tectonophysics, 399, 331-350.

Espinosa, A. F., Hall, M. L., and Yepes, H.,, 1991, Tectonics and seismicity, Ecuador Earthquakes – Mass Wasting and Socioeconomic Effects: Natural Disaster Studies. National Academies Press, Washington, DC, 5, p. 29–41.

Egbue, O., and Kellogg, L., 2010, Pleistocene to present North Andean ‘escape’. Tectonophysics, 489, 248-257, doi: 10.1016/j.tecto.2010.04.021

Ego, F., Sébrier, M., Lavenu, A., Yepes, H., and Eguez, A., 1996, Quaternary state of stress in the Northern Andes and the restraining bend model for the Ecuatorian Andes. Tectonophysics, 259, 101-116.

Eguez, A., Alvarado, A., Yepes, H., Machete, M.N., Costa, C., and Dart, R., 2003, Database and map of Quaternary faults and folds in Ecuador and its offshore region, U.S. Geol. Surv. Open File Report 03-289. International Lithosphere Program's Task Group II-2 "World Map of Major Active Faults. [Available at http://pubs.usgs.gov/of/2000/ofr-03-289/.]

Faucher, B., Vernet, R., Bizon, G., Bizon, J., Grekoff, M., Lys, M., Sigal, J., 1971, Sedimentary formations in Ecuador. A stratigraphic and micropaleontological survey, Bureau Etudes Idust. Coop., BEICIP-IFC 3.

Faucher, B., Savoyat, E., 1973, Esquisse géologique des Andes de l'Equateur. Rev. Géographie Phys. Geol. Dyn., 2), XV(fasc. 1-2), 115-142.

Farley, K.A., Wolf, R.A., and Silver, L.T., 1996, The effects of long alpha-stopping distances on, (U-Th)/He ages. Geochimica et Cosmochimica Acta, v. 60, no. 21, p. 4223-4229, doi:10.1016/S0016-7037(96)00193-7.

Flórez-Rodríguez, A. G., Schellart, W. P., & Strak, V., 2019, Impact of aseismic ridges on subduction systems: Insights from analog modeling. Journal of Geophysical Research: Solid Earth, 124(6), 5951–5969, doi.org/10.1029/2019jb017488.

Flowers, R. M., Ketcham, R. A., Enkelmann, E., Gautheron, C., Reiners, P. W., Metcalf, J. R., ... & Brown, R. W., 2023, (U-Th)/He chronology: Part 2. Considerations for evaluating, integrating, and interpreting conventional individual aliquot data. Bulletin, 135(1-2), 137-161.

Flowers, R. M., Ketcham, R. A., Shuster, D. L., & Farley, K. A., 2009, Apatite, (U–Th)/He thermochronometry using a radiation damage accumulation and annealing model. Geochimica et Cosmochimica Acta, 73(8), 2347–2365, doi.org/10.1016/j.gca.2009.01.015.

Fossen, H., 2010, Structural Geology, Cambridge University Press.

Gaibor, J., Hochuli, J.P.A., Winkler, W., Toro, J., 2008, Hydrocarbon source potential of the Santiago Formation, Oriente Basin, SE of Ecuador. J. S. Am. Earth Sci. 25, 145–156, doi.org/10.1016/j.jsames.2007.07.002.

Gajardo, E., Yepes, H., Ramón, P., Hall, M.L., Mothes, P., and Aguilar, J., 2001, Evaluación del peligro sísmico para la ruta del OCP y evaluación complementaria del peligro volcánico, Escuela Politécnica Nacional, Instituto Geofísico, Internal Report.

Galbraith, R.F., 1981, On statistical models for fission track counts. J Int Assoc Math Geol 13, (6), 471–478, doi.org/10.1007/BF01034498.

Gallagher, K., 2012, Transdimensional inverse thermal history modeling for quantitative thermochronology: Journal of Geophysical Research: Solid Earth, v. 117, no. B2.

Gautheron, C., Tassan-Got, L., 2010, A Monte Carlo approach of diffusion applied to noble gas/helium thermochronology. Chemical Geology 273, 212–224.

Gautheron, C., Pinna-Jamme, R., Derycke, A., Ahadi, F., Sanchez,C., Haurine, F., Monvoisin, G., Barbosa, D., Delpech, G., Mal-tese, J., Sarda, P., and Tassan-Got, L., 2021, Technical note: Analyticalprotocols and performance for apatite and zircon, (U–Th) /Heanalysis on quadrupole and magnetic sector mass spectrometersystems between 2007 and 2020, Geochronology, 3, 351–370, doi.org/10.5194/gchron-3-351-2021.

George, S. W. M., Perez, N. D., Struble, W., Curry, M. E., & Horton, B. K., 2023, Aseismic ridge subduction focused late Cenozoic exhumation above the Peruvian flat slab. Earth and Planetary Science Letters, 600, 117754, doi.org/10.1016/j.epsl.2022.117754.

Gutiérrez, E.G., Horton, B.K., Vallejo, C., Jackson, L.J., George, S.W., 2019, Provenance and geochronological insights into Late Cretaceous–Cenozoic foreland basin development in the Subandean Zone and Oriente Basin of Ecuador, Andean Tectonics, 1. Elsevier, pp. 237–268, doi.org/ 10.1016/B978-0-12-816009-1.00011-3.

Gutscher, M.A., Olivet, J.L., Aslanian, D., Eisser, J.P., Maury, R., 1999, The “lost inca plateau”: cause of flat subduction beneath peru?, Earth and Planetary Science Letters 171, pp. 335-341, doi.org/10.1016/S0012-821X(99)00153-3.

Gutscher, M.A., 2002, Andean subduction styles and their effect on thermal structure and interplate coupling, Journal of South American Earth Sciences 15, pp. 3-10, doi.org/10.1016/S0895-9811(02)00002-0.

Horton, B. K., Capaldi, T. N., & Perez, N. D., 2022, The role of flat slab subduction, ridge subduction, and tectonic inheritance in Andean deformation. Geology, 50(9), 1007–1012, doi.org/10.1130/g50094.1.

Horton, B.K., 2018, Sedimentary record of Andean mountain building. Earth Sci. Rev. 178, 279–309, doi.org/10.1016/j.earscirev.2017.11.025.

Hughes, R., Pilatasig, L., 2002, Cretaceous and Tertiary terrane accretion in the Cordillera Occidental of the Andes of the Ecuador, Tectonophysics, 245, 29-48.

Jackson, L. J., Horton, B. K., & Vallejo, C., 2019, Detrital zircon U-Pb geochronology of modern Andean rivers in Ecuador: Fingerprinting tectonic provinces and assessing downstream propagation of provenance signals. Geosphere, 15(6), 1943-1957.

Jaillard, E., Ordoñez O., Suárez, J., Toro, J., Iza, D., Lugo, W., 2004, Stratigraphy of the Late Cretaceous-Paleogene deposits of the cordillera occidental of central Ecuador: Geodynamic implications, J. South Am. Earth Sci., 17, 49-58.

Jaillard, E., Bengtson, P., Dhondt, A.V., 2005, Late Cretaceous marine transgressions in Ecuador and northern Peru: A refined stratigraphic framework. J. South Am. Earth Sci. 19, 307-323, doi.org/10.1016/j.jsames.2005.01.006.

Jaillard, E., Lapierre, H., Ordoñez, M., Toro, J., Amortegui, A., Vanmelle, J., 2009, Accreted oceanic terranes in Ecuador: Southern edge of the Caribbean plate ? Geol. Soc. London Spec. Publ., 328, 469-485, doi: 10.1144/SP328.19.

Jepson, G., Carrapa, B., George, S., Triantafyllou, A., Egan, S., Constenius, K., et al., 2021, Resolving mid-to upper-crustal exhumation through apatite petrochronology and thermochronology. Chemical Geology, 565, 120071, doi.org/10.1016/j.chemgeo.2021.120071

Kawakatsu, H., Proaño, G., 1991, Focal mechanism of the March 6, 1987 Ecuador earthquackes-CMT inversion with a first motion constraint, J. Phys. Earth, 39, 589-597.

Kerr. C.A., Tarney. J., Kempton. P.D., Spadea. P., Nivia. A., Marriner. G.F., Duncan. R.A., 2002, Pervasive mantle plume head heterogeneit: Evidence from late Cretaceous Caribbean-Colombian oceanic plateau. Journal of Geophysical Research: Solid Earth 107, nº. B7, p. ECV 2-1-ECV 2-13, doi.org/10.1029/2001JB000790

Ketcham, R.A., Carter, A., Donelick, R.A., Barbarand, J., Hurford, A.J., 2007, Improved modeling of fission-track annealing in apatite. American Mineralogist 92, 799–810.

Ketcham, R.A., Gautheron, C., Tassan-got, L., 2011, Accounting for long alpha-particle stopping distances in, (U–Th–Sm)/He geochronology: refinement of the baseline case. Geochimica et Cosmochimica Acta 75, 7779–7791

Ketcham, R.A., 2005): Forward and inverse modeling of low-temperature thermochronometry data, Low-Temperature Thermochronology: Techniques, Interpretations, and Applications: Rev. Mineral. Geochem., 58, 275-314.

Lallemand, S. E., Malavieille, J., & Calassou, S., 1992, Effects of oceanic ridge subduction on accretionary wedges: Experimental modeling and marine observations. Tectonics, 11(6), 1301–1313, doi.org/10.1029/92tc00637.

Laslett, G.M., McBratney, A.B., Pahl, P.J., Hutchinson, M.F., 1987, Comparison of several spatial prediction methods for soil pH. Journal of Soil Science 32, 2, pp. 325-241. doi: 10.1111/j.1365-2389.1987.tb02148.x.

Lee, G. H., Eissa, M. A., Decker, C. L., Castagna, J. P., O’Meara, D. J. & Marin, H. D. 2004. Aspects of the petroleum geology of the Bermejo field, northwestern Oriente basin, Ecuador. Journal of Petroleum Geology, 27, 335–356.

Legrand, D., Baby, P., Bondoux, F., Dorbath, C., Bès de Berc, S., Rivadeneira, M., 2005, The 1999-2000 seismic experiment of Macas swarm, (Ecuador) in relation with rift inversion in Subandean foothills. Tectonophysics, 395, 67-80.

Litherland, M., Aspden, J.A.,, 1992, Terrane-boundary reactivation: a control on the evolution of the Northern Andes. Journal of South American Earth Sciences 5, 71e76.

Litherland, M., Aspden, J., Jemielita, R.A.,, 1994, The metamorphic belts of ecuador. Overs. Mem. Geol. Surv. 11, 1-147.

Luzieux, L.D.A., Heller, F., Spikings, F., Vallejo, C.F., Winkler, W., 2006, Origin and cretaceous tectonic history of the coastal Ecuadorian forearc between 1º N and 3º S: 400-414, doi.org/10.1016/j.epsl.2006.07.008.

Luzieux, L., 2007, Origin and Late Cretaceous-Tertiary evolution of the Ecuadorian forearc, Doctoral dissertation, ETH Zurich,

Margirier, A., Strecker, M. R., Reiners, P. W., Thomson, S. N., Casado, I., George, S. W., & Alvarado, A., 2022, Late Miocene exhumation of the Western Cordillera, Ecuador, driven by increased coupling between the subducting Carnegie Ridge and the South American continent. Tectonics, 42(1), e2022TC007344. https://doi.org/10.1029/2022TC007344.

Malusa, M.G., Fitzgerald, P.G., Eds.,, 2019, Fission-Track Thermochronology and its Application to Geology, doi.org/10.1007/978-3-319-89421-8.

Martin-Gombojav, N., & Winkler, W., 2008, Recycling of Proterozoic crust in the Andean Amazon foreland of Ecuador: implications for orogenic development of the Northern Andes. Terra Nova, 20(1), 22-31, doi.org/10.1111/j.1365-3121.2007.00782.x.

McDowell, D.D., McIntosh, W.C. & Farley, K.A., 2005, A precise 40Ar–39Ar reference age for the Durango apatite, (U–Th)/He and fission-track dating standard. Chem. Geol., 214: 249-263.

Meesters, A.G.C.A., and Dunai, T.J., 2005, A non-iterative solution of the, (U-Th)/He age equation. Geochemistry, Geophysics, Geosystems, (G3), v. 6, no. 4, Q04002, 3 p., doi:10.1029/2004GC000834.

Meffre, S., Crawford, A., 2001, Collision tectonics in the New Hebrides arc, Vanuatu, Island Arc 10, p. 33-50, doi.org/10.1046/j.1440-1738.2001.00292.x.

Mégard, F., 1984, The Andean orogenic period and its major structures in central and northern Peru. Journal of the Geological Society, 141(5), 893–900, doi.org/10.1144/gsjgs.141.5.0893

Miskovíc, A., Spikings, R.A., Chew, D.M., Koˇsler, J., Ulianov, A., Schaltegger, U., 2009, Tectonomagmatic evolution of Western Amazonia: geochemical characterization and zircon U-Pb geochronologic constraints from the Peruvian Cordillera real granitoids: Bull. Geol. Soc. Am. 121, 1298–1324, https://doi.org/10.1130/ B26488.1.

Mora, J.A., Oncken, O., Le Breton, E., Ibánez-Mejia, M., Faccenna, C., Veloza, G., Vélez, V., Freitas, M., Mesa, A., 2017, Linking late Cretaceous to Eocene tectonostratigraphy of the San Jacinto Fold Belt of NW Colombia with Caribbean Plateau collision and flat subduction. Tectonics 36, (11), 2599–2629.

Moreno, F., Garzione, C. N., George, S. W., Horton, B. K., Williams, L., Jackson, L. J., et al., 2020, Coupled Andean growth and foreland basin evolution, Campanian–Cenozoic Bagua Basin, northern Peru. Tectonics, 39(7), e2019TC005967 doi.org/10.1029/2019tc005967

Montes, C., Rodriguez-Corcho, A.F., Bayona, G., Hoyos, N., Zapata, S., Cardona, A., 2019, Continental margin response to multiple arc-continent collisions: The northern Andes-Caribbean margin, Earth-Science Reviews 198, doi.org/10.1016/j.earscirev.2019.102903.

Montes, C. & Hoyos, N., 2020, Isthmian bedrock geology: Tilted, bent, and broken, The Geology of Colombia, Volume 3 Paleogene – Neogene. Servicio Geológico Colombiano, Publicaciones Geológicas Especiales 37, p. 451–467. Bogotá, doi.org/10.32685/pub.esp.37.2019.15.

Nocquet, J. M., Jarrin, P., Vallée, M., Mothes, P. A., Grandin, R., Rolandone, F., et al., 2017, Supercycle at the Ecuadorian subduction zone revealed after the 2016 Pedernales earthquake. Nature Geoscience, 10(2), 145–149, doi.org/10.1038/ngeo2864.

Nocquet, J.M., et al., 2014, Motion of continental slivers and creeping subduction in the northern Andes. Nat. Geosci., doi: 10.1038/ngeo2099.

O'Sullivan, G., Chew, D., Kenny, G., Henrichs, I., Mulligan, D., 2020, The trace element composition of apatite and its application to detrital provenance studies. Earth Sci Rev 201, 103044, doi.org/10.1016/j.earscirev.2019.103044

Pardo, M., Comte, D., & Monfret, T., 2002, Seismotectonic and stress distribution in the central Chile subduction zone. Journal of South American Earth Sciences, 15(1), 11-22, doi.org/10.1016/S0895-9811(02)00003-2.

Pardo-Casas, F., & Molnar, P., 1987, Relative motion of the Nazca (Farallon) and South American plates since Late Cretaceous time. Tectonics, 6(3), 233–248, doi.org/10.1016/0198-0254(87)96011-0

Pasquarè, Cl., Tibaldi, A. and Ferrari, L., 1990, Relationships between plate convergence and tectonic evolution of the Ecuadorian active Thrust Belt. In: Critical Aspects of Plate Tectonic Theory. Theophrastus Publications, Athens, pp. 365-387.

Paton, C., Hellstrom, J., Paul, B.,Woodhead, J. and Hergt, J, 2011, Iolite: Freeware for the visualization and processing of mass spectrometric data. Journal of Analytical Atomic Spectrometry. doi:10.1039/c1ja10172b.

Paul, A.N., Spikings, R.A., Chew, D., Daly, S.J., 2019, The effect of intra-crystal uranium zonation on apatite U-Pb thermochronology: A combined ID-TIMS and LA-MC-ICP- MS study. Geochim Cosmochim Acta 251, 15–35., doi.org/10.1016/j.gca.2019.02.013

Parra, M., Mora, A., Jaramillo, C., Torres, V., Zeilinger, G., & Strecker, M. R., 2010, Tectonic controls on Cenozoic foreland basin development in the north-eastern Andes, Colombia. Basin Research, 22(6), 874-903.

Pepper, M., Gehrels, G., Pullen, A., Ibanez-Mejia, M., Ward, K. M., & Kapp, P., 2016, Magmatic history and crustal genesis of western South America: Constraints ,from U-Pb ages and Hf isotopes of detrital zircons in modern rivers. Geosphere, 12(5), 1532-1555., doi.org/10.1130/GES01315.1

Pérez-Consuegra, N., Hoke, G. D., Mora, A., Fitzgerald, P., Sobel, E. R., Sandoval, J. R., et al. ,2021, The case for tectonic control on erosional exhumation on the tropical Northern Andes based on thermochronology data. Tectonics, 40, e2020TC006652, doi. org/10.1029/2020TC006652

Pilger, R. H., 1981, Plate reconstructions, aseismic ridges, and low-angle subduction beneath the Andes. The Geological Society of America Bulletin, 92(7), 448–456, doi.org/10.1130/0016-7606(1981)92<448:praral>2.0.co;2

Pilger, R. H., 1984, Cenozoic plate kinematics, subduction and magmatism: South American Andes. Journal of the Geological Society, 141(5), 793–802, doi.org/10.1144/gsjgs.141.5.0793.

Pindell, J., Kennan, L., Maresch, W.V., Stanek, K.-P., Draper, G., Higgs, R., 2005, Plate kinematics and crustal dynamics of circum-Caribbean arc-continent interactions; tectonic controls on basin development in proto-Caribbean margins, Caribbean-South America Plate Interactions, Venezuela. 394. pp. 7–52.

Pousse-Beltran, L., Vassallo, R., Audemard, F., Jouanne, F., Carcaillet, J., Pathier, E., & Volat, M., 2017, Pleistocene slip rates on the Boconó fault along the North Andean Block plate boundary, Venezuela. Tectonics, 36(7), 1207-1231.

Pratt, W., Duque, P., Ponde, M., 2005, An autochthonous geological model for the eastern Andes of Ecuador. Tectonophysics, 399, 251-278.

Ramos, V. A., 2005, Seismic ridge subduction and topography: Foreland deformation in the Patagonian Andes. Tectonophysics, 399(1–4), 73–86, doi.org/10.1016/j.tecto.2004.12.016.

Rivadeneira, M., Baby, P., 1999, La Cuenca Oriente: estilo tectónico, etapas de deformacion y características geológicas de los principales campos de Petroproducción. Quito-Ecuador, p. 88.

Rivadeneira, M., Baby, P., 2004, Características geologicas generales de los principales campos petroleros de Petroproducción, La cuenca Oriente: Geología Y Petroleo, Travaux de l'Institut Français des Études Andine, vol. 144, pp. 229-294.

Rivadeneira, M., & Ramirez, F., 1985, La zona Subandina Ecuatoriana y sus prospectos hidrocarburiferos. In Congreso latinoamericano de geologia. 6, pp. 491-507,

Rosenbaum, G., & Mo, W., 2011, Tectonic and magmatic responses to the subduction of high bathymetric relief. Gondwana Research, 19(3), 571–582, doi.org/10.1016/j.gr.2010.10.007.

Rosero-Castillo, J.E.,, 1997, Estructuras y etapas de deformacion de la zona subandina en el Oriente Ecuatoriano, entre 0º10 'S y 0º50'S, Tesis previa a la obtencíon del titulo de Ingeniero Geólogo, Escuela Politecnica Nacional, Quito, 87p.

Ruiz, G., 2002, Exhumation of the nothern Sub-Andean Zone of Ecuador and its source region: a combined thermochrono- logical and heavy mineral approach. Unpublished PHD Thesis, 14905, ETH, Zurich, Switzerland, doi.org/103929/ethz-a-004489528

Ruiz, G.M.H., Seward, D., Winkler, W., 2004, Detrital thermochonology - a new perspective on hinterland tectonics, an example from the Andean Amazon Basin, Ecuador. Basin Res. 16, 413-430, doi.org/10.1111/j.1365-2117.2004.00239.x.

Ruiz, G.M.H., Seward, D., Winkler, W., 2007, Evolution of the Amazon Basin in Ecuador with special reference to hinterland tectonics: data from zircon fission-track and heavy mineral analysis. Dev. Sedimentol. 58, 907-934, doi.org/10.1016/S0070-4571(07)58036-2.

Schoene, B., & Bowring, S. A., 2006, U–Pb systematics of the McClure Mountain syenite: thermochronological constraints on the age of the 40Ar/39Ar standard MMhb. Contributions to Mineralogy and Petrology, 151(5), 615-630.

Schütt, J. M., & Whipp, D. M., 2020, Controls on continental strain partitioning above an oblique subduction zone, Northern Andes. Tectonics, 39(4), 725, doi.org/10.1002/2015TC003941.

Singh, S. C., Hananto, N., Mukti, M., Robinson, D. P., Das, S., Chauhan, A., et al., 2011, Aseismic zone and earthquake segmentation associated with a deep subducted seamount in Sumatra. Nature Geoscience, 4(5), 308–311, doi.org/10.1038/ngeo1119.

Siravo, G., Faccenna, C., Gérault, M., Becker, T. W., Fellin, M. G., Herman, F., & Molin, P., 2019, Slab flattening and the rise of the Eastern Cordillera, Colombia. Earth and Planetary Science Letters, 512, 100-110, doi.org/10.1016/j.epsl.2019.02.002

Shanmugam, G., Poffenberger, M. and Toro Alava, J., 2000, Tide-dominated estuarine facies in the Hollín and Napo (‘‘T’’ and ‘‘U’’) formations, (Cretaceous), Sacha Field, Oriente Basin, Ecuador. AAPG Bull., 84, 652–682.

Spikings, R., Seward, D., Winkler, W., Ruiz, G.M., 2000, Tectonics 19, 2000, 649-668.

Sébrier, M., Mercier, J. L., Macharé, J., Bonnot, D., Cabrera, J., & Blanc, J. L., 1988, The state of stress in an overriding plate situated above a flat slab: The Andes of central Peru. Tectonics, 7(4), 895–928, doi.org/10.1029/tc007i004p00895

Spikings, R., Seward, D., Handler, R., 2001, Along-strike variations in the termal and tectonic response of the continental Ecuadorian Andes to the collision with heterogeneous oceanic crust. Earth Planet. Sci. Lett., 186, 57-73.

Spacapan, J., Brisson, I., Comerio, M., Giampaoli, P., Pineda, J. A., and Di Benedetto, M., 2023, Petroleum system modeling in complex tectonic setting; a study case of the Huallaga-Marañon retroforeland basin system, Peru. Marine and Petroleum Geology, 154, 106326.

Spikings, R. A., & Crowhurst, P. V., 2004, (U-Th)/He thermochronometric constraints on the late Miocene-Pliocene tectonic development of the northern Cordillera Real and the Interandean Depression, Ecuador. Journal of South American Earth Sciences, 17(4), 239–251, doi. org/10.1016/j.jsames.2004.07.001.

Spikings, R., Winkler, W., Hughes, R., Handler, R., 2005, Thermochronology of allochthonous terranes in Ecuador: Unravelling the accretionary and post-accetionary history of the Northern Andes. Tectonophysics, 399, 195-220.

Spikings, R., Crowhurst, P.V., Winkler, W., Villagomez, D., 2010, Syn- and postaccretionary cooling history of the Ecuadorian Andes constrained by their in- situ and detrital thermochronometric record. J. S. Am. Earth Sci. 30, 121-133, doi.org/10.1016/j.jsames.2010.04.002

Spikings, R.A., Cochrane, R.S., Villegomez, D., Van der Lelij, D., Vallejo, C., Winkler, W., Beate, B., 2015, The geological history of northwestern South America: from Peagaea to the early collision of the Caribbean large Igneous Province, 290-75 Ma, Gondwana Res. 27, 95-139, doi.org/10.1016/j.gr.2014.06.004.

Spikings, R.A., Paul, A., Vallejo, C., Reyes, P., 2021, Constraints on the ages of the crystalline basement and Palaeozoic cover exposed in the Cordillera real, Ecuador: 40Ar/39Ar analyses and detrital zircon U/Pb geochronology. Gond. Res. 90, 77–101, doi.org/10.1016/j.gr.2020.10.009.

Tagami, T., Galbraith, R. F., Yamada, R., & Laslett, G. M., 1998, Revised annealing kinetics of fission tracks in zircon and geological implications. In Advances in Fission-Track Geochronology: A selection of papers presented at the International Workshop on Fission-Track Dating, Ghent, Belgium, 1996, pp. 99-112, Springer Netherlands.

Taylor, F. W., Mann, P., Bevis, M. G., Edwards, R. L., Cheng, H., Cutler, K. B., et al., 2005, Rapid forearc uplift and subsidence caused by impinging bathymetric features: Examples from the New Hebrides and Solomon arcs. Tectonics, 24, 6, doi.org/10.1029/2004tc001650.

Thomas, G., Lavenu, A., Berrones, G., 1995, Subsidence evolution of the northern part of the Ecuadorian Oriente Basin, Upper Cretaceous to Present, C. R. Acad Sci II 320, 617–624.

Thomson, S. N., Brandon, M. T., Reiners, P. W., Tomkin, J. H., Vásquez, C., & Wilson, N. J., 2010, Glaciation as a destructive and constructive control on mountain building. Nature, 467(7313), 313–317, doi.org/10.1038/nature09365.

Trenkamp, R., Kellogg, J. N., Freymueller, J. & Mora, H. P., 2002, Wide plate margin deformation, southern Central America and northwestern South America, CASA GPS observations. Journal of South American Earth Sciences, 15, 157–171.

Tschopp, H. J., 1953, Oil explorations in the Oriente of Ecuador. AAPG Bulletin, 37, 2303–2347.

Vallejo, C., & Buitron, A., 1999, Estudio estratigrafico estructural de la Zona Subandina norte, entre los paralelos 08250Sy08400S, Doctoral dissertation, Thesis de grado. Escuela Politécnica Naciónal, EPN), Quito,

Vallejo, C., Winler, W., Spikings, R.A., Luzieux, L., Heller, F., Bussy, F., 2009, Mode and time of terrane accretion in the foreac of the Andes in Ecuador. Geol. Soc. Am. Mem. 204, 197-216, doi.org/10.1130/2009.1204(09,

Vallejo, C.; Romero, C.; Horton, B.K.; Spikings, R.A.; Gaibor, J.; Winkler, W.; Esteban, J.J.; Thomsen, T.B.; Mariño, E., 2021, Jurassic to Early Paleogene sedimentation in the Amazon region of Ecuador: Implications for the paleogeographic evolution of northwestern South America. Global and Planetary Change, 204, doi.org/10.1016/j.gloplacha.2021.103555.

Vallejo, C., Winkler, W., Spikings, R.A., Luzieux, L., Heller, H., Bussy, F., 2009, Mode and timing of terrane accretion in the forearc of the Andes of Ecuador. Geological Society of America Bulletin 204, 197e216.

Vallejo, C., Spikings, R.A., Winkler, W., Luzieux, L., Chew, D., Page, L., 2006, The early interaction between the Caribbean plateau and the NW south American plate. Terra Nova 18, 264-269, doi.org/10.1111/j.1365-3121.2006.00688.x

Valarezo, M.E., Vallejo, C., Horton, B.K., Gaibor, J., Esteban, J., Jackson, L.J., Carrasco, H., Winkler, W., Bernal, C., Beate, B., 2019, Sedimentological and provenance analysis of the Río Playas stratigraphic section: Implications for the evolution of the Alamor-Lancones Basin of southern Ecuador and northern Peru. J. S. Am. Earth Sci. 94, 102239, doi.org/10.1016/j.jsames.2019.102239

Vermeesch, P., 2018, Isoplotr: A free and open toolbox for geochronology, Geoscience Frontiers 9(5), 1479–1493. http://www.sciencedirect.com/science/article/pii/S1674987 118300835

Vermeesch, P., Avigad, D., McWilliams, M.O., 2009, 500 m.y. of thermal history elucidated by multi-method detrital thermochronology of North Gondwana Cambrian sandstone, Eilat area, Israel, Bull. Geol. Soc. Am. 121, (7–8), 1204–1216, doi. org/10.1130/B26473.1.

Von Huene, R., Corvalán, J., Flueh, E. R., Hinz, K., Korstgard, J., Ranero, C. R., & Weinrebe, W., 1997, Tectonic control of the subducting Juan Fernández Ridge on the Andean margin near Valparaiso, Chile. Tectonics, 16(3), 474–488, doi.org/10.1029/96tc03703.

Whattam, S. A., and Stern, R. J., 2015, Late Cretaceous plume-induced subduction initiation along the southern margin of the Caribbean and NW South America: The first documented example with implications for the onset of plate tectonics. Gondwana Research, 27(1), 38-63.

White, R.Y., Tarney, J, Kerr, A.C., Saunders, AD., Kernpton, P.D., Pringle, M.S. & Klaver, G.Th., 1999, Modification of an oceanic plateau, Aruba, Dutch Caribbean: Implications for the generation of continental crust. Lithos 46, 43-68.

Winkler, W., Villagómez, D., Spikings, R., Abegglen, P., Tobler, S., Eguez, A., 2005, The Chota basin and its significance for the inception and tectonic setting of the inter-Andean depression in Ecuador, J. South Am. Earth Sci., 19, 5-10.

Witt, C., Bourgois, J., Michaud, F., Ordoñez, M., Jiménez, N., Sosson, M., 2006, Development of the Gulf of Guayaquil, (Ecuador) during the Quaternary as an effect os the North Andean block tectonic escape. Tectonics, 25, TC3017, doi: 10.1029/2004TC001723.

Woodhead, J., Hellstrom, J., Hergt, J., Greig, A. & Maas, R., 2007, Isotopic and elemental imaging of geological materials by laser ablation Inductively Coupled Plasma mass spectrometry. Journal of Geostandards and Geoanalytical Research, 31, p. 331-343.

Yepes, H., L. Audin, A. Alvarado, C. Beauval, J. Aguilar, Y. Font, and F. Cotton.,, 2016, Tectonics, 35(5), 1249–1279, doi:10.1002/2015TC003941.

Appendix A. LA-ICP-MS

Electronic Material 1. Operating conditions for AFT dating

	Apatite Fission Track analyses
Laboratory & Sample Preparation	
Laboratory name	GeOHeLiS Analytical Platform, Géosciences Rennes/OSUR, Univ. Rennes
Sample type/mineral	Apatites from basement rocks
Sample preparation	15mm resin mount, 1µm polish to finish
Laser ablation system	
Make, Model & type	ESI NWR193UC, Excimer
Ablation cell	ESI NWR TwoVol2
Laser wavelength	193 nm
Pulse width	< 5 ns
Fluence	4 J/cm-2
Repetition rate	5 Hz
Spot size	35*35 µm (square spot)
Pit Depth	Approx. 13 µm
Sampling mode / pattern	Single spot
Carrier gas	100% He, Ar make-up gas and N$_2$ (3 ml/mn) combined using in-house smoothing device
Background collection	10 seconds
Ablation duration	30 seconds
Wash-out delay	10 seconds
Cell carrier gas flow (He)	0.75 l/min
ICP-MS Instrument	
Make, Model & type	Agilent 7700x, Q-ICP-MS
Sample introduction	Via conventional tubing
RF power	1350W
Sampler, skimmer cones	Ni
Extraction lenses	X type
Make-up gas flow (Ar)	0.75 l/min
Detection system	Single collector secondary electron multiplier
Data acquisition protocol	Time-resolved analysis
Scanning mode	Peak hopping, one point per peak
Detector mode	Pulse counting, dead time correction applied, and analog mode when signal intensity > ~ 10^6 cps
Masses measured	^{35}Cl, ^{43}Ca, ^{86}Sr, ^{89}Y, ^{139}La, ^{140}Ce, ^{141}Pr, ^{146}Nd, ^{147}Sm, ^{153}Eu, ^{157}Gd, ^{159}Tb, ^{163}Dy, ^{165}Ho, ^{166}Er, ^{169}Tm, ^{172}Yb, ^{175}Lu, ^{204}(Hg + Pb), ^{206}Pb, ^{207}Pb, ^{208}Pb, ^{232}Th, ^{238}U
Integration time per peak	10-30 ms
Sensitivity / Efficiency	28000 cps/ppm Pb (50µm, 10Hz)
Dwell time per isotope	5-70 ms depending on the masses – total cycle 428ms
Data Processing	
Gas blank	20 seconds on-peak
Calibration strategy	NIST 612 and Durango apatite
Data processing package used	Iolite v4.3 (Paton et al., 2011), Trace_Elements DRS (Woodhead et al., 2007) with Weighted U/Ca pluggin (Cogné et al., 2020)

Appendix B. Raw data for QTQt modeling

Data set for modeling integrated new and published thermochronological data

Sample	Unit	Distance (m) to the unconformity between Albian Hollín Fm and Late Jurassic Misahuallí Fm	Elev (m.s.l)	Lithology	Stratigraphic age (Ma)	Apatite U-Pb age ± error (2σ) (Ma)	AFT age ± error (2σ) (Ma)	MTL ± error (1σ) (1 s.e.) (μm) (n)	ZFT central age ± error (2σ) (Ma)	Mean corrected AHe age ± error (1σ) (SD) (Ma)
Sub-Andean Thrust Belt (SATB)										
11 (Jp)	JP	0	1619		170.0 ± 5.0	-	6.4 ± 1.8	14.35 (1)	-	-
04 (Jp)	JP	-150	1910		170.0 ± 5.0	-	6.2 ± 3.2	-	46.0 ± 5.2	-
08 (Jp)	JP	-2000	1843		170.0 ± 5.0	-	2.5 ± 1.0	15.07 (1)	55.7 ± 5.4	-
09 (Jp)	JP	-1650	2241		170.0 ± 5.0	-	2.8 ± 1.2	-	-	-
Abitagua Block										
03 (Ab)	Ab	-85	2159	Feldspar phyric granite	170.0 ± 0.7	-	161.0 ± 15.0	10.3 ± 3.5 (10)	176.0 ± 38.0	-
22NP25	Ab	-365	2137		170.0 ± 0.7	185.6 ± 26	27.2 ± 8.2	12.4 ± 0.2 (4)	-	12.3 ± 1.2
17 (Ab)	Ab	-485	1280	Mica-rich granite (Py)	170.0 ± 0.7	-	9.9 ± 2.4	11.7 ± 1.2 (6)	132.0 ± 16.0	-
18 (Ab)	Ab	-785	543	Medium granite	170.0 ± 0.7	-	5.0 ± 1.8	12.1 ± 1.7(11)	113.0 ± 12.0	-
14 (Ab)	Ab	-285	642	Monzogranite	170.0 ± 0.7	-	82.0 ± 14.0	9.8 ± 2.5(47)	157.0 ± 24.0	-
North block of the Napo Uplift										
NL68	KTe	750	1735		68.6 ± 3.5	-	22.1 ± 6.3	11.3 ± 2.5 (35)	-	-
19 (Jm)	JM	-100	1438	Andesite	160.0 ± 15.0	-	78.0 ± 14.0	10.8 ± 2.2 (59)	132.0 ± 28.0	-
22NP03	KN	222	1438		84.0 ± 8.0	-	-	-	-	-
10 (Jm)	JM	-310	1662	Ep-K feldspar rhyolite	160.0 ± 15.0	-	83.0 ± 12.0	9.6 ± 1.3 (25)	139.0 ± 29.0	-
53 (Ab)	Ab	-545	1336	Diorite (Pyr-Chl-Ep)	170.0 ± 0.7	-	160.0 ± 48.0	10.5 ± 2.3 (39)	175.0 ± 38.0	-
NA18	JM	-20	1279		160.0 ± 15.0	-	101.6 ± 7.6	9.3 ± 2.0 (58)	-	-
22NP04	JM	-536	1294		165.0 ± 15.0	172.6 ± 16.6	23.4 ± 6.5	11.7 ± 2.1 (4)	-	-
51 (Jm)	JM	-80	1585	Kfeld-plag-hbl-rhyolite	160.0 ± 15.0	-	116.0 ± 30.0	7 (1)	-	-
22NP06	KN	250	754		-	-	-	-	-	-
22NP09	JM	-160	1735		-	-	-	-	-	3.7 ± 0.4
Central block of the Napo Uplift										

22NP18	KN	230	230		79.0 ± 6.0					
22NP24	KH	100	1200		110.0 ± 7.0	-	-	-	-	-
NL92	JM	-7	1157		160.0 ± 15.0	-	167.7 ± 9.0	13.0 ± 1.8 (120)	-	-
31 (Jm)	JM	-10	1015	Volcanic breccias	160.0 ± 15.0	-	-	-	173.0 ± 26.0	-
29 (Jm)	JM	-10	1015	Ash	160.0 ± 15.0	-	-	-	166.0 ± 22.0	-
33 (Jm)	JM	-10	1015	Massive pumice tuff	160.0 ± 15.0	-	183.0 ± 30.0	11.8 ± 1.8 (59)	173.0 ± 30.0	-
NL99	JM	-50	1021		160.0 ± 15.0	-	220.7 ± 39.2	12.4 ± 2.0 (67)	-	-
22NP21	JM	-20	1030	Andesite	160.0 ± 15.0	183.7 ± 16.3	110.0 ± 12.4	10.6±1.1 (6)	-	11.0 ± 1.1
84 (Jm)	JM	-40	1115	Ignimbrite	160.0 ± 15.0	-	-	-	156.0 ± 20.0	-
22NP19	JM	-160	672	Volcanic breccias	160.0 ± 15.0	285..2 ± 13.5	119.0 ± 16.4	11.4±1.3 (36)	-	22.3 ± 2.2
South block of the Napo Uplift										
NA25	M_CAr	3550	664		14.0±1.0	-	25.6 ± 3.0	11.8±2.2 (32)	-	-
NA75	M_CAr	2550	508		16.5 ± 6.5	-	33.4 ± 1.8	11.7 ± 2.1 (49)	-	-
NJ69	KTe	860	447		68.6 ± 3.5	-	53.7 ± 15.1	12.9 ± 2.4 (18)	-	-
NJ82	KTe	1662	470		68.6 ± 3.5	-	80.0 ± 6.4	14.3 ± 2.4 (109)	-	-
20111MS	KTe	1501	391		68.6 ± 3.5	84.5 ± 17.5	59.6 ± 9.4	13.4 ± 1.6 (42)	-	21.9 ± 2.2
22NP29	KTe	840	399		68.6 ± 3.5	76.6 ± 15.7	39.0 ± 12.3	-	-	-
20109MS	KTe	1137	420		68.6 ± 3.5	90.9 ± 7.7	49.0 ± 8.2	12.8 ± 1.9 (46)	-	7.4 ± 0.7
22NP27	KN	780	508		84.0 ± 12.0	-	-	-	-	-

Appendix C. Supplementary File S2_Zeta-factor

D22D=Apatite Durango

Grain	S1	2s	S2	2s	S3	2s	U/Ca Mean	2s	Zeta	2s
D22D_1	0.005268	7.06E-05	0.00531	7.90E-05	0.005011	7.01E-05	0.005187	4.21E-05	1.035402	0.378169
D22D_2	0.005321	7.21E-05	0.005325	7.72E-05	0.00506	7.09E-05	0.00523	4.23E-05	0.845377	0.303745
D22D_3	0.005375	7.27E-05	0.005411	7.90E-05	0.00515	7.95E-05	0.005316	4.44E-05	0.803088	0.298335
D22D_4	0.005136	7.18E-05	0.004891	7.14E-05	0.005131	7.36E-05	0.005051	4.17E-05	0.705916	0.294445
D22D_5	0.005282	7.37E-05	0.005278	7.71E-05	0.005137	7.70E-05	0.005234	4.38E-05	1.030946	0.461134
D22D_6	0.005321	7.58E-05	0.005308	7.73E-05	0.005209	7.97E-05	0.005281	4.48E-05	0.929172	0.450783
D22D_7	0.005321	7.88E-05	0.005302	7.79E-05	0.005234	7.63E-05	0.005285	4.48E-05	0.948099	0.371962
D22D_8	0.005335	7.68E-05	0.005302	7.65E-05	0.005201	7.60E-05	0.005279	4.41E-05	0.911391	0.380153
D22D_9	0.005335	7.43E-05	0.005267	7.74E-05	0.005235	7.56E-05	0.00528	4.37E-05	0.967593	0.372513
D22D_10	0.005348	7.59E-05	0.005219	7.58E-05	0.005224	7.99E-05	0.005265	4.45E-05	0.85481	0.297694
D22D_11	0.005282	7.80E-05	0.005265	7.78E-05	0.005027	7.39E-05	0.005185	4.42E-05	0.758728	0.286845
D22D_12	0.005295	7.95E-05	0.005239	7.88E-05	0.005076	7.41E-05	0.005197	4.47E-05	0.824646	0.306348
D22D_13	0.005202	7.05E-05	0.004873	7.17E-05	0.00504	7.67E-05	0.00504	4.20E-05	0.672091	0.263676
D22D_14	0.005268	8.12E-05	0.005239	7.64E-05	0.005106	7.49E-05	0.005201	4.47E-05	0.832658	0.33314
D22D_15	0.005255	7.55E-05	0.005249	7.78E-05	0.005074	7.16E-05	0.005187	4.32E-05	0.904659	0.330421
D22D_16	0.005268	7.27E-05	0.005289	7.76E-05	0.005142	7.40E-05	0.005232	4.31E-05	0.761405	0.261235
D22D_17	0.005335	7.90E-05	0.005299	7.84E-05	0.0052	7.88E-05	0.005278	4.55E-05	0.973392	0.374752
D22D_18	0.005321	7.76E-05	0.005299	7.86E-05	0.005237	7.59E-05	0.005285	4.47E-05	0.81698	0.36543
D22D_19	0.005348	8.37E-05	0.005257	7.44E-05	0.005252	7.72E-05	0.005282	4.51E-05	1.047324	0.427662
D22D_20	0.005308	7.80E-05	0.005273	7.63E-05	0.00524	7.97E-05	0.005274	4.50E-05	0.82357	0.351242
D22D_21	0.005321	7.59E-05	0.005495	8.29E-05	0.005144	7.68E-05	0.005311	4.53E-05	0.682811	0.221609
D22D_22	0.005335	7.88E-05	0.005426	8.11E-05	0.005162	7.86E-05	0.005305	4.59E-05	0.937503	0.354436
D22D_23	0.005321	7.95E-05	0.005345	8.12E-05	0.005182	7.76E-05	0.00528	4.58E-05	0.933103	0.352773
D22D_24	0.005308	7.80E-05	0.005098	7.23E-05	0.005168	7.48E-05	0.005186	4.33E-05	1.017838	0.434091
D22D_25	0.005242	8.08E-05	0.005271	8.80E-05	0.005104	7.64E-05	0.005198	4.69E-05	0.704963	0.245519
D22D_26	0.005229	7.75E-05	0.005175	7.58E-05	0.005137	7.30E-05	0.005178	4.35E-05	0.739864	0.270232
D22D_27	0.005215	8.04E-05	0.005295	7.88E-05	0.00517	7.59E-05	0.005225	4.52E-05	1.012509	0.389813
D22D_28	0.005268	7.91E-05	0.00505	7.06E-05	0.005245	7.55E-05	0.005179	4.32E-05	0.91035	0.357149
D22D_29	0.005268	7.75E-05	0.005306	8.73E-05	0.00525	7.87E-05	0.005272	4.67E-05	0.850788	0.340399
D22D_30	0.005268	7.98E-05	0.005381	7.73E-05	0.00523	7.73E-05	0.005294	4.51E-05	0.789262	0.309647
D22D_31	0.005295	7.82E-05	0.005484	8.12E-05	0.005144	7.55E-05	0.005299	4.52E-05	0.775793	0.278751
D22D_32	0.005255	8.15E-05	0.005108	6.85E-05	0.005096	7.79E-05	0.005146	4.35E-05	0.960157	0.384149
D22D_33	0.005242	7.79E-05	0.005408	7.86E-05	0.005147	7.72E-05	0.005264	4.50E-05	0.869565	0.323034
D22D_34	0.005268	7.71E-05	0.005125	6.74E-05	0.005131	7.56E-05	0.00517	4.21E-05	1.038723	0.424141
D22D_35	0.005282	7.82E-05	0.005457	8.06E-05	0.005157	7.57E-05	0.005292	4.51E-05	1.090135	0.412137
D22D_36	0.005242	7.38E-05	0.00513	6.81E-05	0.005172	7.50E-05	0.005179	4.16E-05	1.069941	0.41191
D22D_37	0.005242	8.03E-05	0.005392	7.73E-05	0.005185	7.69E-05	0.005273	4.51E-05	0.908917	0.321445
D22D_38	0.004472	6.54E-05	0.004378	6.29E-05	0.004436	6.53E-05	0.004428	3.72E-05	1.044004	0.401933
D22D_39	0.004419	6.44E-05	0.004543	6.73E-05	0.00444	6.76E-05	0.004466	3.83E-05	0.675622	0.24677
D22D_40	0.004459	6.58E-05	0.004405	6.61E-05	0.004487	6.76E-05	0.00445	3.84E-05	0.676475	0.232102
D22D_41	0.004552	7.07E-05	0.004625	6.99E-05	0.004372	6.54E-05	0.004509	3.96E-05	0.801032	0.278972
D22D_42	0.004499	6.60E-05	0.004409	6.17E-05	0.004344	6.21E-05	0.004414	3.65E-05	0.773824	0.273663
D22D_43	0.004485	6.46E-05	0.004626	6.87E-05	0.004382	6.64E-05	0.004495	3.84E-05	0.824667	0.311774
D22D_44	0.004499	6.26E-05	0.004418	6.38E-05	0.004386	6.50E-05	0.004436	3.68E-05	0.71545	0.245469
D22D_45	0.004499	6.36E-05	0.004557	6.93E-05	0.004364	6.55E-05	0.004471	3.81E-05	0.951092	0.35957
D22D_46	0.004485	6.77E-05	0.00455	7.53E-05	0.004366	6.53E-05	0.004459	3.99E-05	0.784616	0.320395
D22D_47	0.004499	6.97E-05	0.004333	5.84E-05	0.004425	6.63E-05	0.004409	3.71E-05	0.813884	0.355274
D22D_48	0.004485	6.94E-05	0.004596	6.94E-05	0.004413	6.75E-05	0.004497	3.97E-05	1.162081	0.600183
D22D_49	0.004472	6.50E-05	0.004286	6.15E-05	0.004449	6.79E-05	0.004397	3.73E-05	0.630859	0.289508
D22D_50	0.004432	6.16E-05	0.004438	6.93E-05	0.004444	6.83E-05	0.004438	3.82E-05	0.93244	0.43963
D22D_51	0.004459	6.01E-05	0.004386	6.63E-05	0.004339	6.40E-05	0.004397	3.66E-05	0.667776	0.284795
D22D_52	0.004419	6.25E-05	0.004479	6.82E-05	0.004391	6.75E-05	0.004429	3.81E-05	0.783217	0.369274
D22D_53	0.004485	7.01E-05	0.004608	6.85E-05	0.004396	6.50E-05	0.004493	3.91E-05	0.755242	0.290767
D22D_54	0.004565	7.74E-05	0.004342	6.32E-05	0.004396	6.54E-05	0.004419	3.92E-05	0.982557	0.463264

D22D_55	0.004552	7.34E-05	0.004474	6.94E-05	0.004413	6.69E-05	0.004475	4.03E-05	0.846275	0.410574
D22D_56	0.004446	6.34E-05	0.004527	6.92E-05	0.004419	6.69E-05	0.004462	3.83E-05	0.946458	0.371321
D22D_57	0.004326	5.69E-05	0.004266	6.07E-05	0.004397	6.61E-05	0.004326	3.52E-05	0.904178	0.41493
D22D_58	0.004419	6.97E-05	0.004371	6.65E-05	0.004428	6.65E-05	0.004405	3.90E-05	0.615967	0.262706
D22D_59	0.004499	7.29E-05	0.004491	6.95E-05	0.004422	6.81E-05	0.004469	4.05E-05	0.88422	0.416902
D22D_60	0.004339	5.48E-05	0.004372	6.71E-05	0.004445	6.82E-05	0.004378	3.60E-05	0.632455	0.258251
D22D_61	0.004525	7.54E-05	0.004501	7.23E-05	0.004374	6.59E-05	0.004459	4.09E-05	0.748258	0.246121
D22D_62	0.004578	7.44E-05	0.004381	6.67E-05	0.004371	6.44E-05	0.004432	3.93E-05	0.590698	0.199761
D22D_63	0.004366	5.92E-05	0.00433	6.20E-05	0.004339	6.62E-05	0.004346	3.59E-05	0.64706	0.240372
D22D_64	0.004339	5.49E-05	0.004322	6.23E-05	0.004354	6.44E-05	0.004338	3.47E-05	0.575915	0.200561
D22D_65	0.004552	7.78E-05	0.00439	6.64E-05	0.004353	6.46E-05	0.004418	3.98E-05	0.635701	0.265167
D22D_66	0.004353	6.10E-05	0.004488	7.08E-05	0.00441	6.75E-05	0.00441	3.81E-05	0.584755	0.217231
D22D_67	0.004393	7.51E-05	0.004467	7.04E-05	0.004428	6.60E-05	0.004431	4.05E-05	0.55857	0.174543
D22D_68	0.004419	6.91E-05	0.004462	7.02E-05	0.004451	6.87E-05	0.004444	4.00E-05	0.632386	0.220242
D22D_69	0.004353	6.68E-05	0.004418	6.93E-05	0.004469	6.68E-05	0.004413	3.90E-05	0.583267	0.209579
D22D_70	0.004472	7.17E-05	0.004323	6.55E-05	0.004453	6.94E-05	0.004411	3.97E-05	0.705434	0.271596
D22D_71	0.004366	6.06E-05	0.004298	5.98E-05	0.00438	6.59E-05	0.004346	3.58E-05	0.659895	0.281433
D22D_72	0.004472	8.08E-05	0.004342	5.87E-05	0.004307	6.32E-05	0.004358	3.80E-05	0.562529	0.234642
D22D_73	0.004247	3.86E-05	0.004392	6.13E-05	0.004375	6.59E-05	0.004305	2.93E-05	0.506758	0.226655
D22D_74	0.004512	7.23E-05	0.004354	6.28E-05	0.004332	6.52E-05	0.004391	3.84E-05	0.581239	0.183874
D22D_75	0.004339	5.53E-05	0.004392	6.58E-05	0.004429	7.15E-05	0.004379	3.64E-05	0.616122	0.232929
D22D_76	0.004485	7.15E-05	0.004457	6.91E-05	0.0044	6.60E-05	0.004445	3.97E-05	0.609597	0.200508
D22D_77	0.004393	7.58E-05	0.00446	6.86E-05	0.004411	6.43E-05	0.004422	3.99E-05	0.893668	0.433568
D22D_78	0.004286	5.55E-05	0.004443	6.95E-05	0.004421	6.85E-05	0.004368	3.66E-05	0.498483	0.185179
D22D_79	0.004432	7.39E-05	0.004369	6.86E-05	0.004434	6.84E-05	0.004411	4.05E-05	0.757894	0.272332
D22D_80	0.004286	5.69E-05	0.00436	6.60E-05	0.00445	6.80E-05	0.004356	3.64E-05	0.846546	0.309196
D22D_81	0.004631	7.29E-05	0.004522	7.37E-05	0.004327	6.66E-05	0.004483	4.09E-05	0.80232	0.303337
D22D_82	0.004565	8.37E-05	0.004528	7.44E-05	0.004427	6.94E-05	0.004498	4.34E-05	0.861548	0.338029
D22D_83	0.004432	6.04E-05	0.004517	7.51E-05	0.004418	6.85E-05	0.00445	3.88E-05	0.611683	0.203964
D22D_84	0.004326	4.66E-05	0.004531	7.31E-05	0.004385	6.42E-05	0.004385	3.35E-05	0.653358	0.278637
D22D_85	0.004645	7.33E-05	0.004487	6.89E-05	0.004494	7.10E-05	0.004539	4.10E-05	0.629439	0.25184
D22D_86	0.004446	8.19E-05	0.004364	6.60E-05	0.004385	6.66E-05	0.004392	4.07E-05	0.627938	0.267817
D22D_87	0.004406	7.46E-05	0.004373	6.40E-05	0.004404	5.98E-05	0.004394	3.77E-05	0.944139	0.402664
D22D_88	0.004273	4.46E-05	0.004297	6.14E-05	0.004458	6.70E-05	0.004321	3.18E-05	0.535041	0.202265
D22D_89	0.00422	3.46E-05	0.00423	5.93E-05	0.004404	6.67E-05	0.004253	2.73E-05	0.682755	0.24143
D22D_90	0.004406	6.90E-05	0.004239	6.07E-05	0.004452	6.45E-05	0.004359	3.72E-05	0.673971	0.238354
D22D_91	0.004419	6.89E-05	0.004476	7.22E-05	0.004337	6.41E-05	0.004405	3.93E-05	0.718278	0.299611
D22D_92	0.004366	5.81E-05	0.004456	7.19E-05	0.004432	7.12E-05	0.004411	3.82E-05	0.667223	0.266952
D22D_93	0.004393	5.69E-05	0.004397	6.48E-05	0.004456	6.84E-05	0.004412	3.63E-05	0.642468	0.238665
D22D_94	0.004393	6.53E-05	0.004327	6.25E-05	0.004394	6.58E-05	0.00437	3.72E-05	0.583213	0.243267
D22D_95	0.004353	6.77E-05	0.00428	6.25E-05	0.004447	6.77E-05	0.004356	3.80E-05	0.793795	0.331108
D22D_96	0.004326	6.44E-05	0.004256	6.61E-05	0.004474	6.88E-05	0.004348	3.83E-05	0.711341	0.310518
D22D_97	0.004379	6.82E-05	0.004277	6.52E-05	0.004438	6.83E-05	0.004362	3.88E-05	0.489281	0.208676
D22D_98	0.004419	7.47E-05	0.004339	6.55E-05	0.00451	6.46E-05	0.004424	3.92E-05	0.616648	0.241931
D22D_99	0.004353	7.02E-05	0.004427	7.02E-05	0.004548	6.73E-05	0.004446	4.00E-05	0.669404	0.257724
D22D_100	0.004393	7.46E-05	0.004376	6.43E-05	0.004465	6.59E-05	0.004412	3.92E-05	0.712103	0.248003

Appendix D. Supplementary File S4_U-Pb

GeOHeLiS Platform, Universite Rennes 1					Data for Tera-Wasserburg plot					Data for Wetherill plot					Dates						
Identifier	206Pb	Uppm	Th/U	Pb ppm	238U/ 206Pb	2se%	207Pb/ 206Pb	2se%	rho	207Pb/235U	2se%	206Pb/238U	2se%	Rho	207Pb/206Pb	2se (abs)	206Pb/238U	2se (abs)	207Pb/235U	2se (abs)	% conc
A_DG6																					
22DURG01	291	13	24.75	2	151.51	9.8	0.21465	22.5	0.8	0.1709	17.5	0.0066	9.8	0.01	2940	372	42	4	160	26	5.4
22DURG02	289	14	25.15	2	152.75	9.9	0.20513	20.8	0.5	0.1785	18.5	0.00655	9.9	0.01	2867	344	42	4	167	28	5.8
22DURG03	304	15	25.41	2	160.03	6.9	0.1923	16.1	0.22	0.1712	17.9	0.00625	6.9	0.23	2761	267	40	3	160	27	5.8
22DURG04	278	13	24.81	2	151.07	8.9	0.24943	17.6	0.01	0.2246	14.1	0.00662	8.9	0.13	3180	282	43	4	206	26	6.5
22DURG05	279	14	24.83	2	160.21	9.1	0.18084	20.1	0.17	0.1606	20.4	0.00624	9.1	0.17	2660	340	40	4	151	29	5.7
22DURG06	327	15	25.13	2	145.31	8.7	0.20625	18.5	0.41	0.1834	16.5	0.00688	8.7	0.02	2876	306	44	4	171	26	5.9
22DURG07	290	13	24.99	2	161.45	9	0.2292	19.7	0.4	0.168	18	0.00619	9	0.11	3046	321	40	4	158	26	5.2
22DURG08	330	13	25.44	2	145.46	8.5	0.18888	24.5	0.67	0.1684	19.9	0.00687	8.5	-0.25	2732	413	44	4	158	29	5.8
22DURG09	294	13	25.31	2	158.37	10	0.20965	16.2	0.36	0.1653	15.4	0.00631	10	0.22	2902	266	41	4	155	22	5.4
22DURG10	309	14	24.82	2	147.9	9.8	0.18067	20.1	0.82	0.1561	15.5	0.00676	9.8	0.09	2658	339	43	4	147	21	5.5
22DURG11	303	15	24.73	2	156.59	8.3	0.21713	12.4	0.53	0.1879	13.1	0.00639	8.3	0.12	2959	202	41	3	175	21	5.9
22DURG12	314	16	24.14	2	155.98	8.5	0.27886	21.5	0.54	0.2322	17.8	0.00641	8.5	0.06	3356	343	41	3	212	34	6.3
22DURG13	270	13	24.94	2	170.28	10	0.21561	21	0.7	0.161	17.7	0.00587	10	0.04	2947	346	38	4	152	25	5.1
22DURG14	301	12	24.24	1	150.97	8.2	0.21011	21.5	0.66	0.1649	17.2	0.00662	8.2	-0.25	2906	356	43	3	155	25	5.3
22DURG15	294	12	24.27	2	151.29	7.5	0.20107	19.1	0.56	0.1785	17.1	0.00661	7.5	-0.2	2834	317	42	3	167	26	5.9
22DURG16	292	12	24.48	1	145.74	7.7	0.226	18.3	0.68	0.2002	16	0.00686	7.7	-0.04	3023	298	44	3	185	27	6.1
22DURG17	265	12	24.71	1	167.57	9	0.19545	21	0.31	0.1563	19.2	0.00597	9	0.06	2788	350	38	3	147	26	5.3
22DURG18	319	12	24.88	1	140.26	8.7	0.22615	21.9	0.86	0.1893	14.4	0.00713	8.7	0	3024	358	46	4	176	23	5.8
A_MAD																					
MAD	5998	22	36.13	51	13	3.6	0.0572	0	0.24	0.6066	3.6	0.07692	3.6	1	498	0	478	16	481	14	99.2
MAD	5862	22	35.84	51	13.28	3.3	0.0572	0	-0.01	0.5939	3.3	0.07531	3.3	1	498	0	468	15	473	13	98.9
MAD	5903	22	35.74	51	12.98	3.8	0.0572	0	0.09	0.6077	3.8	0.07705	3.8	1	498	0	479	18	482	15	99.3
MAD	5948	22	36.4	51	12.9	3.7	0.0572	0	0.04	0.6115	3.7	0.07754	3.7	1	498	0	481	17	484	14	99.4
MAD	5928	22	35.93	52	13.29	3.7	0.0572	0	0.07	0.5934	3.7	0.07525	3.7	1	498	0	468	17	473	14	98.9
MAD	5737	22	35.42	51	13.39	3.9	0.0572	0	-0.02	0.589	3.9	0.07469	3.9	1	498	0	464	18	470	15	98.7
MAD	5837	22	36.15	51	12.97	4	0.0572	0	0.01	0.6078	4	0.07708	4	1	498	0	479	19	482	15	99.3
MAD	5781	22	35.61	51	13.21	3.7	0.0572	0	0.04	0.5968	3.7	0.07568	3.7	1	498	0	470	17	475	14	99
MAD	5963	22	36.18	51	13.02	3.5	0.0572	0	-0.02	0.6057	3.5	0.0768	3.5	1	498	0	477	16	481	13	99.2
MAD	5950	22	35.95	51	13.16	3.5	0.0572	0	0	0.5991	3.5	0.07597	3.5	1	498	0	472	16	477	13	99
MAD	5871	22	35.55	51	13.16	3.7	0.0572	0	-0.05	0.5991	3.7	0.07597	3.7	1	498	0	472	17	477	14	99

MAD	5825	22	35.61	51	12.98	3.6	0.0572	0	0.08	0.6078	3.6	0.07707	3.6	1	498	0	479	17	482	14	99.3
MAD	5677	22	36.42	51	13.2	3.6	0.0572	0	0.08	0.5974	3.6	0.07575	3.6	1	498	0	471	16	476	14	99
MAD	6087	22	35.38	52	12.77	3.6	0.0572	0	0.03	0.6177	3.6	0.07833	3.6	1	498	0	486	17	488	14	99.5
MAD	6010	22	36.11	51	13.06	3.6	0.0572	0	-0.01	0.6039	3.6	0.07658	3.6	1	498	0	476	17	480	14	99.2
MAD	6005	22	36.29	51	12.95	3.2	0.0572	0	0.1	0.609	3.2	0.07723	3.2	1	498	0	480	15	483	12	99.3
MAD	5880	22	35.87	51	13.56	3.5	0.0572	0	0.09	0.5815	3.5	0.07373	3.5	1	498	0	459	15	465	13	98.5
MAD	6006	22	35.72	51	13.16	3.5	0.0572	0	0.05	0.5992	3.5	0.07598	3.5	1	498	0	472	16	477	13	99
A_McClure																					
MCCLURE	2771	7	3.91	4	8.17	4.8	0.30395	6.7	0.3	5.0936	7.1	0.12239	4.8	0.31	3490	104	744	34	1835	60	52.6
MCCLURE	10174	33	4.22	12	10.84	3.9	0.12677	4.6	0.13	1.6054	5.6	0.09229	3.9	0.34	2053	82	569	21	972	35	47.4
MCCLURE	6843	20	3.84	8	10.11	3.5	0.16036	4.3	0.2	2.1732	5	0.09891	3.5	0.3	2459	72	608	20	1173	35	47.7
MCCLURE	7936	25	3.99	11	10.49	4.1	0.15539	6.4	0.16	1.9803	5.4	0.09534	4.1	0.14	2405	109	587	23	1109	36	46.1
MCCLURE	5540	15	4.99	8	9.58	4.1	0.22455	5.4	0.32	3.2191	5.9	0.10438	4.1	0.33	3013	87	640	25	1462	46	48.5
MCCLURE	5196	11	4.17	8	7.46	4.3	0.33871	5.6	0.36	6.251	5.3	0.134	4.3	0.13	3656	85	811	33	2012	46	55
MCCLURE	6400	20	5.33	10	10.44	3.6	0.15921	4.9	0.02	2.0632	5.2	0.09582	3.6	0.48	2447	83	590	20	1137	35	46.5
MCCLURE	11021	34	3.24	14	10.19	4.1	0.17915	5.7	0.33	2.3636	5	0.09815	4.1	0.3	2644	95	604	23	1232	36	46.6
MCCLURE	4302	10	4.65	6	8.14	3.8	0.22667	7.9	0.27	3.7452	7.4	0.1228	3.8	0.05	3028	126	747	27	1581	59	52.2
MCCLURE	6548	18	4.1	8	9.68	3.8	0.17316	3.6	0.07	2.4377	4.8	0.10328	3.8	0.56	2588	60	634	23	1254	35	48.5
MCCLURE	3002	7	3.33	4	8.05	4.3	0.33006	5.5	-0.05	5.6021	7.1	0.12422	4.3	0.62	3617	84	755	31	1916	61	53
G_NIST612																					
NIST612	26801	27	1.44	59	3.51	2.9	0.90164	1.2	0.67	35.3468	2.9	0.28452	2.9	0.47	5091	17	1614	42	3648	29	71.7
NIST612	26824	27	1.44	58	3.51	3	0.89102	1.2	0.64	35.0887	2.9	0.28503	3	0.55	5074	17	1617	42	3641	29	71.8
NIST612	26723	27	1.45	60	3.55	2.9	0.90828	1.1	0.6	35.2719	2.9	0.28199	2.9	0.48	5101	16	1601	41	3646	28	71.5
NIST612	25909	28	1.45	64	3.53	2.9	0.90081	1.4	0.66	35.1661	3	0.28311	2.9	0.4	5090	19	1607	42	3643	29	71.6
NIST612	25798	28	1.44	64	3.53	2.9	0.90239	1.3	0.59	35.1975	2.9	0.28294	2.9	0.55	5092	18	1606	42	3644	29	71.6
NIST612	25824	28	1.42	63	3.52	3	0.89808	1.2	0.5	35.0024	3.2	0.28371	3	0.6	5085	17	1610	43	3639	31	71.6
NIST612	26104	29	1.42	69	3.52	2.9	0.89686	1.1	0.52	35.1575	2.9	0.28422	2.9	0.65	5083	15	1613	41	3643	28	71.7
NIST612	25754	28	1.42	67	3.57	3	0.90345	1.4	0.6	34.8807	3	0.28002	3	0.55	5094	19	1591	42	3635	29	71.4
NIST612	25562	28	1.43	65	3.57	3	0.90955	1.2	0.65	35.0358	2.9	0.27991	3	0.64	5103	17	1591	43	3640	29	71.3
NIST612	26212	25	1.41	62	3.57	2.9	0.91611	1.1	0.48	35.2604	2.9	0.27994	2.9	0.73	5113	16	1591	41	3646	29	71.3
NIST612	27108	26	1.4	64	3.59	3	0.9052	1.3	0.56	34.8172	3	0.27887	3	0.79	5096	18	1586	43	3633	30	71.3
NIST612	25863	25	1.4	62	3.58	2.9	0.91199	1.3	0.57	35.1568	3	0.27925	2.9	0.69	5107	19	1588	41	3643	29	71.3
NIST612	26241	33	1.4	104	3.57	3	0.91211	1.5	0.77	35.278	2.8	0.28011	3	0.12	5107	21	1592	42	3646	28	71.4
NIST612	26379	32	1.4	96	3.54	3	0.8965	1.2	0.71	34.8482	2.9	0.28236	3	0.69	5083	17	1603	43	3634	29	71.5
NIST612	25912	31	1.42	88	3.57	3	0.90037	1.4	0.67	34.819	2.9	0.28029	3	0.58	5089	20	1593	42	3634	29	71.4
NIST612	26543	29	1.42	62	3.51	2.9	0.90155	1.2	0.71	35.4275	2.9	0.28491	2.9	0.52	5091	17	1616	42	3651	29	71.7
NIST612	25799	28	1.39	59	3.56	3.2	0.90374	1.2	0.76	34.9115	2.9	0.28064	3.2	0.7	5094	16	1595	45	3636	29	71.4
NIST612	25550	28	1.42	60	3.57	3.2	0.90998	1.4	0.75	35.1067	3.1	0.2804	3.2	0.24	5104	19	1593	45	3642	31	71.4
NIST612	25572	25	1.4	54	3.54	2.9	0.9033	1.1	0.53	35.1495	2.9	0.28213	2.9	0.77	5093	16	1602	42	3643	29	71.5
NIST612	25508	25	1.41	52	3.52	2.9	0.90134	1.3	0.51	35.2505	2.9	0.2837	2.9	0.66	5090	18	1610	42	3646	29	71.6
20111MS																					
20111MS_G4	3527	11	3.89	16	8.33	4.8	0.75172	3.4	0.61	12.4043	4.5	0.12007	4.8	0.93	4832	48	731	33	2636	43	54.5
20111MS_G5	2240	13	3.79	9	15.91	5.1	0.66457	4.2	0.4	5.8876	6.6	0.06286	5.1	0.86	4655	61	393	19	1959	57	42.1

20111MS_G6	3301	15	3.68	13	12.54	6.7	0.68837	11.9	0.52	7.5149	10.6	0.07974	6.7	0.07	4706	172	495	32	2175	95	46.2
20111MS_G7	2920	11	4.92	12	10.11	6.9	0.74337	3.5	0.23	9.7838	6	0.09891	6.9	0.92	4816	50	608	40	2415	55	50.1
20111MS_G8	2907	7	3.72	6	8.92	4.5	0.73803	4.1	0.57	11.2204	4.3	0.11214	4.5	0.78	4806	59	685	29	2542	40	52.9
20111MS_G9	2243	5	5.03	5	7.28	4.4	0.76569	4.1	0.54	14.4689	4.6	0.13738	4.4	0.46	4859	58	830	34	2781	44	57.2
20111MS_G10	2245	3	2.77	5	5.23	5.7	0.77585	4.4	0.62	20.0567	5.1	0.19119	5.7	0.77	4877	62	1128	59	3094	49	63.4
20111MS_G11	2688	7	3.97	6	9.75	4.1	0.73584	4.5	0.4	10.3795	5.1	0.10253	4.1	0.55	4802	65	629	25	2469	48	51.4
20111MS_G12	1863	5	4.06	4	9.45	5.9	0.75123	6	0.72	10.9391	5.7	0.10585	5.9	0.18	4831	86	649	37	2518	53	52.1
20111MS_G13	3062	11	5.01	7	12.87	3.7	0.71954	3.3	0.44	7.7308	4.2	0.0777	3.7	0.81	4770	47	482	17	2200	37	46.1
20111MS_G14	2950	11	2.75	6	12.42	4.3	0.68	4.1	0.76	7.5416	3.8	0.08049	4.3	0.44	4688	59	499	21	2178	34	46.5
20111MS_G15	2291	4	3.09	5	6.18	5.3	0.7475	6.1	0.53	16.5169	5.9	0.16188	5.3	0.28	4824	87	967	47	2907	57	60.3
20111MS_G16	2289	8	5.04	5	11.18	4.8	0.72282	4.5	0.3	8.8302	5.8	0.08941	4.8	0.76	4776	64	552	25	2321	53	48.6
20111MS_G17	3262	12	4.8	7	11.93	4.1	0.73359	3.7	0.38	8.3172	4.2	0.0838	4.1	0.77	4797	53	519	20	2266	38	47.2
20111MS_G18	4204	4	5.52	8	3.08	14.2	0.8279	6	0.05	38.9703	16.8	0.32447	14.2	0.34	4970	85	1812	225	3745	167	75.4
20111MS_G21	2339	9	5.93	5	12.99	5.4	0.73115	4.5	0.26	7.6246	6	0.077	5.4	0.76	4793	64	478	25	2188	54	45.6
20111MS_G22	2497	11	4.05	5	14.26	5.5	0.67006	4.3	0.19	6.4593	6.4	0.07012	5.5	0.73	4667	63	437	23	2040	56	43.7
20111MS_G25	2886	8	4.57	6	8.63	4.6	0.72142	4.1	0.39	11.3917	4.7	0.11591	4.6	0.7	4773	59	707	31	2556	44	53.5
20111MS_G27	5465	20	5.9	12	11.88	6.8	0.70898	2.7	0.05	8.2185	7.8	0.08419	6.8	0.98	4748	39	521	34	2255	71	47.5
20111MS_G28	1884	6	4.52	4	10.47	7.4	0.73223	3.8	0.35	9.4681	6.5	0.09551	7.4	0.93	4795	55	588	42	2384	60	49.7
22NP19																					
22NP19_G4	1980	2	4.16	6	3.45	8.1	0.73073	4.3	0.3	29.2924	8.7	0.28971	8.1	0.91	4792	62	1640	118	3463	86	72.3
22NP19_G5	3354	5	3.32	9	4.64	6.3	0.65188	3.6	0.32	19.2957	6.6	0.2155	6.3	0.98	4627	52	1258	72	3057	64	66.1
22NP19_G6	1894	2	3.53	6	3.75	6.1	0.7128	4.8	0.24	26.8973	9.1	0.26665	6.1	0.93	4756	69	1524	83	3380	89	71.1
22NP19_G7	5752	7	3.5	17	3.24	14.9	0.71418	3.2	-0.35	31.6191	16.5	0.30867	14.9	0.98	4759	46	1734	227	3539	164	74.4
22NP19_G8	3827	5	3.94	11	4.17	5.8	0.70615	3.2	-0.11	23.345	7.1	0.23962	5.8	0.94	4743	46	1385	72	3241	70	68.3
22NP19_G9	3042	3	3.3	9	2.79	7.4	0.73517	4.4	0.31	36.8249	9.2	0.35907	7.4	0.95	4800	64	1978	126	3689	92	76.8
22NP19_G10	4166	6	3.56	12	4.37	8.2	0.69399	3.6	0.51	20.9542	5.6	0.22889	8.2	0.71	4718	52	1329	99	3136	55	66.5
22NP19_G11	3637	3	2.87	11	2.7	7.4	0.7245	3.7	-0.13	38.8643	11.6	0.37036	7.4	0.99	4779	53	2031	128	3742	115	78.3
22NP19_G12	4474	14	2.99	11	9.5	5.4	0.52554	5.2	0.24	7.5769	6.5	0.10521	5.4	0.55	4314	76	645	33	2182	59	50.6
22NP19_G13	5388	10	3.33	14	5.58	5.8	0.63543	2.9	0.44	15.229	4.4	0.17924	5.8	0.79	4591	42	1063	57	2830	41	61.6
22NP19_G14	5180	6	3.41	15	3.52	6.1	0.72984	5.7	0.5	28.7208	6	0.28426	6.1	0.44	4790	82	1613	88	3444	59	71.9
22NP19_G15	3467	4	3.54	9	3.85	7.7	0.70714	3.6	0.33	24.9523	7.5	0.25944	7.7	0.97	4745	51	1487	102	3306	74	69.7
22NP19_G16	3873	6	3.55	11	4.17	10.6	0.69098	3.6	0.09	22.2601	8.9	0.23952	10.6	0.94	4711	52	1384	132	3195	87	67.8
22NP19_G20	4393	6	3.98	12	4.07	7.4	0.70541	3.2	-0.08	24.2006	9.1	0.24597	7.4	0.97	4741	47	1418	95	3277	89	69.1
22NP19_G21	4904	6	3.43	13	3.79	10.1	0.68409	3.6	-0.27	24.4325	10.4	0.26374	10.1	0.97	4697	52	1509	135	3286	102	70
22NP19_G22	9340	43	3.8	15	14.37	3.7	0.31757	4.3	0.29	3.0406	5.1	0.0696	3.7	0.34	3557	66	434	16	1418	39	39.9
22NP19_G24	3799	8	4.47	9	6.21	5.7	0.63881	3.9	-0.06	14.0551	7	0.16101	5.7	0.97	4598	56	962	51	2753	67	59.9
22NP19_G25	3984	6	4.28	8	5.77	8.8	0.64991	3.8	-0.04	15.5999	10.6	0.1732	8.8	0.98	4623	55	1030	84	2853	102	61.7
22NP19_G26	3108	4	4.45	6	5.06	6.2	0.68179	3.3	0.14	18.4654	6.1	0.19763	6.2	0.81	4692	48	1163	66	3014	59	64.2
22NP19_G27	3489	5	3.78	7	5.11	4.8	0.66018	3.7	0	18.2361	7.3	0.19564	4.8	0.34	4646	53	1152	50	3002	70	64.6
22NP19_G29	4407	6	3.55	9	5.09	7.3	0.65875	3.9	-0.02	18.6413	11.1	0.19635	7.3	0.95	4643	57	1156	78	3023	107	65.1

22NP19_G32	4112	5	3.44	7	4.31	13.4	0.67661	3.4	-0.12	21.0431	13.3	0.23222	13.4	0.97	4681	48	1346	163	3141	130	67.1
22NP21																					
22NP21_G4	4867	10	5.97	11	6.39	5	0.70462	3.1	0.26	15.0397	5.1	0.15653	5	0.8	4740	44	937	43	2818	49	59.5
22NP21_G6	3722	6	5.09	8	5.46	4.3	0.71601	3.6	0.67	17.9553	4	0.18319	4.3	0.44	4763	52	1084	43	2987	38	62.7
22NP21_G7	8763	14	6.02	21	4.93	6.9	0.73894	2.4	-0.11	21.0249	7.9	0.20295	6.9	0.95	4808	34	1191	75	3140	77	65.3
22NP21_G8	3307	3	4.41	8	3.03	5.3	0.78725	3.3	0.28	35.5983	5.4	0.33037	5.3	0.77	4898	48	1840	85	3655	53	74.6
22NP21_G10	4804	3	4.72	12	1.74	4.5	0.8072	2.8	0.36	64.4677	4.8	0.57464	4.5	0.72	4934	40	2927	105	4246	48	86.1
22NP21_G14	4532	13	7.03	11	8.71	4.1	0.64915	3.2	0.54	10.258	3.9	0.11483	4.1	0.5	4621	46	701	27	2458	37	53.2
22NP21_G16	3529	3	4.61	9	2.85	4.6	0.77586	4.1	0.6	37.6132	4.7	0.35057	4.6	0.51	4877	59	1937	76	3710	46	76.1
22NP21_G17	5250	10	6.32	13	5.43	8.1	0.7273	3.9	-0.41	18.7078	10.4	0.18415	8.1	0.93	4785	56	1090	81	3027	101	63.3
22NP21_G18	3902	5	4.77	9	3.49	5.8	0.78312	3.4	0.29	30.3681	5.8	0.28642	5.8	0.79	4891	49	1624	83	3499	57	71.5
22NP21_G19	4232	8	4.96	10	5.94	5	0.71418	3	0.26	16.4891	5.2	0.16837	5	0.77	4759	43	1003	47	2906	50	61.1
22NP21_G21	4516	13	4.91	10	8.77	9.2	0.64345	7.4	0.32	10.0612	10.7	0.11397	9.2	0.72	4609	108	696	61	2440	99	53
22NP21_G22	4803	12	6.57	11	7.77	5.3	0.66054	3.1	0.06	11.7863	6.2	0.12873	5.3	0.79	4647	45	781	39	2588	58	55.7
22NP21_G23	4636	5	5.16	11	3.45	9.9	0.7765	3.4	-0.17	31.2352	11.1	0.28977	9.9	0.97	4879	49	1640	144	3526	110	72.3
22NP21_G24	5323	9	5.77	12	5.17	7.7	0.71563	2.8	-0.09	19.1614	8.6	0.19334	7.7	0.94	4762	40	1139	81	3050	83	64.1
22NP21_G25	4343	3	6.03	11	2.37	10.7	0.803	3.2	0.03	45.5383	11	0.4215	10.7	0.97	4926	46	2267	205	3899	109	79.2
22NP21_G26	3338	3	4.79	7	3.4	4.8	0.7686	3.3	0.47	31.1498	4.9	0.294	4.8	0.69	4864	48	1661	71	3524	48	72.4
22NP21_G28	3648	4	5.43	8	4.05	4.1	0.74366	3.2	0.5	25.2758	4.2	0.2468	4.1	0.53	4817	46	1422	53	3319	41	68.9
22NP21_G32	15914	4	4.96	35	0.86	6.1	0.82345	1.6	0.26	131.7187	6.2	1.15872	6.1	0.85	4962	23	4961	211	4963	62	100
22NP29																					
22NP29_G10	1356	6	5.5	3	16.75	5.7	0.6424	6.7	0.7	5.248	5.8	0.05971	5.7	0.24	4606	97	374	21	1860	50	40.4
22NP29_G14	9479	35	5.02	30	10.86	3.6	0.73133	2.2	0.47	9.3195	3.8	0.09207	3.6	0.83	4793	31	568	20	2370	35	49.4
22NP29_G16	7025	7	139.34	40	2.61	17.4	0.78319	3.4	0.08	39.8795	16.3	0.3827	17.4	0.98	4891	49	2089	311	3768	163	77
22NP29_G18	6085	7	3.12	23	3.31	9.7	0.79524	2.6	0.24	32.8239	9.5	0.30232	9.7	0.97	4913	37	1703	146	3575	94	72.8
22NP29_G23	5453	3	4.83	31	1.67	24.3	0.79807	3.7	0.1	66.9386	25.4	0.60024	24.3	0.99	4918	53	3031	588	4283	260	87.1
22NP29_G28	5280	16	5.69	26	7.92	3.7	0.75185	2.8	0.59	12.992	3.7	0.12619	3.7	0.35	4832	41	766	27	2679	35	55.4
22NP29_G31	5967	18	4.03	27	8.48	7	0.75268	4	-0.02	12.5798	9.6	0.1179	7	0.94	4834	57	718	48	2649	91	54.8
22NP29-BG02	2142	6	2.95	7	7.62	3.9	0.76224	4	0.64	13.6093	3.7	0.13126	3.9	0.37	4852	57	795	29	2723	35	56.1
22NP29-BG03	4081	21	4.91	12	12.15	8.3	0.68184	5.9	0.13	7.7147	9.9	0.08229	8.3	0.79	4692	86	510	41	2198	89	46.8
22NP29-BG04	2804	7	4.27	10	5.72	9.9	0.80815	9.5	0.61	19.1995	9.1	0.17475	9.9	0.5	4936	135	1038	95	3052	89	61.8
22NP29-BG05	1522	4	2.72	6	6.52	5.7	0.81369	6.7	0.66	16.8698	5.4	0.15343	5.7	0.19	4945	96	920	49	2927	52	59.2
22NP29-BG08	1747	20	6.39	7	22.1	5.3	0.61433	5.2	0.42	3.8016	6.6	0.04524	5.3	0.73	4542	75	285	15	1593	53	35.1
22NP29-BG09	2038	11	5.82	9	10.01	8.5	0.71714	4.9	0.07	9.4854	9.2	0.09987	8.5	0.94	4765	70	614	50	2386	85	50.1
22NP29-BG10	1611	5	4.77	8	5.77	4.7	0.78125	5.2	0.73	18.5562	4.6	0.17319	4.7	0.33	4887	74	1030	45	3019	44	61.8
22NP29-BG11	1619	10	4.71	7	12.12	4.6	0.71772	6.2	0.61	8.0369	5.2	0.08249	4.6	0.08	4766	89	511	23	2235	47	46.9
22NP29-BG12	1776	8	6.98	9	8.82	4	0.73395	4.2	0.72	11.4924	3.8	0.11337	4	0.08	4798	60	692	26	2564	35	53.4
22NP25																					

22NP25_G4	3559	3	3.47	9	2.48	7.5	0.79697	3.4	0.34	44.003	7.4	0.40265	7.5	0.88	4916	49	2181	139	3865	74	78.6
22NP25_G5	3712	5	3.61	9	4.54	5.5	0.76036	3	0.48	23.0879	5.3	0.22023	5.5	0.73	4849	44	1283	64	3231	52	66.6
22NP25_G6	4146	6	4.05	10	5.33	4.4	0.74498	3.5	0.6	19.2236	4.6	0.18765	4.4	0.23	4819	50	1109	44	3053	44	63.4
22NP25_G7	2741	5	3.54	7	6.87	6.8	0.71911	4.2	0.08	14.3199	7.6	0.14552	6.8	0.85	4769	60	876	55	2771	73	58.1
22NP25_G8	5776	13	3.11	13	8.17	6.8	0.6462	3.6	-0.26	11.207	9.2	0.12235	6.8	0.92	4615	52	744	48	2540	86	55.1
22NP25_G9	3658	5	3.64	10	4.72	5.8	0.76206	3.8	0.23	22.1575	6.4	0.21203	5.8	0.73	4852	54	1240	65	3191	62	65.8
22NP25_G10	3460	7	3.38	9	6.86	6.4	0.68223	4.6	0.38	13.6135	7	0.14578	6.4	0.71	4693	67	877	53	2723	66	58
22NP25_G11	5023	5	3.25	14	3.31	6.5	0.78159	2.9	0.12	32.99	7.2	0.30231	6.5	0.89	4888	41	1703	97	3580	71	73.2
22NP25_G12	2915	4	3.35	8	4.67	5.1	0.73844	3.5	0.63	21.6612	4.6	0.21411	5.1	0.49	4807	50	1251	57	3169	45	65.9
22NP25_G13	5238	9	4.01	15	5.99	5.8	0.73497	3	0.09	16.9926	6.5	0.16707	5.8	0.88	4800	42	996	54	2934	62	61.1
22NP25_G14	3733	3	3.57	11	3.34	4.6	0.79237	2.9	0.54	32.5082	4.5	0.29945	4.6	0.63	4907	41	1689	69	3566	44	72.7
22NP25_G15	2765	3	3.52	7	4.09	5	0.78568	5.1	0.48	26.2106	5.7	0.24434	5	0.42	4895	73	1409	63	3354	55	68.5
22NP25_G16	4325	4	3.54	12	3.13	11.2	0.79442	7	0.4	34.4266	10.3	0.31898	11.2	0.68	4911	100	1785	174	3622	102	73.8
22NP25_G18	2869	5	3.45	8	5.96	5.2	0.7498	5.6	0.78	17.2748	5	0.16768	5.2	-0.09	4829	81	999	48	2950	48	61.1
22NP25_G19	3741	6	3.69	11	5.86	4.5	0.71741	3.4	0.57	16.8392	4.7	0.17078	4.5	0.37	4765	49	1016	43	2926	45	61.4
22NP25_G20	3898	2	2.94	11	2.14	7.3	0.81592	4.8	0.33	52.4105	8.3	0.46822	7.3	0.78	4949	68	2476	151	4039	83	81.6
22NP25_G22	3876	3	3.53	11	2.9	6	0.78379	3.2	0.42	37.0984	6	0.34441	6	0.74	4892	46	1908	100	3696	60	75.6
22NP25_G23	3301	6	3.61	9	7.1	5.3	0.69839	3.8	0.35	13.5345	6.1	0.14086	5.3	0.79	4727	54	850	42	2718	58	57.5
22NP25_G26	4187	5	3.4	8	4.66	7.8	0.72822	6.5	0.11	21.5083	10.1	0.21442	7.8	0.76	4787	94	1252	89	3162	98	66.1
22NP25_G27	4157	4	2.93	8	3.79	5	0.76217	3.6	0.43	27.4617	5.3	0.26353	5	0.52	4852	51	1508	67	3400	52	70.1
22NP25_G28	2931	3	3.16	6	4.34	4.6	0.74732	3.3	0.09	23.8047	5.2	0.2306	4.6	0.04	4824	48	1338	56	3260	51	67.6
22NP04																					
22NP04_G4	7649	5	4.82	11	2.45	9.9	0.80736	2.3	-0.11	45.5464	10.2	0.40793	9.9	0.98	4934	33	2205	185	3900	102	79
22NP04_G5	3665	5	4.57	5	5.2	4.9	0.72795	3.5	0.57	19.2374	5	0.19224	4.9	0.39	4786	50	1134	51	3054	48	63.8
22NP04_G6	3382	5	4.97	5	5.62	4.8	0.72495	3.2	0.83	17.7411	4.1	0.17802	4.8	0.15	4780	46	1056	47	2976	40	62.3
22NP04_G8	3107	5	4.4	4	6.34	8.4	0.68781	4.2	0.23	14.2735	7.1	0.15771	8.4	0.95	4705	61	944	74	2768	67	58.8
22NP04_G9	3617	6	4.69	5	6.61	7.1	0.72155	4	0.23	15.2207	7.8	0.15123	7.1	0.82	4774	58	908	60	2829	74	59.3
22NP04_G10	4644	5	4.99	6	3.7	7	0.77547	2.9	0.13	29.0042	7.7	0.27042	7	0.9	4877	41	1543	96	3454	76	70.8
22NP04_G11	3767	6	4.93	5	5.82	4.5	0.72504	3.7	0.57	17.0117	4.8	0.17174	4.5	0.25	4781	53	1022	43	2935	46	61.4
22NP04_G13	2469	4	4.95	3	5.91	5	0.7295	3.6	0.46	16.963	5.1	0.16933	5	0.64	4789	52	1008	47	2933	49	61.2
22NP04_G14	4706	15	4.51	6	11.71	4.4	0.6148	3.1	0.58	7.2065	4.5	0.08539	4.4	0.47	4543	45	528	22	2137	40	47
22NP04_G15	2460	6	4.45	3	9.8	4.7	0.62211	4.1	0.63	8.5859	4.7	0.10203	4.7	0.11	4560	60	626	28	2295	43	50.3
22NP04_G16	3808	6	4.89	5	6.04	4.7	0.6915	3.6	0.65	15.7113	4.5	0.16557	4.7	0.33	4713	51	988	43	2859	43	60.7
22NP04_G17	3776	6	5.05	6	5.85	5.1	0.71898	3.7	0.53	16.7934	5	0.17094	5.1	0.64	4768	53	1017	48	2923	48	61.3
22NP04_G18	4220	5	4.94	7	4.06	5.1	0.74587	3.3	0.63	25.0263	4.6	0.2461	5.1	0.58	4821	47	1418	65	3309	45	68.6
22NP04_G20	3664	6	4.67	5	6.64	6.1	0.68194	6.9	0.54	14.0707	6.7	0.15064	6.1	0.22	4692	100	905	52	2754	64	58.7
22NP04_G21	3905	7	5.13	6	6.29	4.9	0.69591	3.5	0.31	15.1566	5.4	0.15888	4.9	0.55	4722	51	951	43	2825	51	59.8
22NP04_G22	5155	6	5.31	8	4.69	4.9	0.74536	3.3	0.38	21.9845	5.3	0.21316	4.9	0.64	4820	47	1246	56	3183	52	66
22NP04_G23	3639	6	4.77	6	6.29	4.5	0.71156	3.5	0.59	15.5596	4.7	0.15887	4.5	0.34	4754	50	950	40	2850	45	60
22NP04_G24	4479	5	5	7	4.39	4.8	0.75262	3.2	0.39	23.4895	5	0.22799	4.8	0.84	4834	46	1324	58	3247	48	67.2
22NP04_G25	4836	5	4.53	8	3.98	6.6	0.77082	2.8	0.27	26.5036	6.6	0.25098	6.6	0.88	4868	40	1444	86	3365	65	69.1
22NP04_G26	6605	7	4.51	11	4.06	6.3	0.77204	3.1	0.53	25.8815	6.3	0.24614	6.3	0.1	4870	44	1419	80	3342	62	68.6
22NP04_G27	3483	6	4.67	5	6.08	4.8	0.70817	3.6	0.61	15.7559	4.5	0.16436	4.8	0.34	4747	51	981	44	2862	43	60.3
22NP04_G28	3175	6	4.6	5	6.89	4.7	0.69126	3.6	0.68	13.8564	4.6	0.14517	4.7	0.34	4712	52	874	39	2740	44	58.1
22NP04_G31	3253	6	4.88	5	6.97	5.3	0.71376	3.1	0.47	13.989	5.2	0.14348	5.3	0.56	4758	44	864	43	2749	49	57.8

22NP20																					
22NP20A_G5	4393	3	7.93	8	0.2	19.3	0.80293	4	-0.36	538.4016	18.4	4.98987	19.3	0.97	4926	57	11540	1043	6387	188	129.7
22NP20A_G13	48585	22	0.64	95	1.73	4.1	0.80534	1.1	0.53	64.2708	4	0.57734	4.1	0.76	4931	15	2938	96	4243	40	86.1
22NP20A_G19	46612	148	1.57	28	11.87	4	0.18439	2.2	0.26	2.1337	4.2	0.08422	4	0.33	2692	37	521	20	1160	29	43.1
22NP20B_G4	15039	29	0.18	23	7.2	4.4	0.68259	2.1	0.26	12.9503	4.4	0.13884	4.4	0.72	4694	30	838	35	2676	42	57
22NP20B_G6	17252	13	0.14	30	2.78	4.5	0.77851	2	0.21	39.3082	5.4	0.36008	4.5	0.81	4882	28	1983	76	3753	53	76.9
22NP20B_G7	8824	3	0.81	16	1	17.2	0.80961	2.2	0.01	111.2236	17.7	0.9962	17.2	1	4938	32	4456	554	4793	180	97.1
22NP20B_G12	15271	19	0.14	23	4.82	4.2	0.71455	3.3	0.55	20.3895	4.5	0.20752	4.2	0.19	4760	47	1216	46	3110	44	65.3
22NP20B_G14	26762	21	0.08	43	2.9	5.4	0.75403	1.5	0.05	35.8894	5.6	0.34524	5.4	0.93	4837	22	1912	89	3663	56	75.7
22NP20B_G15	16604	8	0.02	29	1.76	12.7	0.7859	2.3	-0.14	63.2376	14.1	0.56745	12.7	0.85	4896	33	2897	297	4227	142	86.3
20109MS																					
20109MS_G6	3592	5	7.33	8	5.49	6.6	0.78153	3.8	0.4	19.3482	6.4	0.18206	6.6	0.72	4888	54	1078	65	3059	62	62.6
20109MS_G7	1453	6	4.09	3	15.08	6.3	0.65154	5.7	0.58	5.9041	6.9	0.06633	6.3	0.57	4627	82	414	25	1962	60	42.4
20109MS_G8	3435	16	4.41	6	17.8	5.5	0.46632	6.1	0.35	3.5258	6.8	0.05617	5.5	0.38	4137	91	352	19	1533	54	37.1
20109MS_G9	2458	6	4.73	6	8.84	4.9	0.75487	3.8	0.44	11.6606	5.3	0.11311	4.9	0.56	4838	54	691	32	2578	50	53.3
20109MS_G10	3159	7	3.07	7	7.9	5.3	0.75259	3.2	0.53	12.9931	5	0.12658	5.3	0.69	4834	46	768	38	2679	47	55.4
20109MS_G11	2745	7	3.32	6	10.15	4.5	0.73462	3.9	0.61	9.9489	4.8	0.09849	4.5	0.23	4799	55	606	26	2430	44	50.6
20109MS_G12	1039	4	3.3	2	14.2	5.7	0.72948	6.2	0.72	6.8009	5.4	0.0704	5.7	-0.01	4789	89	439	24	2086	48	43.6
20109MS_G13	5428	13	3.22	12	8.78	4.2	0.74352	2.3	0.58	11.6201	4.2	0.11389	4.2	0.41	4817	34	695	28	2574	39	53.4
20109MS_G14	3967	5	3.47	10	4.98	4.4	0.80346	2.8	0.73	22.2935	4.2	0.20083	4.4	0.31	4927	40	1180	48	3197	40	64.9
20109MS_G16	13516	15	6.08	32	4.11	8.7	0.78414	1.8	0.17	26.2844	8.5	0.2433	8.7	0.97	4893	25	1404	110	3357	83	68.6
20109MS_G17	2577	8	4.2	6	11.02	5	0.72017	4.5	0.65	8.8644	4.9	0.0907	5	0.42	4771	64	560	27	2324	45	48.7
20109MS_G18	3807	6	2.82	9	5.45	4.5	0.78842	3.3	0.68	19.7674	4.4	0.18361	4.5	0.24	4900	47	1087	45	3080	42	62.9
20109MS_G19	3281	4	3.4	8	5.1	5.2	0.80567	3.1	0.42	21.7808	5.3	0.19607	5.2	0.66	4931	45	1154	55	3174	51	64.4
20109MS_G20	3838	18	5.35	9	17.65	4.6	0.67401	3.5	0.62	5.1744	4.4	0.05665	4.6	0.19	4676	51	355	16	1848	38	39.5
20109MS_G21	3824	11	3.29	8	10.58	8.3	0.71824	4.2	-0.09	9.4274	9.8	0.09453	8.3	0.9	4767	60	582	46	2381	90	49.9
20109MS_G23	1905	5	2.14	3	9.78	6	0.77053	5.2	0.56	10.6334	6.1	0.1022	6	0.62	4868	74	627	36	2492	57	51.2
20109MS_G25	4548	10	4.64	7	8.57	4.6	0.75022	3.4	0.66	12.0507	4.6	0.11668	4.6	0.42	4829	49	711	31	2608	43	54
20109MS_G26	9021	51	1.38	12	21.09	4.4	0.63268	2.5	0.22	4.1076	4.6	0.04742	4.4	0.69	4584	36	299	13	1656	37	36.1
20109MS_G27	2229	5	2.88	3	7.48	5.4	0.73329	4.6	0.78	13.4914	4.8	0.13366	5.4	0.35	4797	66	809	41	2715	45	56.6
20109MS_G29	2024	6	3.93	3	10.47	4.9	0.74623	3.9	0.55	9.7935	5.2	0.0955	4.9	0.47	4822	56	588	28	2416	48	50.1
20109MS_G31	6030	15	3.56	8	9.48	4.8	0.74732	2.6	0.33	10.79	4.8	0.10548	4.8	0.74	4824	37	646	30	2505	44	51.9
20109MS_G33	2178	4	2.92	3	7.53	4.9	0.74802	4.4	0.56	13.3505	4.9	0.13285	4.9	0.33	4825	63	804	37	2705	46	56.1

Appendix E, Outlier consideration in AHe

To assess the potential impact of radiation damage in sedimentary and magmatic apatites, we constructed age versus effective uranium (eU) ppm plots (taking into account Crystal size typically represented by the equivalent spherical radius (ESR) in Fig. P), a proxy for radiation damage, as proposed by Shuster et al. (2006) and Flowers et al. (2009). Our analysis indicated that eU in apatite reached up to 40 ppm (Fig. S1). Based on this observation, we concluded that radiation damage was unlikely to have significantly impacted ages in our samples.

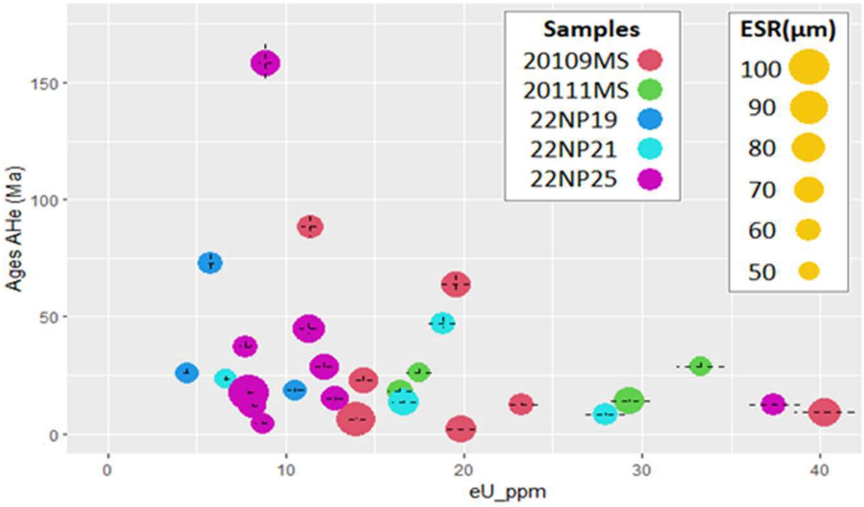

Fig. S1. Effective uranium (eU) ppm versus AHe grain ages (with errors indicated by ± 3σ), circle size represents the equivalent spherical radius.

For the Jurassic magmatic apatites, we examined AHe ages without outliers (Table. S3), we found that the samples fell comfortably within the confidence interval. Importantly, the age dispersion of AHe ($P(x)<0.05$ and $MSWD>1$ in Table N) within the ± 3σ error range showed no correlation with eU, suggesting that radiation damage had minimal influence on these grain ages. Instead, age dispersion appeared to result from other factors, such as parent nuclide zoning (Meesters and Dunai 2002), implantation from neighboring minerals (Spiegel et al. 2009), and fluid inclusions of radiometric He traps (Danišík et al. 2017).

Sample ID	Weighted mean age (Ma)	2σ (Ma)	Confidence interval	MSWD	P(χ^2)	grains used
22NP21	9.8	0.7	4.62E+00	42.00	0.00	2/4
22NP19	21.1	1.5	7.22E+00	23.00	0.00	2/3
22NP25	7.6	0.4	4.31E+00	120.00	0.00	5/9

Table S3. Weighted mean AHe ages of Jurassic magmatic apatite samples in the NU.

Consequently, we refrained from using weighted mean ages in our thermochronological modeling for these three magmatic samples (22NP19, 22NP21, and 22NP25). Instead, we utilized aliquots (single-grain ages) that fell within the confidence interval of each reproducible age, excluding any outliers.

Appendix F. chondrite normalized REE profile plots (spidergrams)

Chondrite normalized REE profile plots (spidergrams) from Jurassic magmatic and detrital rocks from Misahualli Formation and Abitagua Batholith:

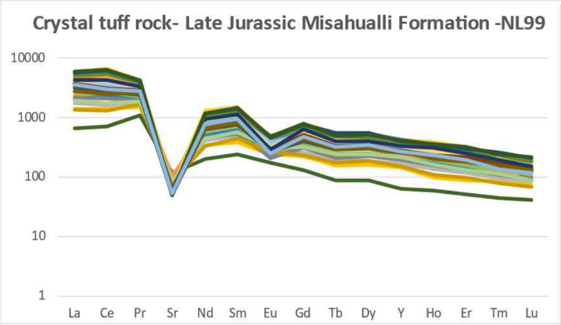
Crystal tuff rock- Late Jurassic Misahualli Formation -NL99

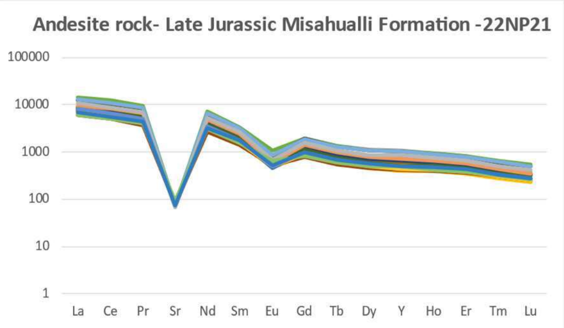
Andesite rock- Late Jurassic Misahualli Formation -22NP21

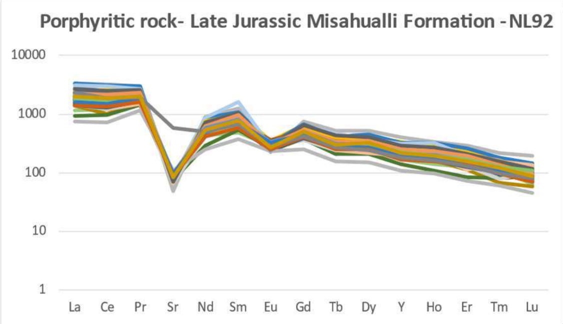
Porphyritic rock- Late Jurassic Misahualli Formation -NL92

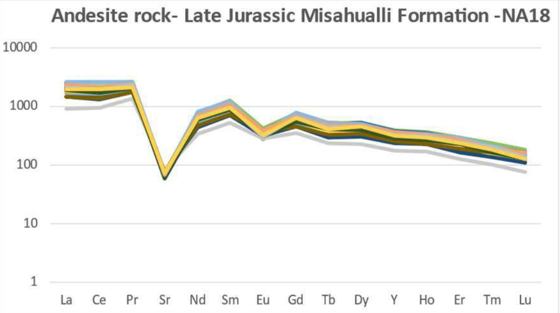
Andesite rock- Late Jurassic Misahualli Formation -NA18

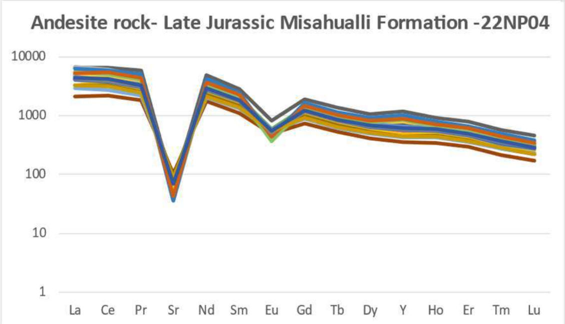
Andesite rock- Late Jurassic Misahualli Formation -22NP04

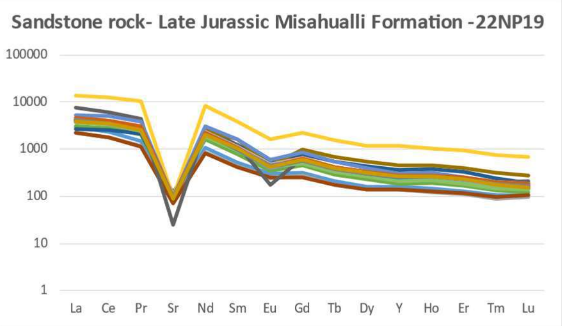
Sandstone rock- Late Jurassic Misahualli Formation -22NP19

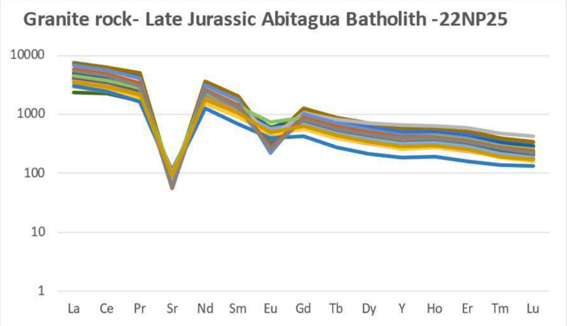
Granite rock- Late Jurassic Abitagua Batholith -22NP25

Chondrite normalized REE profile plots (spidergrams) from detrital Cretaceous-Cenozoic rocks from Tena, Tiyuyacu, Chalcana, Arajuno and Chambira Formations

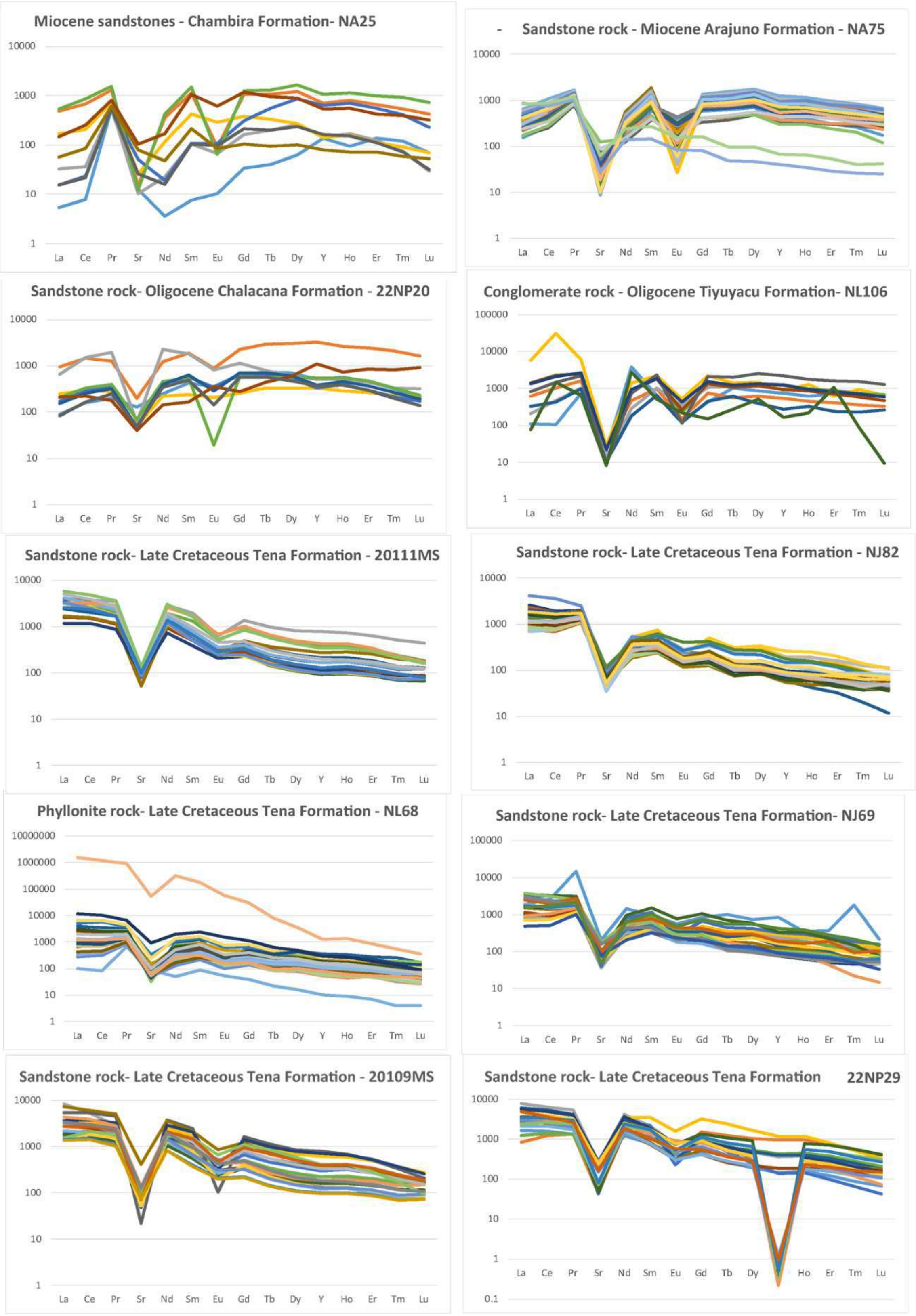

Miocene sandstones - Chambira Formation- NA25

- Sandstone rock - Miocene Arajuno Formation - NA75

Sandstone rock- Oligocene Chalacana Formation - 22NP20

Conglomerate rock - Oligocene Tiyuyacu Formation- NL106

Sandstone rock- Late Cretaceous Tena Formation - 20111MS

Sandstone rock- Late Cretaceous Tena Formation - NJ82

Phyllonite rock- Late Cretaceous Tena Formation - NL68

Sandstone rock- Late Cretaceous Tena Formation- NJ69

Sandstone rock- Late Cretaceous Tena Formation - 20109MS

Sandstone rock- Late Cretaceous Tena Formation 22NP29